Model-Based Electrodermal Activity Sleep Events Detection Algorithm

Jacopo Piccini

Thesis submitted to the Department of Engineering at Reykjavík University in partial fulfillment of the requirements for the degree of Doctor of Philosophy

June 5, 2025

Thesis Committee:

Elias August, Supervisor
Associate Professor, Reykjavik University, Iceland

María Óskarsdóttir, Co-Supervisor
Associate Professor, Reykjavik University, Iceland

Erna Sif Arnardóttir, Committee
Associate Professor, Reykjavik University, Iceland

Sigurður Freyr Hafstein, Committee
Professor, University of Iceland, Iceland

Tatjana Petrov, Examiner
Junior Professor, Università di Trieste, Italy

ISBN print version 978-9935-539-58-8
ISBN electronic version 978-9935-539-59-5
http://hdl.handle.net/1946/xxxx

The undersigned hereby certify that they recommend to the Department of Engineering at Reykjavík University for acceptance this Thesis entitled **Model-Based Electrodermal Activity Sleep Events Detection Algorithm** submitted by **Jacopo Piccini** in partial fulfillment of the requirements for the degree of **Doctor of Philosophy(Ph.D.) in Engineering**

.....

date

Student:

.....

Jacopo Piccini

Thesis Committee:

.....

Elias August

.....

María Óskarsdóttir

.....

Erna Sif Arnardóttir

.....

Sigurður Freyr Hafstein

.....

Tatjana Petrov

To Gloria,

Contents

List of Figures

List of Tables

Model-Based Electrodermal Activity Sleep Events Detection Algorithm

Jacopo Piccini

March 2, 2025

Abstract

Despite the pivotal role of sleep in one's life, quantitative methods to investigate it have been lagging behind. Recent years have witnessed a spike in the application of machine learning (ML) to automate the analysis of physiological signals. Throughout this dissertation, we focus on the electrodermal activity (EDA) signal, which has been long-known in the literature, but due to its need for extensive processing has been scarcely used for diagnostics purposes.

After an introduction and overview on the topic and challenges of diagnosing sleep health, we provide the needed mathematical background for the mathematical tools used throughout this dissertation. We then move to the first part of the thesis, where we present algorithms designed to extract information and diagnose sleep using the EDA signal. We developed these algorithms using both traditional signal-processing and ML methods. After presenting data-driven tools, we dedicate the second part of this thesisto develop physics-driven frameworks to study thermoregulation, which greatly affects the EDA signal. During sleep, the EDA signal is generated through a combination of sleep-specific patterns and thermoregulation responses. Furthermore, there is plenty of empirical knowledge on human body thermoregulation and the optimality of such processes during specific part of the night. We start by proposing a novel framework using control theory and mathematical biology to translate experimental observations on physiological mechanisms to a small set of ordinary differential equations (ODEs). As many others processes during sleep, thermoregulation dynamics undergoes significant and abrupt changes making it, approximately, a switched system. Characterising these class of dynamical systems is an open problem in control theory; even proving the stability of such systems in the simplest of cases, for example, linear switched systems, can be a challenge.

We conclude this dissertation proposing an overlook on how the methods and ideas introduced in this thesis can be used to formulate and tackle new research problems.

Keywords: Electrodermal activity, thermoregulation, sleep, machine learning, numerical optimal control, switched systems, Lyapunov functions.

Acknowledgments

Before writing this section, I never fully realized how many people helped me navigate the amazing (and scary) journey of a PhD. Properly thanking each one of you will be a difficult task, but I will do my best.

First, I would like to express my deepest gratitude to my supervisor, Prof. Elias August. The three years spent working with you have helped me grow both professionally and personally in ways I could never have imagined. You were always there whenever I came knocking on your office door, no matter the reason.
Such deep gratitude also goes to Prof. María Óskarsdóttir for introducing me to the fascinating world of machine learning (of which I remain fairly skeptical); and to Prof. Erna Sif Árnardóttir for her valuable biological feedback.
I need to thank Prof. Sigurður Freyr Hafstein and Stefania Andersen for the many discussions over the years, which I've always found enriching. Thank you Siggi, for agreeing to be on my Committee. A special thank you to Prof. Tatjana Petrov for agreeing to serve as examiner.
Finally, I would like to thank Andrei Manolescu for giving me the opportunity to be a teaching assistant in the Statistics course. It has been an enriching experience.

Outside of Iceland, I want to thank Joel Stavans and Rinat Goren. Although I never had the chance to visit Weizmann (a huge regret), the time spent working with you reignited my love for research and reassured me that I was doing research right.

Looking back, I realize how much support I received from Italy. I need to thank my parents for teaching me to finish what I start; it has been an invaluable skill. To my brother, for reminding me how significant baseball has been in my life, something I had forgotten. Unsung support came from Riccardo and Serena, for always making me feel at home and never unwanted. Lastly, to Gloria, you know everything I could say. I'll limit myself to saying that I would never have made it through without you.

Chapter 1

Introduction

1.1 Background and Motivation

Sleep is a fundamental aspect of human health. However, although we spend one-third of our lives sleeping and the consequences of lack or inadequate sleep are well known, we still poorly understand it. In 2022, The Lancet and The Lancet Neurology published a four-paper series where sleep was defined as the "Cinderella branch of medicine", [2]. The editorial highlights the mismatch between the pivotal importance of sleep and its underappreciation at the educational and funding levels.

In parallel with the interest in sleep research, the importance of healthy sleep is becoming more well-known to the general public and increasingly the object of research. The importance of research on sleep and its disorders is becoming even more prominent as the frequency of sleep disorders is likely to increase because of modern lifestyle. While it has become clear that proper and timely sleep diagnosis is crucial to reduce the impact of poor sleep on health and minimise the burden of sleep-related conditions on healthcare systems, sleep data are still commonly annotated by hand, which is very resource-consuming and delays diagnosis.

Only recently have modern computational tools being applied to sleep research. Particularly, thanks to the rise in computational power, research on sleep diagnostics is benefiting from using machine learning (ML) methods to automate time-consuming tasks, such as sleep staging and there is an ever-increasing interest in developing algorithms that can automate manual scoring activities, [3, 4].

However, current ML algorithms are trained on the same signal set used by sleep experts during manual scoring activities, such as electroencephalogram (EEG), electrooculogram (EOG), and submental electromyogram (EMG) signals [5]. While this allows a direct comparison between ML and human performances, it prevents using different signals to diagnose sleep, which might provide additional informa-

tion on sleep health. A second prominent bottleneck in sleep healthcare is the limited number of sleep studies that can be performed. Currently, the gold standard for sleep studies is polysomnography (PSG), an extensive and invasive study that must be carried out in a controlled environment, which massively reduces accessibility to sleep studies.

Indeed, modern research is moving in two different directions to mitigate these issues. The first one is the development of ML algorithms to perform accurate automatic scoring. The second research direction takes advantage of the growing popularity of wearable devices and aims at developing new devices that provide accurate information on sleep health. The former research direction focuses on automating the scoring of traditional measures, for example, EEGs; while developing such an algorithm would reduce the time needed to score PSG recordings, it would not make sleep studies accessible to more people. On the other hand, significant research efforts are being devoted to developing new wearable devices, such as smartwatches [6] and self-applied electrodes [7], which would allow to perform studies in free-living conditions.

PSGs consist of one-night recordings, an invasive set of sensors and the unfamiliar setting can cause sleep that is not consistent with sleep in everyday conditions [8]; this can be exacerbated by the intrusiveness of the PSG setting, see Fig. 1.1 where we show a traditional PSG setting. Sensors employed to record signals are physically attached to an external base station; this can cause significant discomfort as it causes major motion constraints for the participant. For example, even simple actions, such as turning twice in the opposite direction to the base of the recording device, could easily result in the study participant becoming tangled. This, in turn, might cause the participant to wake up or lead to the detachment of cables, potentially disrupting the recording process. Furthermore, because of the need of accurate placement of the sensors, this study can only be carried out in hospitals or specialised clinics.

The use of wearable devices allows to collect multiple night recordings, and to obtain a more complete and trustful set of sleep signals [9, 10]. However, alternative signals must be used. Actimetry, the processing of acceleration signals, has been widely used in sleep medicine to detect wakefulness and sleep status. A further signal which can be recorded at the wrist and is rich in physiological meaning is the electrodermal activity (EDA) signal.

Until recently, EDA has been rather overlooked in sleep medicine; which is striking, considering the number of wakefulness applications in which EDA is used. EDA measures the fluctuations in the skin's electrical properties, largely caused by sweating. Furthermore, although the mechanisms governing sweating, and therefore skin electrical properties dynamics, are yet to be understood, it has been since 1969 that EDA has been appointed as an outstanding candidate for monitoring sleep because of its relationship with sleep [11]. During wakefulness, sweat is secreted in response to emotional stimuli, such as stress [12]. Be-

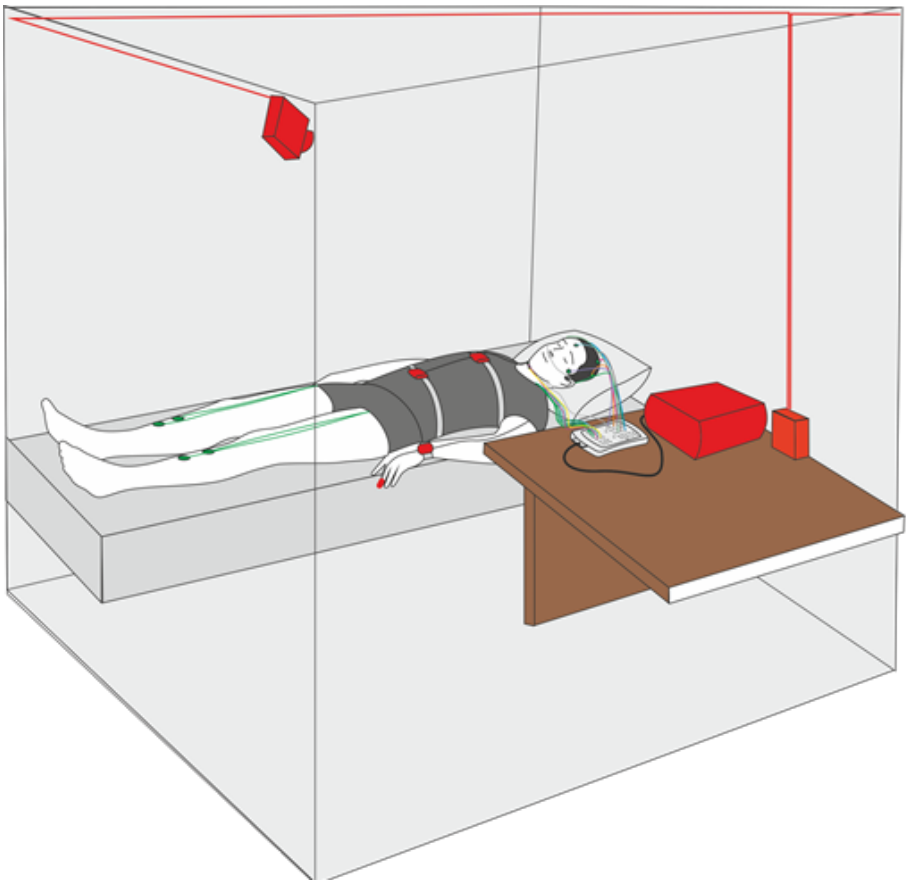

Figure 1.1: A scheme of a traditional polysomnography (PSG) setup.

cause of this relationship, it is used to detect the physiological state during various tasks. On the other hand, during sleep, the emotional contribution to EDA becomes negligible. Particularly, the sympathetic nervous system (SNS) employs sweating solely for thermoregulation purposes. Even during rare and potentially intense emotional events, such as nightmares, EDA signals remain robust to these occurrences. Even during these emotions-induced sweat manifestation, abnormal patterns in EDA signals only appear in a localised time window, not affecting the remaining part of sleep [13]; thus the EDA signal is a valid candidate for diagnosing general sleep health characteristics. The isolation from external stimuli makes the EDA signal a promising candidate for understanding SNS behaviour; additionally, the existence of sleep-characteristic EDA phenomena is well-established in

the literature [14].

However, using EDA for sleep applications is a rather complex task. The difficulty is mainly due to the signal's noise often caused by sudden motions or poor attachment between the sensor and the skin. However, EDA exhibits clear patterns in specific sleep stages, and through proper processing it might be possible to use such signals to obtain a non-invasive sleep stages prediction.

OSA is one of the most common sleep-disordered breathing causing repetitive pharyngeal collapses [15]. Sleep-disordered breathing is estimated to affect 20% of men and 10% of women in high-income countries [16]. Two of the main OSA symptoms are excessive daytime sleepiness (EDS) and cardiovascular complications, for example, hypertension and coronary artery disease [17]. OSA diagnosis and evaluation is a difficult task; the gold standard for its detection is, again, PSG. The traditional way to evaluate OSA is by means of two indices, the apnoea-hypopnoea index (AHI) and the oxygen desaturation index (ODI). These two measures complement each other. AHI gives a measure of apnoea and hypopnoea frequency, while ODI measures the severity of such occurrences by evaluating the drop in blood oxygen saturation. OSA occurrences are also characterised by hyperhidrosis, that is, excessive sweating [18]. Previous studies confirmed abnormal patterns in EDA signals during OSA events. Similarly to sleep stages classification, EDA might be a good predictor to evaluate OSA conditions.

Data-driven methods have been used to only explain the visible side of sleep, that is, physiological manifestations. To the best of our knowledge, there is a lack of AI methods used to understand the underlying physiological mechanisms during sleep. This kind of insight can be obtained through the use of mechanistic mathematical modelling [19]. Thermoregulation is the primary mechanism causing EDA fluctuations through sweat secretion. Thermoregulation during sleep is not a uniform process and there are significant differences in its behaviour between non-rapid eye movement (NREM) sleep and REM sleep. During NREM, the human body induces a decrease in core body temperature (CBT) [20], which is an average of organs and brain temperatures, to match the circadian-rhythm-induced oscillation. Such decrease in CBT is needed to maximise the likelihood of sleep [21] even further, while divergence from this cooling cycle can lead to insomnia [22]. During NREM sleep, changes in CBT are achieved through appropriate thermoregulatory responses while minimising the energy used to achieve the change. This energy-optimal behaviour has been observed through a wide variety of endothermal animals [23]. This energy allocation is thought to have an evolutionary purpose as animals minimising energy expenditure at night have more energy available during the day, therefore obtaining an ecological advantage. While the role and aim of thermoregulation during most of sleep is well understood, the same cannot be said of REM sleep, which remains poorly understood. During REM epochs, more energy is allocated to maintain brain activity levels close to those observed during wakefulness. These activity levels are needed for the de-

velopment of cognitive abilities [24, 25], although the exact mechanisms are still not clear. Research on thermoregulation has been conducted at different levels, both during sleep and wakefulness, using qualitative and quantitative approaches. Romanovsky provides a feedback-like architecture for the thermoregulation system [26, 27]; particularly, the human body generates thermoregulatory responses evaluating the deviations of actual temperature signals of different body parts from their reference values. These signals are then evaluated in the hypothalamus and appropriate thermoregulation responses are generated [28]. Despite substantial knowledge of the architecture of the thermoregulation system and its optimality, optimal control has yet to be introduced to the analysis of thermoregulation during sleep.

1.2 Thesis Outline

The doctoral research carried out has led to the following publications which constitute this thesis:

- Piccini, J., August, E., Noel Aziz Hanna, S. L., Siilak, T., & Arnardóttir, E. S. (2023). *Automatic Detection of Electrodermal Activity Events during Sleep.* Signals, 4(4), 877–891, (Chapter 3).
- Piccini, J., August, E., Óskarsdóttir, M., & Arnardóttir, E. S.(2023). *Using the electrodermal activity signal and machine learning for diagnosing sleep*. Frontiers in Sleep, 2. https://doi.org/10.3389/frsle.2023.1127697, (Chapter 4).
- Piccini, J., August, E., Hafstein, S., & Andersen, S. (2023). *Sufficient Stability Conditions for a Class of Switched Systems With Multiple Steady States.* IEEE Control Systems Letters, 7, 2653–2658, (Chapter 6).

The article presented in Chapter 5 is yet to be submitted.

In Chapters 3-5, we present various quantitative tools based on different theories, and use them to characterise thermoregulation during sleep and its manifestations. Particularly:

- Chapter 2 provides the mathematical concepts used in this thesis. First, we introduce the signal processing methods used in the present data-driven applications; then, we move to describing Lyapunov stability, switched systems, and the computational frameworks used to solve optimisation problems.
- In Chapter 3, we use signal processing methods to develop an algorithm capable of automatically detecting EDA events and EDA storms. These are some of the most prominent manifestations of EDA and show clear patterns

in specific sleep phases. However, the distinctive noise in EDA signals has made it difficult to develop methods to automatically detect these phenomena; such difficulty has been exacerbated to the point that there is not a unique definition for an EDA event. In this work, we use a often used definition and translate it into frequency and amplitude requirements. We then use subsequent extensive processing of the raw signal to detect oscillations satisfying new requirements. We then compare the algorithm's automatic scoring with the manual scoring performed by a sleep technologist. We do so by providing different indices characterising the overlap between the scorings. We conclude the chapter with statistical analyses comparing the automatic and manual scorings. We obtain F1-score-like values of 69%, and 56%, when detecting EDA events, and EDA storms, respectively. Furthermore, by performing a two-sample t-test comparing automatic, and manual scorings, the p-values does not suggest a statistical significance between the two scorings; not for EDA events, nor for EDA storms.

- In Chapter 4, we present an ML model trained on EDA signals for sleep diagnostics purposes. The goal of this chapter is to prove that by properly processing and by extracting physiology-inspired metrics, EDA signals can be used to obtain sleep health measures. In this chapter, we do not simply rely on computational power, rather we use a relatively simple learning algorithm, that is, extreme gradient boosting (XGB), while focusing on feature engineering. We build on qualitative, and to a smaller extent quantitative, observations about EDA events and EDA storms being more common in specific sleep stages. Particularly, we use the detection algorithm from Chapter 3 to design a set of learning variables related to EDA events and EDA storms. When performing sleep staging, we obtain an average F1-score of 57.5%, and 66.6&, depending on whether we considered five or four sleep stages, respectively. Training the algorithm to detect OSA resulted in better performances, leading to an accuracy of 83.7%, or 78.4%, depending on the index used, ODI, or AHI, respectively.

- In Chapter 5, we propose a new framework to study thermoregulation during NREM sleep. Particularly, we design a low dimensional model by combining physical modelling and optimal control theory. First, we model heat exchanges; second, we design and solve an optimisation problem describing the energy allocation process. Solving such optimisation problem, we generate a sequence of thermoregulation responses obtaining the required tracking properties, while fulfilling physiological constraints.

- In Chapter 6, we deal with the problem of determining the stability of switched systems. Switched systems are an important subclass of dynamical systems that might be used to model thermoregulation dynamics transition between

NREM and REM sleep. We use absorbing sets and sum of squares (SOS) decomposition to prove the existence of a Lyapunov function providing a stability certificate for both nonlinear and linear dynamical switching systems. We show that the presented approach can provide stability certificates for a wide range of switched systems, both linear and nonlinear, at a reduced computational cost.

- Finally, Chapter 7 concludes the thesis by summarising the research work performed and presenting future research directions.

Chapter 2

Mathematical Preliminiaries

In this Chapter, we present the main mathematical tools used in this thesis. In Section 2.1, we review the notion of wavelet transforms. In Section 2.2, we present the theory behind gradient boosting family algorithms, we then go into the details of the specific algorithm implementation in Sec. 2.3.1. We present the theory behind the nonlinear optimisation solver used in Section 2.7. We dedicate Section 2.4 to review Lyapunov stability theory, while we review Sum of Squares (SOS) decomposition in 2.6.

2.1 Wavelet Transform

The wavelet transform (WT) can be seen as an extension of Fourier transform, where an approximation of a periodic function is created by superimposing trigonometrical base functions, particularly, sines and cosines. Particularly, the use of wavelets allows to use different basis functions. By allowing the use of a number of different functions rather than only sine and cosine functions wavelets allow to analyse a signal at different scales, which has been used to automatically extract features in ML. The core element of wavelet analysis is the base function, also called mother wavelet, which we denote by $\psi(t)$.

2.1.1 Continuous Wavelet Function

Analogously to the continuous Fourier transform (FT), the continuous wavelet transform (CWT) is written as:

$$W_f(s,\tau) = \int_{-\infty}^{\infty} f(t)\psi^*_{s,\tau}(t)dt, \tag{2.1}$$

where * denotes the complex conjugate operator, and $f(t)$ is the signal to be decomposed. The key parameters s, τ generate a set of wavelets $\psi_{s,\tau}$, where s is the scale factor and τ is the translation factor. The scale factor determines the view level of the wavelet, that is, it determines how compressed, or stretched, the basis function is. Large scale factors will stretch the mother wavelet and, therefore, providing a more global view of the signals and capturing coarser features. Conversely, small scale factors will provide focus on finer details. The set of wavelets generated by the mother wavelet is expressed as:

$$\psi_{s,\tau} = \frac{1}{\sqrt{s}}\psi\left(\frac{t-\tau}{s}\right). \tag{2.2}$$

As per (2.2), all wavelets generated through the mother wavelet ψ have the same shape but different scale and location.

2.1.2 Wavelet Properties

A wavelet must fulfil the admissibility and the regularity conditions. The admissibility condition is used to verify the ability to reconstruct a signal without any loss of information. The wavelet $\psi(t)$ must satisfy the following condition:

$$\int_0^\infty \frac{|\Psi(\omega)|^2}{|\omega|} d\omega < +\infty, \tag{2.3}$$

where $\Psi(\omega)$ represents the Fourier transform of the wavelet function $\psi(t)$. The admissibility condition is needed to guarantee perfect reconstruction of the signal. Furthermore, it has the following implication:

$$\int_{-\infty}^{\infty} \psi(t)dt = 0. \tag{2.4}$$

By requiring (2.4), wavelet functions capture the dynamics of the signal rather than constant contributions.
The regularity condition requires that wavelet functions must be localised in both time and frequency domains. It is usually stated by setting the translation factor to zero, that is, $\tau = 0$, and considering the Taylor series of (2.1):

$$W_f(s,0) = \frac{1}{\sqrt{s}}\left[\sum_{p=0}^{n} f^{(p)}(0)\int_{-\infty}^{\infty}\frac{t^p}{p!}\psi\left(\frac{t}{s}\right)dt + \mathcal{O}(n+1)\right], \tag{2.5}$$

where we denote the p-th derivative of f as $f^{(p)}$. We can rewrite (2.5) by introducing wavelet moments:

$$M_p = \int_{-\infty}^{\infty} t^p\psi(t)dt. \tag{2.6}$$

Therefore, (2.5) becomes:

$$W_f(s,0) = \frac{1}{\sqrt{s}}\left[\sum_{p=0}^{n}\frac{f^{(p)}(0)}{p!}M_p s^{p+1}\right]. \tag{2.7}$$

Because of the admissibility condition $M_0 = \int_{-\infty}^{\infty} t^0\phi(t)dt = 0$. In addition to $M_0 = 0$, it is possible to make other moments equal to zero. By doing so, we are obtaining smoother mother wavelets which are better at approximating sharp changes in the signal.

2.1.3 Discrete Wavelet Transform

Although powerful, CWTs are not efficient in the representation of the signal. This is because of the continuous range of the scale and translation factors. In most applications, scale and translation factors are discretised, we refer to the resulting WT as discrete wavelet transform (DWT). Although being named discrete, DWTs are actually continuous in time. DWTs are rather CWTs evaluated on a finite grid of scale factors and dilation steps. The discrete scale and translation factors are expressed as:

$$s = s_0^i, \quad s_0 > 1,\ i \in \mathbb{Z}, \tag{2.8}$$

$$\tau = k\tau_0 s_0^i, \quad k,\ i \in \mathbb{Z}. \tag{2.9}$$

Here, s_0 is a fixed dilation step. Note that, often computer implementations set $s_0 = 2$. The usual choice for the translation step is $\tau_0 = 1$ [29]. When $s_0 \simeq 1$ and $\tau_0 \simeq 1$, the DWT closely approximates the CWT, as scale and translation grids are denser. The resulting discrete wavelets are obtained by inserting (2.8) and (2.9) into (2.2) [30]:

$$\psi_{i,k}(t) = \frac{1}{\sqrt{s_0^i}}\psi\left(\frac{t - k\tau_0 s_0^i}{s_0^i}\right). \tag{2.10}$$

The computer implementation therefore becomes:

$$\psi_{i,k}(t) = \frac{1}{\sqrt{2^i}}\psi\left(\frac{t}{2^i} - k\right), \tag{2.11}$$

and the DWT coefficients:

$$W_f(j,k) = \frac{1}{2^j}\int_{-0}^{\infty} f(t)\psi^*\left(\frac{t}{2^j} - k\right)dt = \left\langle f(t), \psi_{j,k}(t)\right\rangle \tag{2.12}$$

2.1.4 Multiresolution Analysis

DWTs form the backbone of the so-called Multiresolution Analysis (MRA). MRA is a powerful framework that allows signals to be decomposed and analysed across successive frequency bands. For the MRA framework to be applicable, the signal must have finite energy, expressed as:

$$\int_0^\infty f(t)^2 dt < \infty. \tag{2.13}$$

If such constraint holds, then, $f(t)$ lies in the Lebesgue space, that is, the space of all square integrable functions, mathematically denoted as $f(t) \in L^2(\mathbb{R})$. A MRA is defined as a sequence of sets V_i dividing the Lebesgue space. This decomposition is complemented by a second sequence of subspaces W_j, where W_j has an orthonormal basis formed by the wavelet function:

$$\psi_{j,k}(t) = \frac{1}{\sqrt{2^j}} \psi\left(\frac{t}{\sqrt{2^j}} - k\right), \quad j,\, k \in \mathbb{Z}. \tag{2.14}$$

Analogously, subspaces V_i are generated by introducing a second function, that is the scaling function $\phi_{j,k}$. Furthermore, in MRA, the subspace families $V_i,\ W_j$ have the following properties [31]:

$$\ldots \subset V_{-2} \subset V_{-1} \subset V_0 \subset V_1 \subset V_2 \subset \ldots \tag{2.15}$$

$$V_\infty = L^2(\mathbb{R}) \tag{2.16}$$

$$V_{-\infty} = \{0\} \tag{2.17}$$

$$f(t) \in V_j \iff f(2^j t) \in V_0. \tag{2.18}$$

The scaling function $\phi(t)$ is defined similarly to the wavelet function, particularly:

$$\phi_{j,k}(t) = \frac{1}{\sqrt{2^j}} \phi\left(\frac{t}{\sqrt{2^j}} - k\right), \quad j,k \in \mathbb{Z}. \tag{2.19}$$

The scaling function determines the approximation space V_j, which represents the coarse-scale structure of a signal, while the wavelet function defines the detail space W_j, capturing finer-scale information. Let us assume that $f(t) \in V_0$ that is the approximation space for $j = 0$. Since $V_1 \perp W_1$, the initial approximation space can be rewritten as:

$$V_0 = V_1 \oplus W_1, \tag{2.20}$$

where $\oplus$ denotes the direct sum of functional spaces. Because $V_j,\ W_j$ are spanned by orthonormal functions, the original signal $f(t)$ lying in V_0 can be rewritten as the sum of its projections in V_1 and in W_1:

$$f(t) = C_1 f(t) + D_1 f(t) \tag{2.21}$$

In (2.21), we denote the projections of $f(t)$ on V_1 and W_1 as $C_1,\ D_1$, respectively. These projections are calcualted as follows:

$$C_1 f(t) = \sum_k c_1(k)\phi_{1,k}(t), \tag{2.22}$$

$$D_1 f(t) = \sum_k d_1(k)\psi_{1,k}(t), \tag{2.23}$$

where $c_1(k)$ and $d_1(k)$ are the expansion coefficients corresponding to the scaling and wavelet functions. Since $\phi_{1,k}(t),\ \psi_{1,k}(t)$ form orthonormal bases for $V_1,\ W_1$, respectively, the coefficients are computed as:

$$c_1(k) = \langle \phi_{1,k}(t), f(t) \rangle, \tag{2.24}$$

$$d_1(k) = \langle \psi_{1,k}(t), f(t) \rangle, \tag{2.25}$$

where $\langle \cdot, \cdot \rangle$ denotes the inner product. By iterating the decomposition process up to a desired resolution level J, the signal $f(t)$ is approximated as:

$$f(t) \approx C_J f(t) + \sum_{j=1}^{J} D_j f(t), \tag{2.26}$$

where $C_J f(t)$ represents the projection on the approximation subspace V_J and the sequence $\{D_j f\}_{j=1}^{J}$ represents the projection coefficients on progressively finer subspaces.

Alternatively, the expansion coefficients $c_1(k)$ and $d_1(k)$ can be computed using discrete filtering operations, particularly by introducing interscale low-pass and high-pass discrete filters; we denote them as $p(n),$ and $q(n)$, respectively.

$$c_1(k) = \frac{1}{\sqrt{2}} \sum_n p(n-2k)c_0(n), \tag{2.27}$$

$$d_1(k) = \frac{1}{\sqrt{2}} \sum_n q(n-2k)c_0(n) \tag{2.28}$$

In the latter, $c_0(n)$ represents the scaling coefficients of $f(t)$ at the previous level. The factor of $\frac{1}{\sqrt{2}}$ ensures normalization, and the downsampling by a factor of 2 arises from the shift in the filters $p(n),\ q(n)$. Coefficients normalisation is needed to guarantee the conservation of the signal's energy, while downsampling coefficients results in efficient DWT computations.

2.1.5 Stationary Wavelet Transform

In Chapter 3, we utilize Wavelet Transforms (WTs) to denoise electrodermal activity (EDA) signals, particularly near sudden spikes. A known limitation of the

Discrete Wavelet Transform (DWT) is its lack of translation invariance. This issue arises due to the downsampling step in the decomposition process, as described in (2.27). Downsampling discards specific samples, making the wavelet coefficients highly sensitive to small shifts or translations in the input signal. Even slight translations can lead to significant changes in feature detection, which may result in inconsistent denoising performance, especially in regions with abrupt changes, such as spikes. To address this problem, we use the Stationary Wavelet Transform (SWT). Unlike the DWT, the SWT does not perform downsampling. Instead, it retains the original sampling rate at all decomposition levels, maintaining the resolution of the signal throughout the analysis. Because of this property, SWT is often referred to as the non-decimated DWT. By avoiding downsampling, the SWT achieves time-invariance, meaning that its representation of the signal remains consistent regardless of small shifts or translations. This characteristic makes SWT particularly well-suited for applications like denoising and feature extraction in signals with sharp transients, where maintaining accuracy around abrupt changes is critical. In summary, the SWT provides a robust alternative to the DWT by sacrificing efficiency and introducing redundancy to achieve translation invariance, ensuring better consistency and reliability in detecting and processing signal features near sudden spikes.

Example 1. *DWT*
Let us consider the illustrative signal:

$$f(t) = sin(2\pi f_1 t) + sin(2\pi f_2 t) + 0.5\epsilon, \tag{2.29}$$

where $f_1 = 7$ Hz, $f_2 = 13$ Hz, and ϵ represents normal standard random noise affecting the signal. We analyse this signal using the `db4` mother wavelet, that is a Daubechies wavelet with four vanishing moments. We can analyse the signal as described in Sec. 2.1.4, that is, by splitting low-frequencies and high-frequencies by calculating the approximation and detail coefficient, respectively. For this example, we create three levels of coefficients, we show both approximation and detail coefficients in Fig. 2.1. As seen in the previous plots, going into lower decomposition levels ensure smoother approximation coefficients. Detail coefficients show a similar trend, that is, decomposition level one, capture noise and the most high-frequency contributions in the original signal. Further decomposition levels, reduce the contributions' frequency being captured.

2.2 Gradient Boosting

One thing to keep in mind when developing ML models for healthcare applications is explainability [32]. The need to fully understand the learning process of the ML model significantly reduces the number of usable algorithms. Gradient

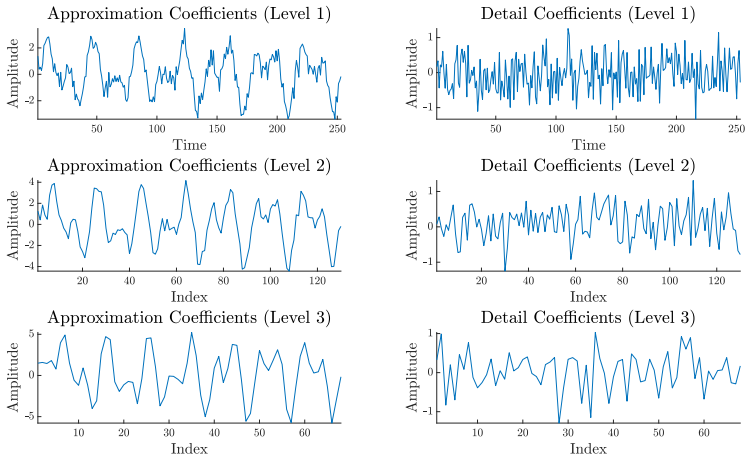

Figure 2.1: Approximation and detail coefficients up to decomposition level three of (2.29).

boosting (GB) is a popular class of learning algorithms, which has being applied to a wide variety of fields, from credit scoring [33] to bioactive molecule prediction [34]; we refer the interested reader to [35] for a thorough review on different implementations and different applications. The main idea behind GB is to combine many so-called weak learners to obtain a strong one [36].

2.2.1 Decision Trees

Decision trees are a popular choice when choosing a weak learner. Decision trees partition the space of the feature set $x \in \mathbb{R}^n$ into J regions $I_1, I_j, \ldots, I_J$, by defining a set of thresholds. Each region is characterised by a weight w_j. We provide a graphical representation of a simple split domain in Fig. 2.2.
Fig. 2.2 also highlights the main feature that makes decision trees-based algorithms appealing for healthcare applications, which is that they are easy to explain. A tree is mathematically expressed as follows:

$$\varphi\left(x, \{w_j, I_j\}_1^J\right) = \sum_{j=1}^{J} w_j 1\left(x \in I_j\right), \tag{2.30}$$

where $\varphi\left(x, \{w_j, I_j\}_1^J\right)$ is the output of the decision tree given the input to φ is x and $1\left(x \in I_j\right)$ is 1 if $x \in I_j$ and 0 otherwise. Through (2.30), the output φ is calculated by checking in which region I_j, the input vector x falls into. The problem

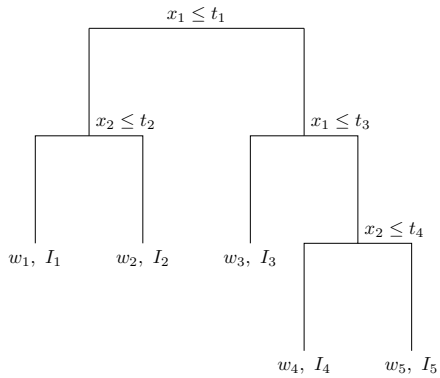

Figure 2.2: Exemplary visualisation of how the regions I_j are defined, for a feature set with two learning variables, that is, x_1, and x_2.

of optimising weights and splits of decision trees is a combinatorial one [37]. Such problems can be decomposed into two parts: The first one, the hard one, is how to split the feature domain in subregions I_j. The second problem, and easier one, is obtaining w_j after the division in I_J regions. We explain how extreme gradient boosting (XGBoost), the algorithm used in Chapter 4, solves the domain-splitting issue in the following Sections. Let us show an example about decision tree training.

Example 2. *Decision Trees*
Let us in consider the following dataset:

x	**y**
5	2
6	3
7	3
10	7
12	8

For sake of this example, let us arbitrarily split the data at $x = 7$. Now, for each domain, let us calculate the mean predicted values for the left and right domains:

$$\hat{y}_{left} \simeq 2.67 \tag{2.31}$$
$$\hat{y}_{right} = 7.5. \tag{2.32}$$

While using the mean squared error (MSE) as loss function, we calculate the loss for the left spilt as follows:

$$MSE = \frac{1}{N}\sum_{i=1}^{N}(y_i - \hat{y})^2. \tag{2.33}$$

Applying (2.33) to the left and right domain, we obtain: $MSE_{left} \approxeq 0.22$, $MSE_{right} = 0.25$. This process is repeated evaluating different split candidates. The weighted MSE, that is, $wMSE$, is then calculated as:

$$wMSE = \frac{\#Left}{n_{tot}} MSE_{left} + \frac{\#Right}{n_{tot}} MSE_{right}. \tag{2.34}$$

This process is repeated considering different splits, until all candidate splits are evaluated. Finally, the split resulting into the lowest $wMSE$ is chosen as split.

2.3 Gradient Boosting

GB algorithms learn on a feature set $X \in \mathbb{R}^{n\times m}$, where m is the number of features and n is the number of observations, and on the corresponding label vector $y \in \mathbb{R}^n$. In the following, we consider the learning process for a single data point, therefore we consider a row vector $x \in \mathbb{R}^m$, from the feature set X. The way approximations are constructed is by taking the previous iteration approximation and adding a weak learner to correct the previous prediction. For the t-th iteration we have:

$$\hat{y}^{(t)}(x) = \hat{y}^{(t-1)}(x) + \alpha^{(t)} z^{(t)}(x), \tag{2.35}$$

where $\hat{y}^{(t)}$ is the approximations at the t-th iteration, $\alpha^{(t)}$ is the weight of the function $z^{(t)}(x)$ minimising the loss function at the current step. In this sense, the gradient boosting algorithm is a greedy one, the solution tree $z^{(t)}(x)$ is chosen to maximise the reduction in the loss function at the current iteration. A general gradient boosting algorithm generates consecutive models to minimise the following function:

$$\mathcal{L}^{(t)} = \sum_{i=1}^{n} \ell\left(y_i, \hat{y}_i^{(t-1)} + \alpha^{(t)} z^{(t)}(x)\right). \tag{2.36}$$

In (2.36), ℓ is a differentiable convex function, popular choices are the squared loss function and the logistic function, an extensive review of the possible loss functions is carried out in [38]. To choose $z^{(t)}(x)$, we compute the gradient of the loss function to obtain the steepest descent direction:

$$g_i^{(t)} = -\frac{\partial \ell\left(y_i, \hat{y}(x)\right)}{\partial \hat{y}}\Big|_{\hat{y}^{(t-1)}}. \tag{2.37}$$

For example, if $\ell = \frac{1}{2}(y_i - f(x_i))^2$, that is, the loss function is quadratic, then $g_i = y_i - f(x_i)$. While the direction found in (2.37), defines the steepest descent direction, we still need to define the size of the step. The correct definition of the step size is of fundamental importance to obtain good performances in optimisation algorithms. Underestimating the step size can cause the algorithm to need significant more iterations to converge. On the other hand, overestimating it can result in overshooting the minimum, leading to oscillations around it, or even causing divergence from the optimal solution [39]. We do so by maximising the loss function's reduction. Such value can be found solving the following equation using line search [40]:

$$\alpha_{(t)} = \arg\min_{\alpha} \ell\left(\hat{y}^{(t-1)} - \alpha g^{(t)}\right). \tag{2.38}$$

2.3.1 Extreme Gradient Boosting

XGBoost is a decision tree ensemble model [41], that is, it uses decision trees as weak learners. The algorithm minimises the following modified loss function:

$$\mathcal{L}(\varphi) = \sum_{i=1}^{n} \ell\left(y_i, \hat{y}_{i,t-1} + \varphi_t(x_i)\right) + \sum_j \Omega\left(\varphi_j\right) \tag{2.39}$$

$$\Omega\left(\varphi_j\right) = \gamma J + \frac{1}{2}\lambda ||w_j||^2. \tag{2.40}$$

In (2.39), subscript t denotes the t-th learning iteration; furthermore, the loss function is augmented with the regularisation term $\Omega\left(\varphi_j\right)$. We use this term to avoid overly complex decision trees which could lead to overfitting during the training phase. Because of how the regularisation term is set, γ penalises decision trees dividing the feature domain into too many regions, that is, high J values; while, λ penalises terminal nodes, that is, w_j with larger absolute values. These terminal nodes are also called leaves. In (2.40), we used the same notion as in (2.30). At each iteration, decision tree φ^* denotes the tuned decision tree minimising the loss function. It is obtained by first computing the Taylor's expansion of (2.39):

$$\mathcal{L}_t \simeq \sum_{i=1}^{n} \left[\ell\left(y_i, \hat{y}_{t-1}\right) + g_{t-1}\varphi_t\left(x_i\right) + \frac{1}{2}h_{t-1}\varphi_t^2\left(x_i\right) + \Omega\left(\varphi_t\right) + h.o.t.\right]. \tag{2.41}$$

The partial derivatives $\left.\frac{\partial \ell(y_i, \hat{y}_{t-1})}{\partial \hat{y}_{t-1}}\right|_{\hat{y}_{t-1}}$ and $\left.\frac{\partial^2 \ell(y_i, \hat{y}_{t-1})}{\partial \hat{y}_{t-1}^2}\right|_{\hat{y}_{t-1}}$ are related to the gradient and hessian of the loss function, respectively; to simplify the notation we denote them by g_i and h_i, respectively. A needed condition for φ^* to be optimal is that the first derivative of $\mathcal{L}_t$ with respect to φ equals zero. We can then rewrite (2.41) by

removing the first term and rewriting the regularisation term:

$$\tilde{\mathcal{L}}_t = \sum_{i=1}^{n} \left[g_i \varphi_{j,t}(x_i) + \frac{1}{2} h_i \varphi_t^2(x_i) \right] + \gamma J + \frac{1}{2} \lambda \sum_{j=1}^{J} w_j^2 \tag{2.42}$$

The latter equation can be rewritten by using (2.30). Particularly, we consider the case where the decision tree of the t-th iteration has J_1 leaves.

$$\tilde{\mathcal{L}}_t = \sum_{j=1}^{J_1} \left[\left(\sum_{i \in I_j} g_i \right) w_j + \frac{1}{2} \left(\left(\sum_{i \in I_j} h_i \right) + \lambda \right) w_j^2 \right] + \gamma J_1. \tag{2.43}$$

Taking the derivative of (2.43) with respect to w_j:

$$\frac{\partial \tilde{\mathcal{L}}_t}{\partial w_j} = 0 \tag{2.44}$$

$$= \sum_{j=1}^{J_1} \left[\left(\sum_{i \in I_j} g_i \right) + \left(\left(\sum_{i \in I_j} h_i \right) + \lambda \right) w_j \right]. \tag{2.45}$$

The optimal weight of the region j is therefore:

$$w_j^* = - \frac{\sum_{i \in I_j} g_i}{\left(\sum_{i \in I_j} h_i \right) + \lambda}. \tag{2.46}$$

By using the optimal weight computed by (2.46), we obtain the following loss function:

$$\tilde{\mathcal{L}}_t = -\frac{1}{2} \sum_{j=1}^{J_1} \frac{\left(\sum_{i \in I_j} g_i \right)^2}{\left(\sum_{i \in I_j} h_i \right) + \lambda} + \gamma J_1. \tag{2.47}$$

The loss calculated as in (2.47) solves the first problem presented in Section 2.2.1; we now move and present how split points are used. Evaluating all possible split points, which is defined as the exact approach, is inefficient and computationally expensive; to obtain more effective methods, a variety of approximate methods have been developed. Such methods evaluate splits based on percentiles of feature distribution [41]. After finding the set of split candidates, the algorithm computes the score given by each split by using the following equation:

$$\mathcal{L}_{split} = \frac{1}{2} \left[\frac{\left(\sum_{i \in I_L} g_i \right)^2}{\left(\sum_{i \in I_L} h_i \right) + \lambda} + \frac{\left(\sum_{i \in I_R} g_i \right)^2}{\left(\sum_{i \in I_R} h_i \right) + \lambda} - \frac{\left(\sum_{i \in I_I} g_i \right)^2}{\left(\sum_{i \in I_I} h_i \right) + \lambda} \right] - \gamma. \tag{2.48}$$

In 2.48, $I_I = I_L \cup I_R$, that is, I_I is instance set before the split, while I_L, I_R are the instance sets after the split; GB methods choose the split to maximise such score.

Example 3. *Gradient Boosting*
Let us consider a classification problem given by the points shown in Table 2.1. Gradient boosting (GB) algorithms defines an initial guess of the likelihood of a

x	y
1	0
3	0
4	1
7	1
8	1

Table 2.1: Training data available. The classification problem is a binary one.

point to be in the positive class by converting in probability the logarithm of the odds, that is the ratio between the amount of elements belonging to the positive class, and the amount of elements in the negative class. For data in Table 2.1, that is:

$$\hat{p}_0 = \frac{e^{\log\left(\frac{\#\text{class 1}}{\#\text{class 0}}\right)}}{1 + e^{\log\left(\frac{\#\text{class 1}}{\#\text{class 0}}\right)}} = 0.6. \tag{2.49}$$

Given that $\hat{p}_0$ is our first guess, each point will be assigned $\hat{y}_i = 0.6$. We can now calculate the residuals of this first guess, as:

$$r_i = y_i - \hat{y}_i, \tag{2.50}$$

resulting in 0.4 for the points belonging to the positive class, and -0.6 for the points in the negative one. The next step is to train a weak learner, for example, a regression tree, to predict these residuals. However, because the predictions are based on the odds' logarithm (2.49). Suppose we fit a simple decision stump that partitions the space at $x = 5$, assigning a predicted value of 0.4 to points in the positive class and -0.6 to points in the negative class. The update step is:

$$F_1(x) = F_0(x) + \alpha h(x), \tag{2.51}$$

where $F_0(x) = \log(\frac{\hat{p}_0}{1-\hat{p}_0})$, α is the learning rate, and $h(x)$ is the weak learner's prediction. The updated probability estimate is then computed as:

$$\hat{p}_1 = \frac{e^{F_1(x)}}{1 + e^{F_1(x)}}. \tag{2.52}$$

This process iterates, sequentially improving the model at each step by reducing residual errors through additional weak learners. The final boosted model is obtained by summing up all the weak learners' contributions, yielding an improved probability estimate.

2.4 Lyapunov Stability

We now introduce the problem of characterising the stability of dynamical systems. Consider the following autonomous dynamical system:

$$\dot{x} = f(x), \tag{2.53}$$

where $x \in \mathbb{R}^n$, $f : \mathbb{R}^n \to \mathbb{R}^n$ are the state vector and the vector field describing the system's dynamics, respectively. Assuming that the origin of the system is an equilibrium point of the system (2.53), that is, $f(0) = 0$, it is often important that such equilibrium is a stable one. The stability of an equilibrium point is defined as follows:

Definition 1. *(**Stability** [42])*
The equilibrium point $x(t) = 0$ of (2.53) is

- *Stable, if for each $\epsilon > 0$, there is a $\delta > 0$ such that*

$$||x(0)|| < \delta \Rightarrow ||x(t)|| < \epsilon, \forall t \geq 0$$

- *Unstable, if not stable*
- *Asymptotically stable, if it is stable and δ can be chosen such that*

$$||x(0)|| < \delta \Rightarrow \lim_{t \to \infty} x(t) = 0$$

The first definition of stability states that if the trajectories start within an n-dimensional sphere with radius δ and centered at the origin, then the trajectories of the system will not leave the ϵ-radius sphere. Asymptotic stability is a much stronger property, as it ensures that the trajectories of the system will eventually converge to the equilibrium point.

To prove asymptotic stability, one relies on the existence of a Lyapunov function, which is an energy-like function. Particularly, every Lyapunov function must satisfy the conditions in the following theorem, which is known as Lyapunov's stability theorem.

Theorem 1. *([42])*
Let $x = 0$ be an equilibrium point for (2.53) and $X \subset \mathbb{R}^n$ be a domain containing $x = 0$. Let $V : X \to \mathbb{R}$ be a continuously differentiable function, such that:

$$V(0) = 0, \quad \text{and } V(x) > 0, \text{ in } X - \{0\} \tag{2.54}$$

$$\dot{V}(x) = \frac{\partial V}{\partial x}\frac{dx}{dt} \leq 0 \text{ in } X \tag{2.55}$$

Then, $x = 0$ is stable. Moreover, if

$$\dot{V}(x) < 0 \text{ in } X - \{0\} \tag{2.56}$$

then $x = 0$ is asymptotically stable.

From an energy-like standpoint, (2.55) states that over the entire domain X, the system's "energy", described here by Lyapunov function $V(x)$, either dissipates or remains the same. Since the energy of the system does not increase, it is guaranteed that the trajectories of the system will remain in a bounded region, therefore ensuring its stability. On the other hand, (2.56) guarantees continuous energy dissipation in the entire domain except for the equilibrium point where it is 0. Therefore, trajectories converge to the equilibrium point. Lyapunov theory is a widely used framework to study dynamical systems. For example, given the linear time-invariant (LTI) dynamical system $\dot{x} = Ax$, where $x \in \mathbb{R}^n$ is the state vector. The stability of the LTI system can be studied considering a quadratic Lyapunov function candidate $V(x) = x^{\mathrm{T}}Px$, where $P \succ 0$, that is matrix P is positive definite. Taking the time derivative of V, we obtain,

$$\begin{aligned} \dot{V} &= \dot{x}^{\mathrm{T}}Px + x^{\mathrm{T}}P\dot{x} \\ &= x^{\mathrm{T}}A^{\mathrm{T}}Px + x^{\mathrm{T}}PAx \\ &= x^{\mathrm{T}}(A^{\mathrm{T}}P + PA)x \\ &= -x^{\mathrm{T}}Qx. \end{aligned} \tag{2.57}$$

The equation

$$-Q = A^{\mathrm{T}}P + PA \tag{2.58}$$

is known as the Lyapunov equation. For Theorem 1 to hold, it follows that $-x^{\mathrm{T}}Qx^{\mathrm{T}} < 0$, which is equivalent to solving the following linear matrix inequality (LMI) for $P = P^{\mathrm{T}} \succ 0$:

$$A^{\mathrm{T}}P + PA \prec 0. \tag{2.59}$$

Example 4. *Lyapunov Stability* To illustrate the notion of Lyapunov stability, let us introduce the following the following linear dynamical system:

$$\dot{x}_1 = -3x_1 + 2x_2 - x_3 \tag{2.60}$$

$$\dot{x}_2 = +x_1 - 4x_2 + 2x_3 \tag{2.61}$$

$$\dot{x}_3 = -2x_1 + x_2 - 5x_3, \tag{2.62}$$

which yields the matrix:

$$A = \begin{bmatrix} -3 & 2 & -1 \\ 1 & -4 & 2 \\ -2 & 1 & -5 \end{bmatrix}. \tag{2.63}$$

To find the quadratic Lyapunov function $V(x) = x^{\mathrm{T}}Px$, ensuring the stability of (2.60), we need to solve (2.59). The Lyapunov equation requires to solve a strict inequality, however one cannot do so in practice. We overcome this issue by solving the following semi-strict inequality:

$$A^{\mathrm{T}}P + PA \preceq -I, \tag{2.64}$$

where, I is the identity matrix of appropriate dimensions. while also imposing that $P = P^{\mathrm{T}} \succeq \epsilon I$, where $\epsilon > 0$ is an arbitrarily small positive constant, to ensure that P is strictly positive definite. We solve this system using YALMIP [43], while setting $\epsilon = 10^{-4}$, which yields the following matrix:

$$P = \begin{bmatrix} 0.3497 & 0.0991 & -0.0608 \\ 0.0991 & 0.2774 & 0.0538 \\ -0.0608 & 0.0538 & 0.2132 \end{bmatrix}. \tag{2.65}$$

The existence of a positive definite P solving (2.64), guarantees the existence of a quadratic Lyapunov function, ensuring (2.60) is a stable system as per Theorem 1.

2.5 Semidefinite Programming

Many problems in control theory are subject to LMI constraints [44], as for example (2.59). Optimisation problems involving LMI constraints can be solved using semidefinite programmes (SDPs) [45] where the minimisation problem is given by:

$$\text{min.} \qquad c^{\mathrm{T}}x \tag{2.66}$$

$$\text{s.t.} \qquad F(x) \succeq 0, \tag{2.67}$$

$x \in \mathbb{R}^n$ is the decision vector, and $F(x) = F_0 + \sum_{i=1}^{m} x_i F_i$. In the latter, F_i are matrices used to obtain an equivalent representation to $F(x)$, given the decision vector x.

Example 5. Let us consider the matrix:

$$F(x) = \begin{bmatrix} 2 + x_1 + x_1^2 & -x_1 + 2x_2 + x_1x_2 & 1 - x_1 - x_1^2 \\ -x_1 + 2x_2 + x_1x_2 & 3 + 2x_1 + x_1^2 & -1 - x_1 - x_2 - x_1x_2 \\ 1 + x_2 - x_1^2 & -1 - x_1 - x_2 - x_1x_2 & 4 + x_1 + 3x_2 + 2x_1^2 \end{bmatrix}. \tag{2.68}$$

The latter equation can be rewritten as $F(x) = F_0 + \sum_{i=1}^{m} x_i F_i$, by considering the following decision vector:

$$x = \left[x_1,\ x_2,\ x_1^2,\ x_1 x_2\right]. \tag{2.69}$$

Therefore, we obtain the following F_i matrices:

$$F_0 = \begin{bmatrix} 2 & 0 & 1 \\ 0 & 3 & -1 \\ 1 & -1 & 4 \end{bmatrix}, F_1 = \begin{bmatrix} 1 & -1 & -1 \\ -1 & 2 & -1 \\ 0 & -1 & 1 \end{bmatrix}, F_2 = \begin{bmatrix} 0 & 2 & 0 \\ 2 & 0 & -1 \\ 1 & -1 & 3 \end{bmatrix} \tag{2.70}$$

$$F_3 = \begin{bmatrix} 1 & 0 & -1 \\ 0 & 1 & 0 \\ -1 & 0 & 2 \end{bmatrix}, F_4 = \begin{bmatrix} 0 & 1 & 0 \\ 1 & 0 & -1 \\ 0 & -1 & 0 \end{bmatrix}. \tag{2.71}$$

Note that (2.66) and (2.67) define a convex optimisation problem, as the objective function and constraints are convex. Interior-point methods are generally used to solve SDPs [46]; SeDuMi [47] is one of the most popular choices as solver.

2.6 Sum of Squares Programming

Many control problems, require to check nonnegativity of a polynomial, this is generally an NP-hard problem [48]. One popular approach, to relaxing the verification whether a polynomial is nonnegative, is to check if such a polynomial can be written as a Sum of Squares (SOS). We will later show how the existence of such polynomial guarantees nonnegativity. First, we require the following definition.

Definition 2. *(SOS polynomial)*
A polynomial $F(x)$ is said to be a SOS polynomial if the following SOS decomposition exists

$$F(x) = \sum_{i=1}^{N} f_i^2(x). \tag{2.72}$$

Being a SOS polynomial, it follows that $F(x) \geq 0,\ \forall x \in \mathbb{R}^n$. Note that there exist nonnegative polynomials that are not SOS; however SOS decompositions always exist for the following types of problems:

- Polynomials in one variable
- Polynomials of second order
- Polynomials of fourth order in two variables.

By using the SOS approach the focus shifts from proving the nonnegativeness to finding a SOS decomposition.

Proposition 1. *A polynomial $F(x)$ of degree $2d$ is a Sum of Squares if and only if there exists a positive semidefinite matrix Q and a vector of monomials $z(x)$ containing monomials in x of degree less than or equal to d such that*

$$F(x) = z(x)^{\mathrm{T}} Q z(x). \tag{2.73}$$

As illustration, we replicate the example from [49]:

Example 6. Consider the following polynomial function:

$$F(x) = 2x_1^4 + 2x_1^3 x_2 - x_1^2 x_2^2 + 5x_2^4 \tag{2.74}$$

Choosing $z(x) = \begin{bmatrix} x_1^2 & x_2^2 & x_1 x_2 \end{bmatrix}^{\mathrm{T}}$ we obtain:

$$F(x) = \begin{bmatrix} x_1^2 \\ x_1 x_2 \\ x_2^2 \end{bmatrix}^{\mathrm{T}} \begin{bmatrix} q_{11} & q_{12} & q_{13} \\ q_{12} & q_{22} & q_{23} \\ q_{13} & q_{23} & q_{33} \end{bmatrix} \begin{bmatrix} x_1^2 \\ x_1 x_2 \\ x_2^2 \end{bmatrix} \tag{2.75}$$

By comparing (2.74) and (2.75):

$$q_{11} = 2,\ 2q_{12} + q_{33} = -1,\ q_{13} = 1,\ q_{22} = 5,\ q_{23} = 0. \tag{2.76}$$

We then find the coefficients $q_{12},\ q_{33}$ by solving the optimisation problem associated with the following semidefinite programme:

$$\begin{aligned} \min \quad & \mathrm{tr}(A_0 Q) && (2.77)\\ \text{s.t.} \quad & \mathrm{tr}(A_j Q) = c_j, \quad j = 1, \dots, p && (2.78)\\ & Q = Q^{\mathrm{T}} \succeq 0, && (2.79) \end{aligned}$$

where $p = 5$ to satisfy the constraints expressed in (2.76). Some examples of A_j are:

$$A_2 = \begin{bmatrix} 0 & 1 & 0 \\ 1 & 0 & 0 \\ 0 & 0 & 1 \end{bmatrix}, \quad A_4 = \begin{bmatrix} 0 & 0 & 0 \\ 0 & 1 & 0 \\ 0 & 0 & 0 \end{bmatrix}, \tag{2.80}$$

while $c_2 = -1,\ c_4 = 5$.

2.7 Nonlinear Programming

Optimisation problems involving nonlinear dynamical systems are generally hard to solve. Furthermore, there are problems for which a solution cannot be found using analytical approaches. We now introduce some of the theory underlying the tools used in Chapter 5. It is common that dynamical system variables cannot

assume all values in $\mathbb{R}$, that is because hidden or explicit constraints are acting on the system. For example, the control actions available are constrained by physical limitations, such as, physical limitations of aircraft hydraulic actuators. In this Section, we deal with the following general constrained optimisation problem:

$$\min \quad \int_0^T J\left(x\left(t\right), u\left(t\right)\right) dt \tag{2.81}$$

$$\text{s.t.} \quad \dot{x} = f\left(x\left(t\right), u\left(t\right)\right), \quad t \in [0, T] \tag{2.82}$$

$$u(t) \in \mathcal{U}, \quad t \in [0, T] \tag{2.83}$$

$$x(t) \in \mathcal{X}, \quad t \in [0, T] \tag{2.84}$$

In (2.81), where we minimise cost function J to generate optimal control input $u^*(t)$, we denote the state vector as x, the control vector as u. The minimisation problem is constrained to evolve in the specified admissible state region $\mathcal{X}$ and the control actions are required to stay within region $\mathcal{U}$. In this thesis, we solve constrained nonlinear optimal control problems (OCP) using the software CasADi [50]. CasADi is a powerful software that allows to obtain numerical solutions for constrained optimisation problems, it is particularly suited for those problems involving differential equations constraints. In Chapter 5, we employ CasADi after discretising the nonlinear optimisation problem using a direct collocation method (DCM).

2.7.1 Direct Collocation Method

Direct collocation methods (DCM) transcribe the constrained OCP into a sparse nonlinear programming problem, which is then solved through optimisation methods such as nonlinear interior point and sequential quadratic programming (SQP); examples of solvers using these methods are IPOPT [51] and SNOPT [52], respectively. To solve (2.81)-(2.84), first, the problem is discretised in N collocation intervals t_i, and, for each control interval we assume piecewise constant control actions:

$$u(t) = u_k, \quad \text{for } t \in [t_k,\ t_{k+1}], \quad k = 0, 1, \ldots, N. \tag{2.85}$$

On each collocation interval, we further define d collocation points:

$$t_{k,i} = t_k + i h_k, \quad \text{for } k \in \{0, \ldots, N\}, \quad i \in \{0, \ldots, d\}, \tag{2.86}$$

$$h_k = \frac{t_{k+1} - t_k}{d}. \tag{2.87}$$

In (2.87), we allow for a variable time step in between different t_k; however, a fixed-value $h_k = h$ can be set. A crucial step in direct transcription is discretising the

system dynamics (2.82). When using DCMs, we approximate the state trajectory $x(t)$ by a polynomial of order d:

$$p_k(t, c_k) = \sum_{i=0}^{d} c_k \ell_{k,i}(t). \tag{2.88}$$

In (2.88), we denote the vector of polynomial coefficients by $c_k = \{x_{k,0}, \dots, x_{k,d}\}$ and the basis vectors are denoted by $\ell_{k,i}$, in DCMs, Lagrange polynomials are generally used. By construction [53],

$$\ell_{k,i}(t_{k,j}) = \begin{cases} 1 & \text{if } i = j, \\ 0 & \text{if } i \neq j, \end{cases} \tag{2.89}$$

therefore, $p_k(t_{k,i}, c_k) = x_{k,i}$. Moreover, at the first collocation time of each collocation interval, t_k, the following condition must hold:

$$p_k(t_k, c_k) = x_k. \tag{2.90}$$

Constraint (2.90) defines the first coefficient of c_k. The other $d - 1$ coefficients are set by requiring the time derivative of the approximating polynomial to satisfy the state dynamics $\dot{x}(t) = f(x(t), u(t))$. The so-called collocation conditions then becomes:

$$g_k(c_k, x_k, u_k) = \begin{bmatrix} c_{k,0} - x_k \\ \dot{p}_k(t_{k,1}, c_k) - f(c_{k,1}, t_{k,1}, u_k) \\ \vdots \\ \dot{p}_k(t_{k,d}, c_k) - f(c_{k,d}, t_{k,d}, u_k) \end{bmatrix} = 0. \tag{2.91}$$

To guarantee continuity, a final condition must be set on x_{k+1}:

$$x_{k+1} = p_k(t_{k+1}, c_k). \tag{2.92}$$

After transcription, OCP can be written as:

$$\min_{x_k, u_k} \quad \sum_{k=0}^{N-1} l_k(x_k, u_k) \tag{2.93}$$

$$\text{s.t.} \quad s_0 - x_0 = 0 \tag{2.94}$$

$$g_k(c_k, x_k, u_k) = 0, \qquad k = 0, \dots, N-1 \tag{2.95}$$

$$p_k(t_{k+1}, c_k) - x_{k+1} = 0, \quad k = 0, \dots, N-1 \tag{2.96}$$

$$h(x_k, u_k) \leq 0, \qquad k = 0, \dots, N-1, \tag{2.97}$$

where we denote by $l_k(x_k, u_k)$ the contribution to the global loss function at time step t_k, and $h(x_k, u_k)$ is the function constraining the admissible values for the

discrete state trajectory and for the control actions. DCMs return a very large but also very sparse NLP. Modern software tools solve such minimisation problems by using interior point methods. Particularly, the default solver used by CasADi to solve NLPs is `IPOPT` [51].

Example 7. Consider a simple optimal control problem defined by the following dynamics:

$$\dot{x}_1(t) = x_2(t), \tag{2.98}$$
$$\dot{x}_2(t) = u(t). \tag{2.99}$$

Let us consider the problem of minimising the following cost function over the time interval $[0,\ t_f]$:

$$J = \int_0^{t_f} u^2(t)dt. \tag{2.100}$$

Let us set $t_f = 1$, and the boundary conditions to:

$$x_1(t=0) = 0, \tag{2.101}$$
$$x_2(t=0) = 0, \tag{2.102}$$
$$x_1(t=1) = 1, \tag{2.103}$$
$$x_2(t=1) = 0 \tag{2.104}$$

For sake of explanation, let us use a trapezoidal collocation method. The dynamics is therefore approximated as:

$$\frac{x_{1,i+1} - x_{1,i}}{\Delta T} = \frac{x_{2,i+1} + x_{2,i}}{2}, \tag{2.105}$$
$$\frac{x_{2,i+1} - x_{2,i}}{\Delta T} = \frac{u_{i+1} + u_i}{2}. \tag{2.106}$$

In the latter $i = 0, 1, \dots, N-1$, where N is the number of intervals used to discretise the interval $[0, T]$. We can now discretise (2.100):

$$J = \Delta t \sum_{i=0}^{N-1} \frac{u_{i+1} + u_i}{2}. \tag{2.107}$$

Then, the full OCP can be written as:

$$\min_{x_k,u_k} \quad \Delta t \sum_{i=0}^{N-1} \frac{u_{i+1}+u_i}{2} \tag{2.108}$$

$$\text{s.t.} \quad x_{1,0} = 0 \tag{2.109}$$

$$x_{2,0} = 0 \tag{2.110}$$

$$\frac{x_{1,i+1}-x_{1,i}}{\Delta t} - \frac{x_{2,i+1}+x_{2,i}}{2} = 0, \quad i = 0, \dots, N-1 \tag{2.111}$$

$$\frac{x_{2,i+1}-x_{2,i}}{\Delta t} - \frac{u_{i+1}+u_i}{2} = 0, \quad i = 0, \dots, N-1 \tag{2.112}$$

$$x_{1,N} = 1 \tag{2.113}$$

$$x_{2,N} = 0. \tag{2.114}$$

The latter system can be solved using standard optimisation software such as IPOPT [51], and SNOPT [52]

Chapter 3

Automatic Detection of Electrodermal Activity Events During Sleep

This chapter was published as: "Piccini, J., August, E., Noel Aziz Hanna, S. L., Siilak, T., & Arnardóttir, E. S. (2023). Automatic Detection of Electrodermal Activity Events during Sleep. Signals, 4(4), 877–891. https://doi.org/10.3390/signals4040048".

Abstract

Currently, there is significant interest in developing algorithms for processing electrodermal activity (EDA) signals recorded during sleep. The interest is driven by the growing popularity and increased accuracy of wearable devices capable of recording EDA signals. If properly processed and analysed, they can be used for various purposes, such as identifying sleep stages and sleep-disordered breathing, while being minimally intrusive. Due to the tedious nature of manually scoring EDA sleep signals, the development of an algorithm to automate scoring is necessary. In this paper, we present a novel scoring algorithm for the detection of EDA events and EDA storms using signal processing techniques. We apply the algorithm to EDA recordings from two different and unrelated studies that have also been manually scored and evaluate its performances in terms of precision, recall, and F_1 score. We obtain F_1 scores of about 69% for EDA events and of about 56% for EDA storms. In comparison to literature values for scoring agreement between experts, we observe a strong agreement between automatic and manual scoring of EDA events and a moderate agreement between automatic and manual scoring of EDA storms. EDA events and EDA storms detected with the algorithm can be further processed and used as training variables in machine learning algorithms

to classify sleep health.

3.1 Introduction

Thermoregulation is a delicate task, deviations from a relatively tight temperature range can lead to organ failure and death. During the wakefulness, thermoregulation keeps brain and organ temperatures in homeostasis. During sleep, thermoregulation aligns core body temperature (CBT) with the circadian rhythm [54]. Notably, during rapid eye movement (REM) sleep, a significant reduction in thermoregulatory capabilities has been observed. This decrease has been explained through energy considerations: During REM sleep, the brain's activity resembles wakefulness and it requires more energy, which reduces the energy available for thermoregulation [23]. One of the mechanisms used by the sympathetic nervous system (SNS) to decrease CBT is sweat, which enables heat dissipation through vaporisation [55]. Abnormal sweat patterns have been observed in connection with sleep-related breathing disorders [18]. Particularly, obstructive sleep apnoea (OSA) is known to cause excessive sweating [56]. A person with OSA repeatedly stops breathing [57], which hinders heat dissipation by means of exhalation and triggers heat dissipation by means of sweating instead.

Since, during sleep, sweat dynamics vary depending on sleep stage and health conditions, analysing sweat dynamics provides means to determine the latter two. Furthermore, sweat dynamics strongly relates to SNS activations, which provides a unique opportunity to study the SNS with minimal external disturbance. A proxy for capturing changes in sweat production is measuring fluctuations in the electrical properties of the skin caused by changes in skin hydration levels. They are measured indirectly either by measuring the resistance or the conductance of the skin, after externally applying a voltage (exosomatic method), or by measuring the voltage of the skin without externally applying a voltage (endosomatic method). One commonly refers to the resulting signal as the electrodermal activity (EDA) signal [14, 58]. Despite being the less commonly used method, the endosomatic method is easier to implement [59] and provides "more" physiological insight. We refer the reader to [58] for more details about the two methods.

First experimental observations of EDA date back to 1860s [14]. However, using the EDA signal became popular only in recent years due to the rise of wearable devices able to record EDA signals [60, 59]. During wakefulness, the EDA signal has been used to monitor students' engagement in the classroom [61], to detect epileptic seizures [62], to assess task-induced stress [63], and to classify emotions [64], to cite but few applications. While the use of the EDA signal during wakefulness is relatively well established now, the use of the EDA signal for assessing sleep is a relatively new field and most algorithms have been developed in the last two years. During sleep, EDA signals are typically used to detect sleep

stage [65], to predict sleep quality [66], and to predict the presence of OSA [67].

Analysing or scoring EDA sleep recordings mainly consists of detecting EDA events and EDA storms. EDA events are oscillations in the EDA signal with well-defined amplitude and frequency [68]. These oscillations are not uniformly spread throughout the night. They are more commonly found in non-REM sleep 2, slow wave sleep (SWS), and late-night REM sleep [69, 70]. Moreover, it has been observed that abnormal EDA patterns are caused by OSA [71]. EDA storms are time intervals with a significant number of EDA events. They have been first described by Burch [72] as consisting of "a minimum of 5 galvanic skin response peaks per minute for ten consecutive minutes of sleep". Currently, several alternative definitions, both, for EDA events and EDA storms exist; we refer the interested reader to [73]. In this work, because we apply the endosomatic method for recording the EDA signal, we use the EDA event definition given in [68]; that is, we consider changes in skin potential with amplitude $> 50\ \mu$V and duration > 1.5 s. The endosomatic method is less commonly used, because it records oscillations that are not only monophasic but also biphasic or triphasic and, thus, the recorded EDA events are more difficult to interpret. On the other hand, as mentioned previously, it provides "more" physiological insight. While for exosomatic recordings, several algorithms for the detection of EDA events have been developed using signal processing [74], model-based analysis [75], and convex optimisation [76], to our knowledge, none have been developed for endosomatic recordings. Note that several alternative definitions of an EDA event have been proposed in the literature for exosomatic recordings. A summary is given in [73].

A common problem that affects EDA recordings, particularly, ones of longer duration, is the presence of artefacts in the signal, that is, the presence of sudden and out-of-scale spikes. Artefacts have different causes [70]. The most prominent ones are movements during sleep and a poor connection between skin and electrodes. To address this problem, supervised as well as unsupervised machine learning (ML) techniques have been proposed for artefact detection in EDA signals [77, 74].

In this paper, we present a novel algorithm for the automatic detection of EDA events in endosomatic recordings. We use a traditional signal processing approach rather than a supervised ML one for two reasons. The first one is the relative scarcity of scored endosomatic EDA sleep signal datasets. Manual scoring of EDA events is traditionally not performed due to the difficulty of distinguishing EDA events from artefacts, the tediousness of scoring whole-night EDA signals, and the difficulty of interpreting collected information. The second reason is that the scoring that provides labels for ML algorithms might be incomplete or even wrong, due to the complexity of the EDA signal. As in [69], we use wavelet transforms (WT) to identify and remove artefacts. The basic idea behind wavelet theory is to decompose the signal into a set of wavelets, which are "brief oscillations", in order to describe it [30, 78]. After removing artefacts, we use the Fourier Transform

(FT) to evaluate the oscillations in terms of frequency and amplitude. We then use the definitions given by Sano and colleagues [73] to detect EDA events and EDA storms. Finally, we validate our algorithm against manual scorings. We use data from, both, healthy participants and participants with OSA. The participants diagnosed with OSA had various severities of OSA, ranging from mild to severe.

The remainder of the paper is organised as follows. In Section 3.2.1, we present the data used in this work, the instrumentation used to collect it, and the guidelines used to score EDA signals. In Section 3.2.2 and Section 3.2.3, we introduce the theoretical foundations of WT theory and the definition of EDA events. In Section 3.2.4, we present the algorithm. Sections 3.2.5 - 3.2.9 describe in detail the different parts of the algorithm and the performance indices used to evaluate the algorithm in Section 3.2.10. The results are presented in Section 3.3 and then discussed in Section 3.4. Finally, Section 3.5 concludes the paper.

3.2 Materials and Methods

3.2.1 Data Collection

We used data collected in two different research studies. One dataset consists of 20 scored polysomnography (PSG) recordings from a study that has been carried out in Iceland in 2005 [56]; it contains *.ebm files. The other dataset consists of 30 scored PSG recordings that were made by the Sleep Revolution Project [79] team in 2021-2022. The recordings were exported from Noxturnal software (noxmedical.com) as *.edf files [80]. A representative EDA signal is shown in Fig. 3.1.

EDA manual scoring was performed using either Somnologica software (Somnologica Science 3.3.1; Flaga Inc., Reykjavik, Iceland) for the 2005 recordings or Noxturnal software (Nox Medical, Reykjavik, Iceland) for the 2021-2022 recordings. The sleep technologists applied a high-pass filter with cut-off frequency $f_{h,c}$ set to 0.3 Hz and a low-pass filter with cut-off frequency $f_{l,c} = 10$ Hz. After filtering the signal, they used the following definition: An EDA event is a change in skin potential > 50 μV and of duration > 1.5 s [56]. Sleep technologists categorised sleep stages using the recommended scoring rules [81, 82]. For the automatic signal analysis, segments labelled “awake” were removed.

The data collected in 2005 is described in [56]. Recordings from the Sleep Revolution Project are of persons with either diagnosed or suspected OSA. The average apnoea-hypopnoea index (AHI) is 14.6, the standard deviation is 14.7, and values range from 0.9 to 57.3. Both studies received the approval of the National Bioethics Committee and the Data Protection Authority of Iceland (Sleep Revolution VSN-070). Informed consent was obtained by participants prior to data collection.

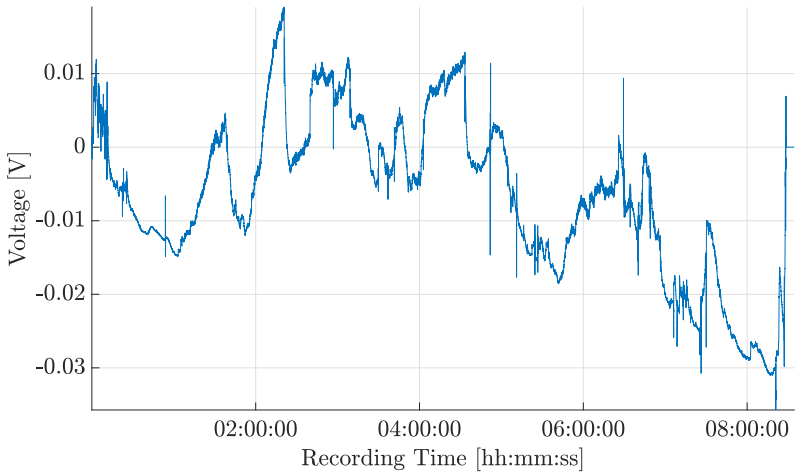

Figure 3.1: A sample raw EDA signal from a single night PSG recording is shown.

3.2.2 Wavelet Transforms

In the literature, WTs have been applied to various biophysical signals, such as electrocardiogram and electromyography signals [83, 84]. Recently, WTs have been used for pre-processing EDA signals, particularly, for artefact detection [85, 74]. By properly choosing the mother wavelet, we can distinguish those parts of the signal that resemble the shape of measurement noise or of motion artefacts in order to exclude them.

In this work, we use the Discrete Wavelet Transform (DWT) and the Stationary Wavelet Transform (SWT). In the following, we provide a brief description of the WT, a detailed introduction to wavelets can be found in [86]. The WT is similar to the Fast FT (FFT) or Discrete FT in the sense that they are all linear operations. While the basis functions of FFT are sines and cosines, WTs allows the use of more complex basis functions [87]. The other main difference between the FFT and the DWT is that wavelets are localised in space. The sine and cosine functions used in the FT are not. Moreover, when using FFT coefficients to reconstruct a signal, sharp changes in the original signal may cause the appearance of ringing artefacts in the reconstruction, which can be confused with actual artefacts. A popular mother wavelet used to limit the effect of sharp changes due to measurement noise is the *haar* function [77], which is shown in Fig. 3.2.

In this work, we employ the SWT for the identification of motion artefacts in the data. This choice was motivated by the time-invariant nature of these artefacts, as well as their lack of susceptibility to causing undesirable ringing artefacts. As

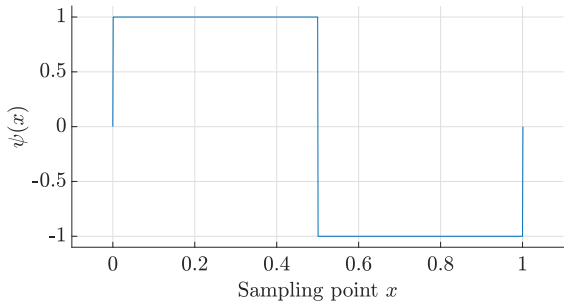

Figure 3.2: The figure shows that *haar* function. We use it to limit the effect of sharp changes due to measurement noise.

candidate mother wavelets, we use the functions *db44* and *coif3*, see Fig. 3.3 and Fig. 3.4, respectively. Both wavelet functions are frequently used in biomedical applications. Moreover, the *coif3* wavelet resemblances the characteristic shape of motion artefacts [85, 88].

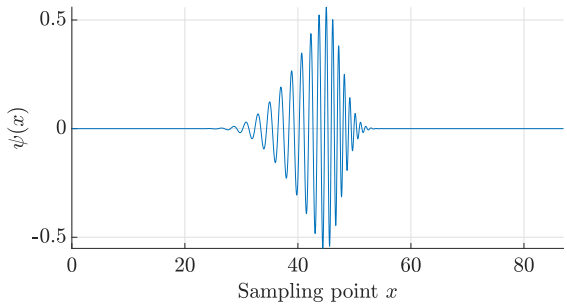

Figure 3.3: The *db44* function.

After choosing the candidate mother functions, the choice of decomposition level (DL) is most critical. We use the DL with minimum entropy as recommend in [89]. Additionally, the entropy of a signal is related to the number of coefficients needed to properly describe the signal [89]. Therefore, choosing the DL with lowest entropy allows to minimise the number of coefficients needed to represent the signal. In this work, we considered Shannon entropy as measure. It is defined by

$$E_{sh} = -\sum_i y_i^2 ln(y_i^2), \tag{3.1}$$

where y is the signal [89]. For different DL, the Shannon entropy of the signal

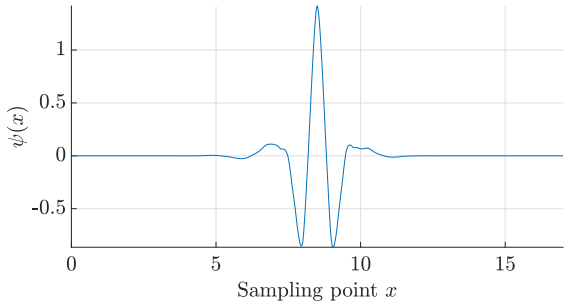

Figure 3.4: The *coif3* function.

shown in Fig. 3.1 is given in Table 3.1, where the entropy values for $db44$ and $coif3$ are similar. Importantly, we obtain similar results for all other EDA signals in the datasets (not shown). Thus, DL 1, which has the lowest entropy, seems to be the most appropriate for artefact detection. Since *coif3* resemblances the characteristic shape of motion artefacts, we use it for artefact detection, that is, we exploit the similarity between this mother wavelet and motion artefacts. Note that the *haar* function was used to smooth the signal.

Mother Function	***DL 1***	***DL 2***	***DL 3***	***DL 4***
db44	0.0059	0.0228	0.0815	0.3572
coif3	0.0060	0.0219	0.0789	0.3599

Table 3.1: Shannon Entropy for different mother functions and decomposition levels for the signal shown in Fig. 3.1, measured in bits.

3.2.3 Events Frequency Range

As mentioned previously, EDA signals can be recorded either exosomatically or endosomatically. Most devices and wearables, such as the Empatica E4 watch and the WatchPAT^{TM}, record EDA exosomatically. The recorded signal is simpler, because it does not distinguish between monophasic, biphasic, and triphasic oscillations. However, these three different types of oscillations have different physiological meaning. Since endosomatic recording distinguishes between them [90], it is more valuable from an information theoretical point of view. The EDA signals considered in this work were recorded endosomatically. The procedure is described in the paper by Arnardóttir and colleagues [56].

For an EDA sleep signal oscillation to be considered an EDA event, it must have a certain duration. In the literature, different values are given for this duration. Edelberg suggests 1.2 s to 4 s [91], while Venables and Christie suggest 1 s to 3 s [92]. We use these values to define the following EDA oscillations-frequency range-of-interest:

$$\begin{aligned} f_{s,min} &= \frac{1}{\max(3\text{ s}, 4\text{ s})} = 0.25\text{ Hz}, \\ f_{s,max} &= \frac{1}{\min(1.2\text{ s}, 1\text{ s})} = 3\text{ Hz}. \end{aligned} \tag{3.2}$$

This means that we consider triphasic oscillations that last for around 1 s and monophasic oscillations that last for around 4 s. We assume that significant signal fluctuations of higher frequencies are either motion artefacts, recording errors, or non-relevant EDA events.

3.2.4 Algorithm

The algorithm was developed using MATLAB® [93]. The respective flow diagram is shown in Fig. 3.5, while a brief description of the different parts is given in the following.

- **Data Loading.** First, files containing the EDA signal, the manually scored events, and sleep stages are loaded. After loading, the task Signal Pre-processing is performed.
- **Signal Pre-Processing.** WTs are used to smooth the original signal, before down-sampling the signal and applying a band-pass filter. A *haar* discrete WT (DWT) is applied to the filtered signal, detail coefficients are hard-thresholded, and an inverse DWT is applied to obtain a smoothed signal.
- **Artefact Detection.** Motion artefacts are detected using WTs on the non-smoothened signal. Parts of the EDA signal that strongly resemble a specific wavelet are considered artefacts.
- **Event Detection.** The pre-processed signal is segmented into non-overlapping time windows. Then, the FFT is applied to each segment and thresholds are used in the time domain as well as frequency domain to detect EDA events. Respective parts of the signal are stored in an array.
- **Artefact Removal.** Signal segments that are considered artefacts are removed from above array.
- **Wake Epoch Removal.** Signal segments marked as waking periods are also removed.

- **Storm Detection.** Finally, EDA storms are detected using respective definition.

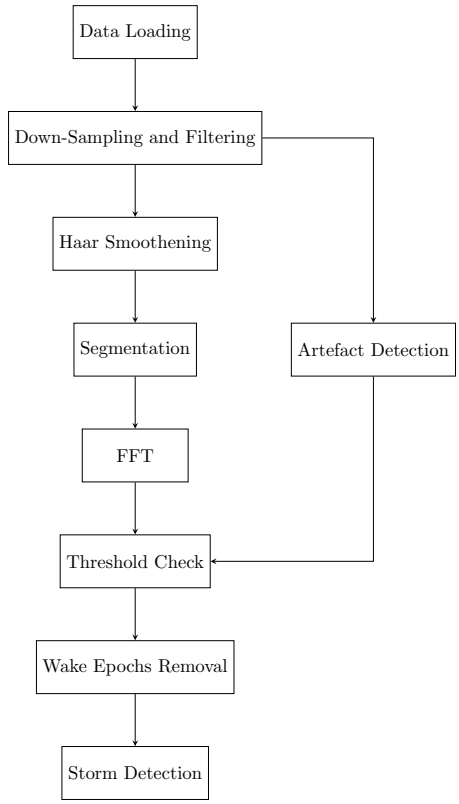

Figure 3.5: Flow diagram of the algorithm developed in this work. After applying a band-pass filter, the signal is processed in two different ways in parallel. One branch is for EDA event detection, while the other one is for motion artefact detection. The outputs of the two branches are then merged and artefacts removed. The final steps consist of removing periods of wakefulness and EDA storm detection.

3.2.5 Re-Sampling

The EDA signals from the two different studies are sampled at different frequencies. The sampling frequency in the 2005 study is 10 Hz, while the one in the study that was performed as part of the Sleep Revolution Project is 200 Hz. To reduce

computational time, the latter signals are down-sampled to 35 Hz using the MATLAB® function `resample`. The Nyquist-Shannon theorem states that it is possible to reconstruct oscillations of 3 Hz with a sampling frequency as low as 6 Hz. However, such low sampling frequencies cannot distinguish between the phasic and tonic components and, therefore, leading to a significant loss of information [94]. Because of this, we down-sample the signals from 200 Hz to 35 Hz. Note that while a higher sampling frequency guarantees more accurate readings, there are no phenomena of interest at frequencies > 35 Hz.

3.2.6 Signal Pre-Processing

As mentioned in the introduction, event detection is performed by evaluating the results of applying the FFT to 4 s segments. To avoid causing ringing, during the pre-processing phase, we use the DWT with the *haar* function as mother function. After computing DWT approximate coefficients and detail coefficients, the latter ones are hard-thresholded by factor t, where

$$t = \sigma \cdot \sqrt{2 \cdot ln(n)}, \tag{3.3}$$

σ is the standard deviation of the detail coefficients, and n is the length of the signal [95]. After hard-thresholding, an inverse DWT is applied and the signal reconstructed.

We then apply a bandpass filter, with range $[0.25 \text{ Hz} - 10 \text{ Hz}]$, to reduce the contribution of noise as well as of signal drift. Furthermore, we set the filter upper frequency limit to 10 Hz to be more consistent with the data collected in the 2005 study. Bandpass filtering concludes the pre-processing phase.

3.2.7 Artefact Detection

Applying WT to a segment of the signal that has a shape similar to the one of the chosen mother wavelet will lead to coefficients with larger magnitude. Therefore, for artefact detection, we used *coif3* as mother function, since it resembles typical motion artefacts [85]. After computing the SWT coefficients, they are thresholded and non-zero signal segments are marked as artefacts. Signal segments with significant high-frequency contributions – that is, for frequencies > 3 Hz – are considered to be artefacts and are labelled accordingly. An example of an artefact is shown in Fig. 3.6.

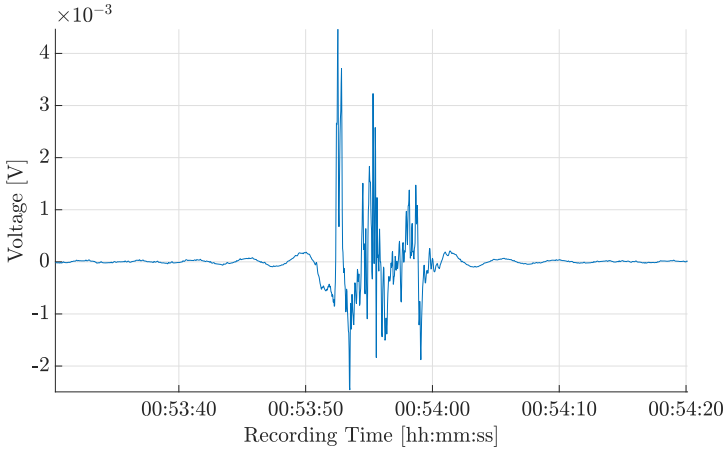

Figure 3.6: Example of an artefact. The signal exhibits a sudden voltage drop followed by high-frequency oscillations.

An example of an artefact detected in the frequency domain is shown in Fig. 3.7. The power spectrum has high frequency contributions that are larger than the threshold. Consequently, this specific 4 s segment is marked as being an artefact. Note that we also consider the 10 s of signal preceding and the 10 s of signal succeeding an artefact as being an artefact. The reason behind is that, often, the onset of artefact oscillations as well as their end are marked by weak oscillations that could be erroneously considered events.

3.2.8 EDA Event Detection

As mentioned previously, EDA events have frequencies in the range of 0.25 Hz to 3 Hz. Within this frequency range, we only consider EDA oscillations whose amplitudes are between 50 μV and 500 μV. For event detection in the frequency domain, we segment the signal and transform individual signal segments using the FFT. To obtain the segments, the signal is sliced into non-overlapping time windows of constant duration $T = 4$ s. This allows us to detect events with a frequency as low as 0.25 Hz.

Then, we multiply the FT coefficients by $2/N$, where N is the number of coefficients, and compute their absolute value. If any of these values lies between 50 μV and 500 μV then the segment is marked as an event; see Fig. 3.8 and Fig. 3.9. In Fig. 3.8, the displayed signal segment has oscillations of frequencies between 0.25 Hz and 3 Hz whose amplitudes are significant. Hence, the algorithm labels this segment as an EDA event. In Fig. 3.9, the power spectrum in the frequency

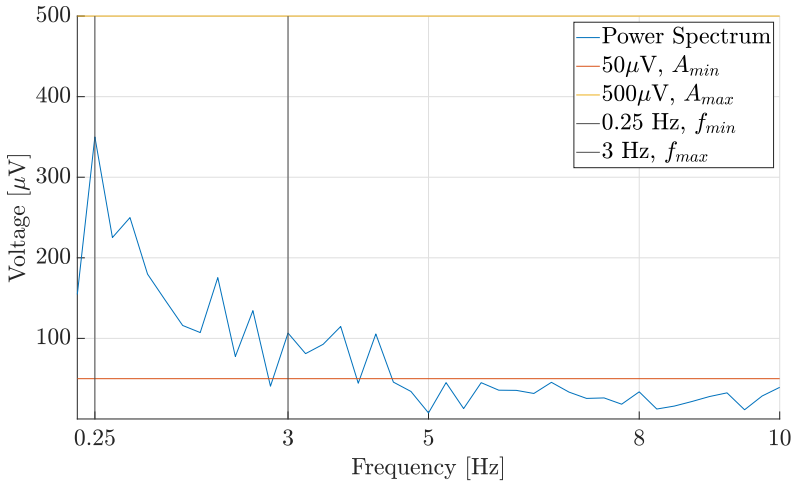

Figure 3.7: Example of an artefact's power spectrum. The high-frequency contribution exceeds the threshold. Thus, the segment is labelled an artefact.

range between 0.25 Hz and 3 Hz does not show oscillations of relevant amplitudes. Hence, this segment is not labelled as an EDA event.

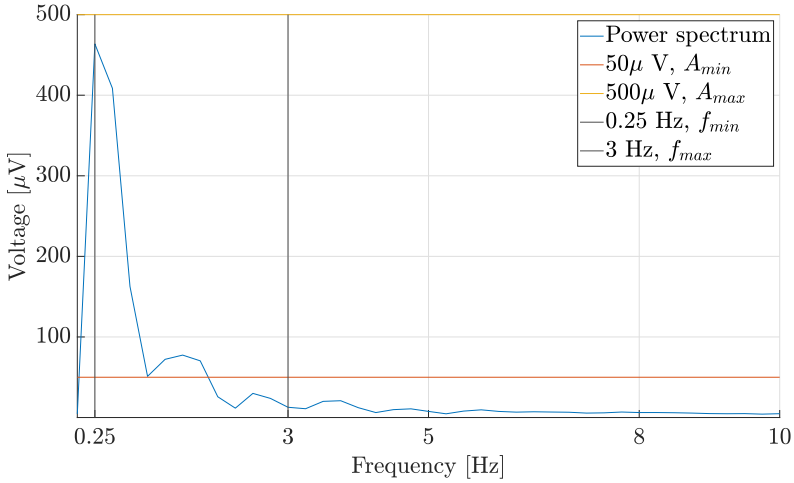

Figure 3.8: An EDA event is detected: The power spectrum of frequencies between 0.25 Hz and 3 Hz exceeds the EDA event threshold.

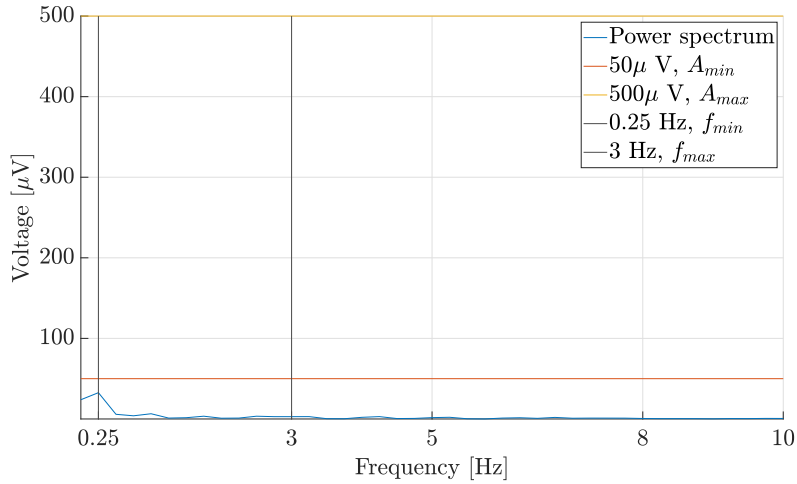

Figure 3.9: An EDA event is not detected: The power spectrum does not exceed the EDA event threshold.

3.2.9 EDA Storm Detection

Detection of EDA storms is important for using the EDA signal to assess key aspects of sleep health such as the presence of disordered breathing, one of which is OSA [67]. Our algorithm labels a one-minute window, that contains two or more EDA events, as an EDA storm. An example of an EDA storm is shown in Fig. 3.10.

3.2.10 Performance Indices

We use three indices to quantify algorithm performances, which we explain in the following. We compute them for, both, EDA event and EDA storm detection. For this evaluation, we use manual scoring. Note that EDA storms were not scored during the manual EDA scoring process. For this reason, we devised a pseudo-manual EDA storm scoring by considering a one-minute window, that contains two or more EDA events, being an EDA storm, just as before in the automatic scoring.

3.2.10.1 Precision

Precision P is the ratio between the number of true positives and the number of predicted positives. In this work, the number of true positives is the number of

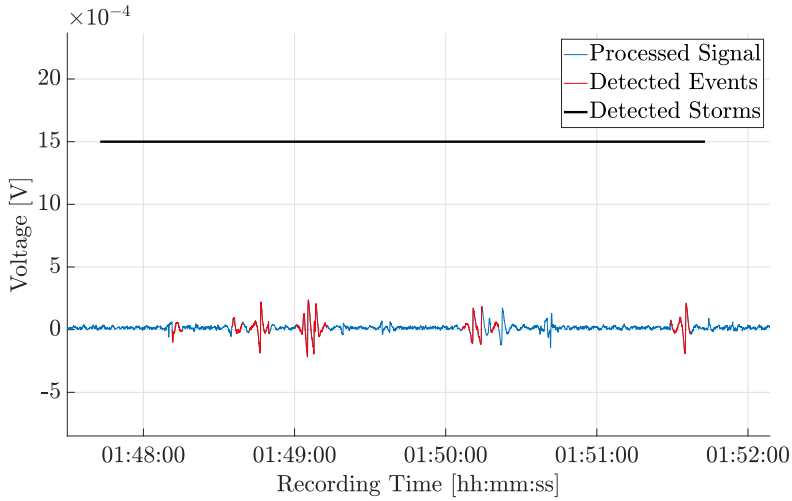

Figure 3.10: An example of an EDA storm.

EDA events (storms) detected by the algorithm that overlap with manually scored EDA events (storms). We denote this number by $n_{overlap,e}$ ($n_{overlap,st}$) and the number of manually scored EDA events (storms) by $n_{manual,\,e}$ ($n_{manual,\,st}$). The number of predicted positives is the number of automatically detected EDA events (storms). We denote this number by $n_{detected,e}$ ($n_{detected,st}$).

$$P = \frac{n_{overlap}}{n_{detected}}. \tag{3.4}$$

3.2.10.2 Recall

Recall R is the ratio between the number of true positives and the number of actual positives, which is the number of manually scored EDA events (storms) in this work.

$$R = \frac{n_{overlap}}{n_{manual}}. \tag{3.5}$$

3.2.10.3 F_1-Score

The F_1 score is the harmonic mean of precision and recall.

$$F_1 = 2 \cdot \frac{PR}{P + R}. \tag{3.6}$$

3.3 Results

3.3.1 Algorithm Performance

The algorithm's performances are summarised in Table 3.2 and Table 3.3. Table 3.2 shows the performance when the algorithm is used to score the recordings from the 2005 study. Table 3.3 shows the performance when the algorithm is used to score the collected recordings within the Sleep Revolution Project.

Index	Average	Median	Minimum	Maximum	Standard Deviation
P_{event}	73.7%	77.4%	11.1%	100%	19.5%
R_{event}	66.1%	67.4%	8.9%	95.3%	22.4%
$F_{1_{event}}$	68.9%	68.9%	9.9%	100%	20.5%
P_{storm}	50.3%	47.6%	0.0%	100%	26.6%
R_{storm}	62.6%	65.4%	18.8%	100%	18.2%
$F_{1_{storm}}$	51.5%	53.6%	0.0%	82.4%	20.2%

Table 3.2: The performance of the algorithm scoring EDA signals from the 2005 study.

Index	Average	Median	Minimum	Maximum	Standard Deviation
P_{event}	68.9%	76.5%	16.7%	91.8%	19.7%
R_{event}	77.8%	79.8%	16.7%	96.1%	14.7%
$F_{1_{event}}$	71.4%	78.0%	16.7%	89.7%	15.6%
P_{storm}	49.8%	49.5%	0.0%	97.2%	26.0%
R_{storm}	75.9%	78.9%	0.0%	100%	20.7%
$F_{1_{storm}}$	56.6%	57.6%	0.0%	95.6%	22.1%

Table 3.3: The performance of the algorithm scoring EDA signals recorded by the Sleep Revolution Project team.

To assess whether there is a statistically significant difference in performance when the scoring algorithm is applied to either dataset, we perform a two-sample *t*-tests, where we compare a set of indices from one study to the respective set from the other study. The results are shown in Table. 3.4. We discuss them in the following section.

3.4 Discussion

The *p*-values in Table 3.4 show that the differences in Precision and F_1 performance of the automatic scoring algorithm, when applied to either one of the two

$\mathbf{P_{event}}$	$\mathbf{R_{event}}$	$\mathbf{F1_{event}}$	$\mathbf{P_{storm}}$	$\mathbf{R_{storm}}$	$\mathbf{F1_{storm}}$
0.3937	0.0300	0.6167	0.9458	0.0237	0.5012

Table 3.4: The p-values of two-sample t-tests are shown, where we compare a set of indices from one study to the respective set from the other study.

datasets, are not statistically significant. This suggests that our algorithm is robust to differing sampling frequencies and sleep technologists, who score the EDA signals. When applying the algorithm to the EDA recordings from the two different studies and evaluating its performance, we obtain F_1 scores with an average of 68.9% and of 71.4% for EDA events and of 51.5% and 56.6% for EDA storms. The low agreement for EDA storm detection and, to a lesser extent, the moderate agreement for EDA event detection are partially misleading. The low average of $F_{1_{storm}}$ scores stems from the definition of F_1 scores and, thus, is caused by having some low P_{storm} values while the R_{storm} average is similar to the R_{event} average. The consistency between the two recall performances further confirms that the relatively low average value for $F_{1_{storm}}$ scores is exclusively caused by the existence of some low P_{storm} value. They arise because EDA storm automatic and manual scoring is different.

One issue is the absence of a definition in the literature for the maximum length of an EDA event. Because of this, a manual scorer might label as one EDA event what the automatic scoring algorithm presented in this paper labels as multiple EDA events. Also, since manual scorers do not score EDA storms but rather consider them a long-lasting EDA event, we consider a long-lasting manually scored EDA event to be an EDA storm. This differs from how the algorithm scores EDA storm, as it rather follows what the literature considers an EDA storm. We graphically represent this in Fig. 3.11. The figure shows another issue in EDA event detection. While the manual and the automatic scores identify the EDA events, the associated performance indices are low because of misalignment in the onset of the detected EDA events.

In the literature, agreement between different sleep technologists when scoring sleep stages is categorised using the intraclass correlation coefficient, as outlined by Kuna et al. [96]: Poor agreement for 0-0.2; fair agreement for 0.3-0.4, moderate agreement for 0.5-0.6, strong agreement for 0.7-0.8, and almost perfect agreement for >0.8. Based on these ranges and using the F_1 score as the relevant performance measure, our algorithm achieves strong agreement for EDA event detection and moderate agreement for EDA storm detection when applied to the dataset from the Sleep Revolution Project. For the 2005 dataset, the agreement for EDA event detection is moderate; however, the value is almost in the strong agreement range. The agreement for EDA storm detection remains moderate. Notably, we believe that the performance measures presented in Table 3.2 and Table 3.3 are

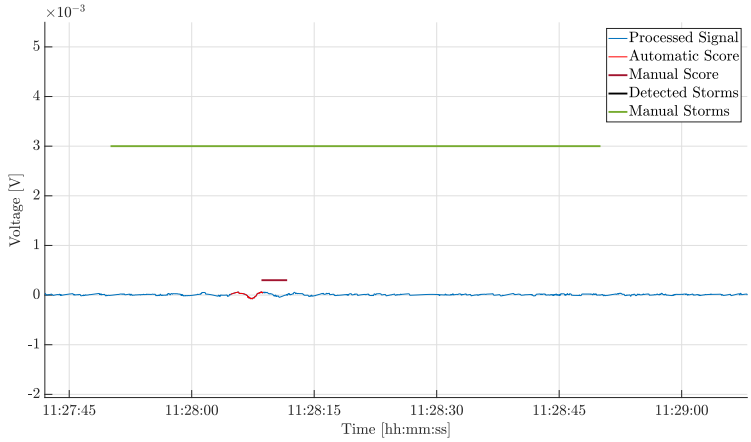

Figure 3.11: Difference between manual and automatic scoring.

rather conservative ones. In [67], we show that there is a strong correlation between EDA events and EDA storms detected by our algorithm and sleep stages or the presence of OSA. It might be possible to increase accuracy in such applications might be obtained by combining the EDA-based classifier with ML models trained on different signals. For example, one could consider the electroencephalography (EEG) signal or the electromyography signal [97, 98]. Finally, combining predictions made using either the EDA signal or the EEG signal might yield new insight on the connections of the different regulatory processes occurring in the brain during sleep [99].

3.5 Conclusions

We presented an algorithm that automatically scores EDA events and EDA storms. To our knowledge, a scoring algorithm for EDA recordings obtained by the endosomatic method has not been developed previously. Including EDA in sleep studies is not norm because of its relative novelty in sleep research and because scoring it is tedious and has not been properly standardised. We believe that the tool presented in this work provides valuable means for inclusion by allowing for more accurate and faster manual scorings. After its employment, sleep technologists can import the automatic scoring into the scoring software and briefly check whether wrongly detected EDA events need to be removed. The next step is to make the algorithm clearly highlight areas of no interest and grey zones in the signal, where there is significant activity that might qualify as an event and needs the attention of an expert technologist.

Moreover, due to its nature, the endosomatic method is much suitable to be included in wearables, as it does require to externally apply a voltage. Indeed, a few commercial devices already measure EDA. However, due to its complex nature, the signal has not been used for assessing sleep, yet. We believe that our work is a first stepping stone in this direction.

ML models are the current state-of-the-art computational methods for sleep research. However, research on selecting training variables that effectively reflect physiological phenomena during sleep is scarce, particularly, in the area of EDA. Given also the difficulty of and ambiguity in scoring endosomatic EDA sleep signals, training dataset might not be sufficiently correct to guarantee a correct learning process. For this reason, we abstained from using ML and rather obtained the measures used in this work from the literature.

Feature engineering is a pivotal step in optimising ML models. It has been shown that simpler and more interpretable ML models outperform complex models when accompanied by ad-hoc feature engineering. Our algorithm detects EDA events and EDA storms, phenomena known to be associated with physiological processes during sleep, which can be used for feature engineering in the future.

Our algorithm has been already successfully used to detect OSA. Thus, it opens the possibility of not only detecting but also monitoring the progression of OSA without invasive measurements. Moreover, we believe that better integrating EDA in sleep research will allow us to gain more physiological insight, for instance, by means of network physiology, which investigates the interactions between different physiological systems. Although sleep studies record many different physiological signals, network physiology has been rather neglected. Investigating changes in topology of the physiological network when EDA events and EDA storms occur will help to better characterise the processes underlying thermoregulation and understand its interaction with other physiological systems.

Thus, in the future, we believe that automatic scoring algorithms, such as the one presented in this work, will much aid the work of manual scorers, ultimately taking over this tedious task. Their use will also allow a more thorough standardisation of scoring and, thus, for better interpretability of scoring results from different studies. Finally, they will also be used to optimise ML algorithms for better determining sleeps stages and disease severity, while allowing for a better understanding of underlying physiological processes by facilitating the analysis of correlation between different physiological signals relevant to sleep. We therefore see the work presented in this paper as a first stepping stone in this direction.

Chapter 4

Using the electrodermal activity signal and machine learning for diagnosing sleep

This chapter was published as: "Piccini, J., August, E., Óskarsdóttir, M., & Arnardóttir, E. S. (2023). Using the electrodermal activity signal and machine learning for diagnosing sleep. Frontiers in Sleep, 2. https://doi.org/10.3389/frsle.2023.1127697".

Abstract

The use of the electrodermal activity (EDA) signal for health diagnostics is becoming increasingly popular. The increase is due to advances in computational methods such as machine learning and the availability of wearable devices capable of better measuring EDA signals. One field where work on EDA has significantly increased is sleep research, as changes in EDA are related to different aspects of sleep and sleep health such as sleep stages and sleep-disordered breathing; for example, obstructive sleep apnoea (OSA). In this work, we used supervised machine learning, particularly the extreme gradient boosting (XGBoost) algorithm, to develop models for detecting sleep stages and OSA. By complementing a standard generic statistical feature set with EDA-specific variables, we obtained an average macro F1-score of 57.5% and 66.6%, depending on whether we considered five or four sleep stages, respectively. When detecting OSA, regardless of the severity, the model reached an accuracy of 83.7% or 78.4%, depending on the measure used to classify the participant's sleep health status. The research work presented here provides further evidence that, in the future, most sleep health diagnostics might well do without complete PSGs studies, as wearables can detect well the EDA signal.

4.1 Introduction

Electrodermal activity (EDA) is one of the longest-known and most accessible physiological signals [14]. EDA reflects changes in skin potential due to sweating, which, during sleep, has a thermoregulatory function. Eccrine sweat glands, the sweat glands that are activated during sleep [14], are innervated by the sympathetic nervous system (SNS) only, with no parasympathetic input [100]. Despite this direct connection between EDA and the SNS during the night, the signal has been so far mostly used in studies of diurnal phenomena. For instance, it has been used for detecting stress [101], epileptic seizures [62], and students' emotional engagement in classrooms [61].

One of the main reasons for neglecting EDA in sleep studies is the complexity of the recorded signals. Long-term EDA recordings are susceptible to noise from various sources that cause artefacts in the signals, that is, sudden out-of-scale spikes; the most prominent sources of noise are body movements and poor skin-to-electrode connection. While in laboratory-controlled settings it is possible to log the patient's movements and to discard those signal segments when analysing data, in free-living conditions, it is more difficult to do so. Because removing artefacts is important, much of the research on EDA signals has focused on automating their detection. Various methods have been proposed, often using supervised or unsupervised machine learning (ML) algorithms [102, 77, 74]. EDA has been only scarcely and only recently used for sleep staging or to infer sleep quality [65, 66].

Abnormal sweating patterns may indicate the presence of various sleep disorders [18, 103]. In this work, we focused on sleep-breathing disorders, particularly obstructive sleep apnoea (OSA) [57]. OSA causes unexpected SNS activity, resulting in frequent nocturnal sweating [71]. Despite the relationships between EDA and OSA has been studied [68, 56], there is still a need for a quantitative model relating EDA and OSA.

In this paper, we applied supervised ML to EDA data to predict sleep stages and the presence of OSA. Currently, diagnosing it requires performing a full polysomnography (PSG) study in a laboratory setting, followed by manual scoring of the recordings. This procedure is time-consuming and can lead to atypical sleep patterns because of the differences between sleeping in a controlled environment, such as a sleep lab, and sleeping at home [104]. We present an ML-based approach that uses features extracted from the EDA signal, recorded in a home-setting, to automatically detect sleep stages and OSA.

4.2 Materials and Methods

We used a set of 60 full-night PSG recordings from participants in the Sleep Revolution Project [105]. We describe the cohort in detail in Table 4.1. The consent

of the National Bioethics Committee and the Data Protection Authority of Iceland was granted for this study (VSN-21-070). All participants received and signed an informed consent for study participation.

4.2.1 Instrumentation

PSGs studies were recorded using A1 devices from Nox Medical (Reykjavik, Iceland). As the traditional PSG setup does not include EDA recordings, we added a channel for the EDA signal. A1 devices measured EDA at a sampling frequency of 200 Hz. For the measurement of the EDA signal, we used the same technique as in [56].

4.2.2 Sleep Stage Labelling

Sleep experts manually scored the electroencephalogram (EEG) and determined the sleep stage: wake (W), rapid eye movement (REM) sleep, sleep stage 1 (N1), sleep stage 2 (N2), and sleep stage 3 (N3). The scoring procedure was performed according to the American Academy of Sleep Medicine guidelines [106], using the Noxturnal software (Nox Medical, Reykjavik, Iceland). In this work, for detection, we considered both the above mentioned five stages or only four stages, by merging the N1 and N2 stages and relabelling them as light sleep. Additionally, we relabelled the N3 stage as deep sleep. The stages that we considered are then W, light sleep, deep sleep, and REM sleep, as is often done in the literature [107]. We report the distribution of sleep stages in Table 4.2.

	Non-OSA	**Mild OSA**	**Moderate to severe OSA**
Number of participants (AHI)	19	24	17
Female participants (AHI)	47.4%	67.0%	29.4%
AHI	2.8 ± 1.3	10.0 ± 2.8	24.9 ± 10.5
BMI	25.8 ± 3.6	26.0 ± 3.6	25.8 ± 3.8
Age	36.2 ± 10.4	49.6 ± 14.7	52.0 ± 14.4
Percentage of epochs (AHI)	32.1%	39.0%	28.9%
Number of participants (ODI)	21	26	13
Female participants (ODI)	42.9%	61.5%	38.5%
ODI	1.5 ± 2.5	9.0 ± 2.5	24.1 ± 7.7
BMI	25.8 ± 3.8	27.7 ± 4.5	29.2 ± 2.8
Age	38.4 ± 12.4	48.2 ± 14.8	53.9 ± 14.0
Percentage of epochs (ODI)	33.9%	44.7%	21.4%

Table 4.1: Dataset content according to the apnoea-hypopnoea index (AHI) or the oxygen desaturation index (ODI).

Wake	N1	N2	N3	REM
12.2% ± 0.1	16.5% ± 0.1	32.5% ± 0.1	18.2% ± 0.1	20.6% ± 0.1

Wake	Light	Deep	REM
12.2% ± 0.1	49.0% ± 0.1	18.2% ± 0.1	20.6% ± 0.1

Table 4.2: Distribution of sleep stages for 4 and 5 stages architectures. We report mean values and standard deviations.

4.2.3 Obstructive Sleep Apnoea Labelling

Currently, OSA detection requires either manual scoring of a full PSG study or a home sleep apnoea testing, and the evaluation of two parameters: the apnoea-hypopnoea index (AHI) and the oxygen desaturation index (ODI) per hour of sleep, [106]. A shortcoming of the AHI is that it does not quantify one of the main consequences of OSA, which is oxygen desaturation. For this reason, sleep experts have defined the ODI value as the number of oxygen desaturation events $\geq$3% or $\geq$4% divided by the total sleep time [108, 106]. In this work, the sleep experts used 3% as threshold value.

We obtained a participant's OSA status from the manual scoring of PSG. We merged the moderate and severe OSA conditions to obtain three classes. To define them, we used the following modified version of the standard guidelines [109]:

- Non-OSA: AHI <5,
- Mild OSA: 5$\leq$ AHI <15,
- Moderate to severe OSA: AHI $\geq$15.

We also classified the samples based on the ODI and computed the correlation between the two indexes and the EDA signal. Note that the ranges used for the ODI-based classification are the same as the ones for the AHI classification [108]. Each epoch in an individual's data sample was labelled as either belonging to a non-OSA participant, one with mild OSA, or one with moderate to severe OSA. By epoch, we refer to a 30 seconds signal window. We adopted this time length to be consistent with the epochs' length used by sleep experts during manual scoring. Note that only seven samples were classified differently depending on whether we used the AHI or the ODI. Finally, we present the distribution of non-OSA, mild OSA, and moderate to severe OSA epochs in Table 4.1.

4.2.4 Signal Pre-Processing

From the Noxturnal software environment, we exported EDA signals using the edf file format and imported them in MATLAB® [93] for pre-processing and feature

extraction. We down-sampled the original signal from 200 Hz to 35 Hz to reduce the computational burden, following the guidelines presented in [94]. We then pre-processed the original signal to obtain different kinds of data required by our detection algorithm.

First, because individual sweating patterns lead to significantly different-looking EDA signals [14], we computed the second-order polynomial best approximating the raw signal and subtracted it from the raw signal. Second, we applied a seventh-order Savitzky-Golay filter [110] to the original signal to eliminate high-frequency contributions. We also applied a discrete wavelet transform (DWT) to the original signal. We computed the approximate and detailed discrete wavelet coefficients and soft thresholded the detail coefficients to remove possible recording noise [95]. We then subtracted the Savitzky-Golay filtered signal from the discrete wavelet filtered signal; we referred to it as diffEDA.

Third, we computed the first and second-order derivatives of previously described three signals using a differentiator finite impulse response (FIR) filter. We used this method rather than a finite-differences scheme to prevent noise propagation. Particularly, we used a 50th-order filter with a passband frequency of 10 Hz and a stop-band frequency of 12.5 Hz. We disregarded the transient to avoid including artificial oscillations caused by applying the filter by discarding $N = 50$ samples. Note that, we denoted time derivatives by placing ∂_t or ∂_t^2 before the signal of interest; for example, we referred to the second time derivative of the de-trended signal as ∂_t^2detEDA.

Fig. 4.1- 4.4 shows the complexity of the EDA signal. We show five-minutes time windows of continuous N3 and REM sleep in Fig. 4.1 and Fig. 4.2, respectively. We then highlight EDA events in Fig. 4.3. Finally, we show the EDA signal during an OSA occurrence in Fig. 4.4.

4.2.5 Feature Extraction and Selection

We defined a feature set in the time-domain, frequency-domain, as well as time-frequency domain (these are wavelet-related variables) in a process called feature engineering [111]. In addition to standard statistical features, we used number and energy content of EDA events and storms, as they are known to differ for different sleep stages [73] and OSA severity [56]. EDA events are oscillations of the skin voltage of defined amplitudes and frequencies. We are particularly interested in the following three types of oscillations: positive/negative monophasic, biphasic, and triphasic. EDA storms are time windows with high concentrations of events. The definition of storms has changed through time [112, 73], we used an equivalent definition to the one given by Sano and colleagues, that is, a timespan of at least one minute with a minimum of two EDA events. Particularly, we used the algorithm developed in [113] to detect EDA events and storms. Thereafter, we computed the normalised number of samples within either an EDA event or

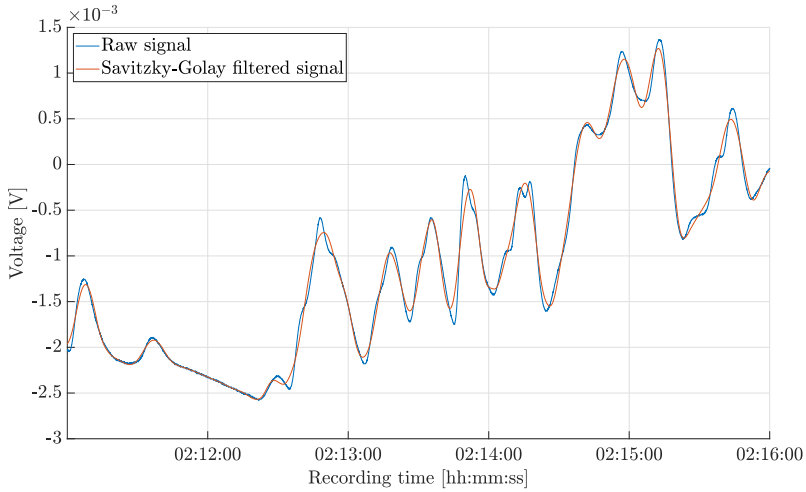

Figure 4.1: Comparison between the electrodermal activity (EDA) signal and the Sabitzky-Golay filtered signal for five minutes of raw and filtered signal during sleep stage 3 (N3).

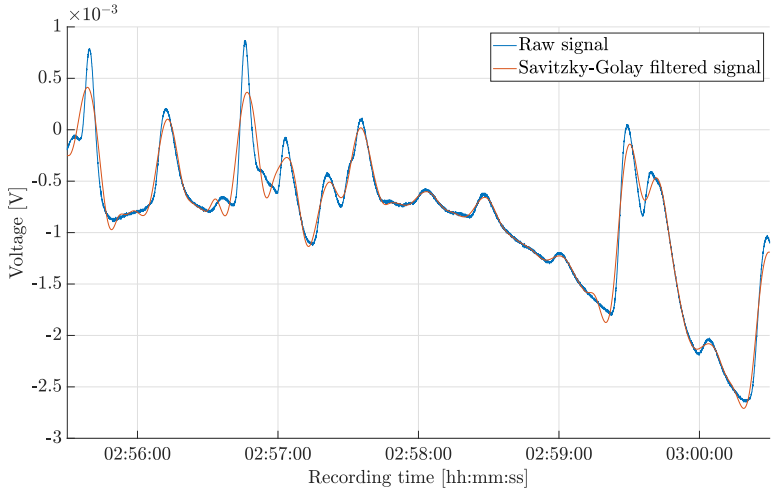

Figure 4.2: Comparison between the electrodermal activity (EDA) signal and the Sabitzky-Golay filtered signal for five minutes of raw and filtered signal during rapid eye movement sleep (REM).

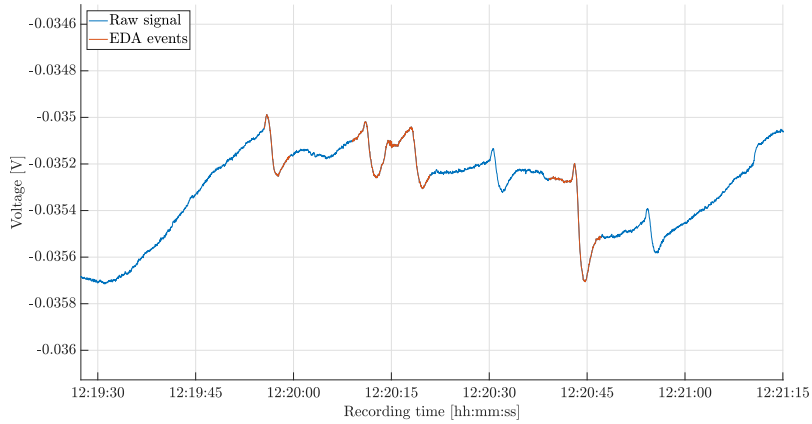

Figure 4.3: Comparison between the electrodermal activity (EDA) signal and the Sabitzky-Golay filtered signal for EDA events(raw signal).

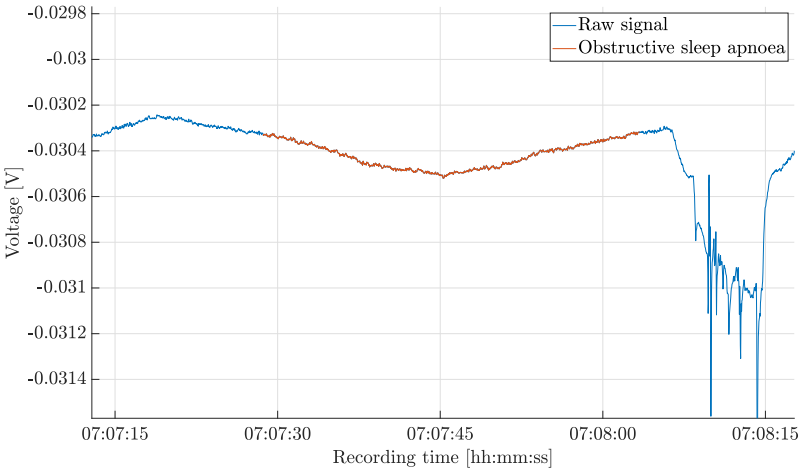

Figure 4.4: Comparison between the electrodermal activity (EDA) signal and the Sabitzky-Golay filtered signal for five minutes of raw and filtered signal during an obstructive sleep apnoea occurrence.

storm, together with their euclidean norms. Additionally, we added sex as a categorical feature to complete the set of variables and normalised the features across individuals. The full feature set is shown in Table 4.3.

Finally, after training and testing the model on the complete variable set, we investigated whether we could reduce the feature set dimension by analysing intra-variable correlation. We identified correlated features by computing the pairwise Pearson correlation coefficient r. We then reduced the dimension of the feature set by retaining only one of the correlated variables. We looked at the correlation matrix to identify the threshold value r_{th}.

Index	**Signal**	**Computed features**
1-18	EDA detEDA	Mode, median, maximum of absolute value, line length, 10^{th} quantile, 75^{th} quantile, singular value decomposition (SVD) entropy, nonlinear energy, Shannon entropy
19-34	∂_tEDA, ∂_t^2EDA ∂_tdetEDA, ∂_t^2detEDA	Mean value, variance, median value, numbers above zero
35-40	EDA detEDA	Maximum power spectral density (PSD) estimate, frequency of the maximum PSD estimate, Fisher's g [114]
41-64	EDA detail coefficients decomposition levels (DL) 1-4	Maximum, mean, standard deviation, median, Euclidian norm, normalised numbers above zero
65-70	EDA detEDA	Lyapunov exponent, maximum value of the upper envelope, minimum value of the lower envelope
71-72	diffEDA	Sum of cross-correlation, maximum convolution value
73-76	EDA	Normalised number of event samples, normalised event energy, normalised number of storm samples, normalised storm energy
77	Individual	Sex

Table 4.3: Set of variables extracted from the electrodermal activity (EDA) signal.

4.2.6 Training Procedure

Sleep stages are not equally distributed during the night, this asymmetry caused a significant imbalance in our dataset and affected model performance. To reduce the negative impact of this effect, we performed synthetic minority oversampling (SMOTE) [115], that is, we generated artificial samples for the minority classes to alleviate the bias towards the most dominant class. We then trained models using the extreme gradient boosting (XGBoost) algorithm [41], since a gradient boosting algorithm was recently used in a similar application with promising results [66].

We applied different validation methods. We either used leave-one-subject-out (LOSO) validation [37], where we alternately left out one sample and used the other 59 samples as training data, or we did as previously and in addition, we trained the model using randomly selected 25% of the epochs from the left-out subject's night (Personalised). We always used the same seed for reproducibility. After this random sampling, we applied the SMOTE algorithm to the training data. We evaluated the OSA model only by means of the LOSO scheme. We did so, because of the way that we labelled the data for OSA detection, see Section 4.2.3.

4.2.7 Evaluation Metrics

We computed different measures to evaluate the models' performances. All indices were obtained using scikit-learn [116]. F1 and recall scores were used to evaluate the sleep staging performances. While F1-score is a commonly used measure in ML applications, we used the recall score to account for the significant class imbalance [66]. Recall score is the ratio between true positives and the sum of true positives and false negatives and, thus, a measure for the number of relevant objects detected by the algorithm. The F1-score is the harmonic mean of precision and recall scores and is used in classification problems with imbalanced datasets, as the precision score on its own may be misleading. As we dealt with a multi-class classification problem, we used the macro version of both parameters; the macro F1-score is the average of all F1-scores, and the macro recall is the average of all recalls. For the remainder of the paper, we referred to the macro F1-score and macro recall value simply as F1-score and recall.

For the OSA model, we used the F1-score and accuracy values. Accuracy is the ratio between the number of correctly identified epochs and the total amount of epochs. In addition to these two measures, we evaluated the three-class algorithm's ability to distinguish between non-OSA participants and those with OSA. To do this, we considered all OSA epochs as equivalent, which made the classification problem a binary one; we then computed the accuracy score and referred to it as the adjusted accuracy score. We did not include the recall for OSA models' evaluations, as it deals with all misclassifications in the same way. Particularly,

misclassifications between severe and mild OSA conditions and between non-OSA and OSA conditions have different clinical meanings.

4.2.8 SHapley Additive exPlanations

To evaluate the contribution of each training variable, we used SHapley Additive exPlanations (SHAP) [117]. The technique was developed in game theory and only recently adapted to ML interpretability applications [118]. To find the SHAP value of the i-th variable, we computed the predictions for all possible feature combinations with and without the i-th variable. The SHAP value is then the average of the contributions of the i-th variable to each prediction [119].

4.3 Results and Discussion

4.3.1 Feature reduction

Before presenting the models' performances, we offer an analysis of the feature set reduction process; for the sake of notation, we refer to variables by index, as in Table 4.3. We identified three main clusters of correlated variables by looking at the graphical representation of the correlation matrix, Fig. 4.5. The first one involves features 1-15, which are statistical measures, in the time domain, of EDA and detEDA signals. The second one is a large cluster encompassing features 41-64, variables obtained in the time-frequency domain. Finally, nonlinear features 65-70 also show meaningful correlation patterns.

After setting $r_{th} = 0.8$, we reduced the number of correlated variables. We decided which feature to eliminate as follows: first, we computed the correlation coefficients between the i-th feature and the remaining ones, then we eliminated the j-th feature, if $r_{i,j} > r_{th}$, where $r_{i,j}$ is the Pearson correlation coefficient between the i-th and the j-th variables and $j > 1$. We started at $i = 1$. In this way, we obtained a reduced set of 40 features, which we present in Table 4.4. We opted not to decrease further the r_{th} value, as the resulting feature set did not present any significant clusters, see Fig. 4.6. Also, lower values of r_{th} may result in worse classification performances.

4.3.2 Interpretation of Sleep Staging

We summarised the models' performances in Table 4.5, where the F1-scores and recall values are reported. Our results suggest a need for personalised models [10]. A possible explanation for the relatively poor performance is that different brain regions can be in different sleep stages at the same time. For instance, sweat glands' activation signals and, thus, EDA, are generated in the hypothalamus [120], while the EEG, used to manually label sleep stages, measures neocortex activity,

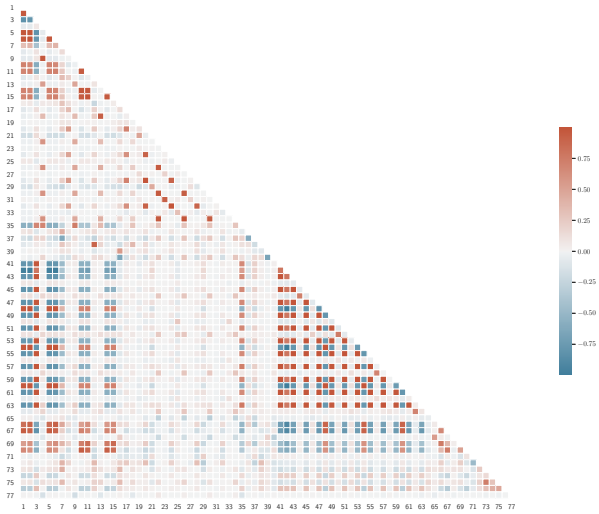

Figure 4.5: Representation of the lower triangular feature correlation matrix. We denoted the variables by index, as in Table. 4.3.

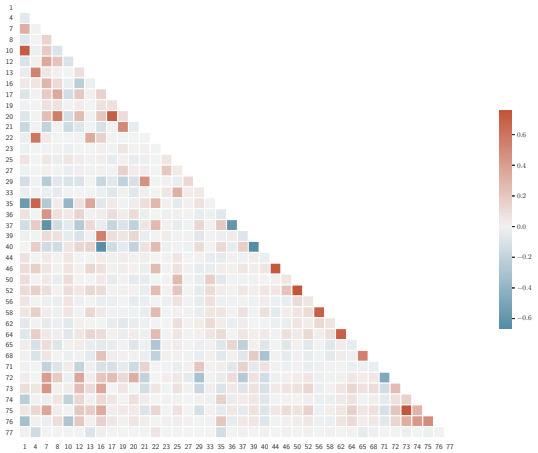

Figure 4.6: Correlation matrix for the reduced feature set. Variables are denoted by index, as in Table 4.3.

and it is known that the two brain areas can be in different sleep stages [99]. How-

Signal	**Computed features**
EDA	Mode, maximum of absolute value, line length, singular value decomposition (SVD) entropy, nonlinear energy, Lyapunov exponent, maximum power spectral density (PSD) estimate, frequency of the maximum PSD estimate, Fisher's g [114]
detEDA	Mode, maximum of absolute value, line length, singular value decomposition (SVD) entropy, nonlinear energy, Lyapunov exponent, requency of the maximum PSD estimate, Fisher's g [114]
∂_tEDA	Mean, variance, median, number above zero
∂_t^2EDA	Mean, median
∂_tdetEDA	Mean, median
∂_t^2detEDA	Median
EDA detail coefficients decomposition levels (DL) 1-4	Median, normalised numbers above zero
diffEDA	Sum of cross-correlation, maximum convolution value
EDA	Normalised number of event samples, normalised event energy, normalised number of storm samples, normalised storm energy
Individual	Sex

Table 4.4: Optimised feature set for the sleep staging models, $r_{th} = 0.8$.

ever, personalising the LOSO-based model with a small number of epochs from the left-out sample dramatically improves the algorithm, see also Fig. 4.7- 4.8 and Fig. 4.9- 4.10, which show confusion matrices normalised such that the sum of each row equals one.

By looking at the confusion matrix in Fig. 4.8, we concluded that the personalised model cannot characterise the N1 sleep stage using only EDA. Furthermore, N1 detection appeared to be a cumbersome task even when other ML methods and other signals were used, such as EEGs, electrooculograms (EOGs), and electromyograms (EMGs) [121, 122]. A similar disagreement in determining the sleep stage was also found when comparing different manual scorings [123]. However, the detection of slow wave sleep (SWS) phases, that is, deep sleep and N3 stage, and REM sleep phases worked well for both models. This was expected, since these are the phases with the most distinct EDA patterns. Notably, by looking at Fig. 4.8, we can conclude that, based on EDA, the N3 stage is more similar to the N2 stage than any other sleep stage.

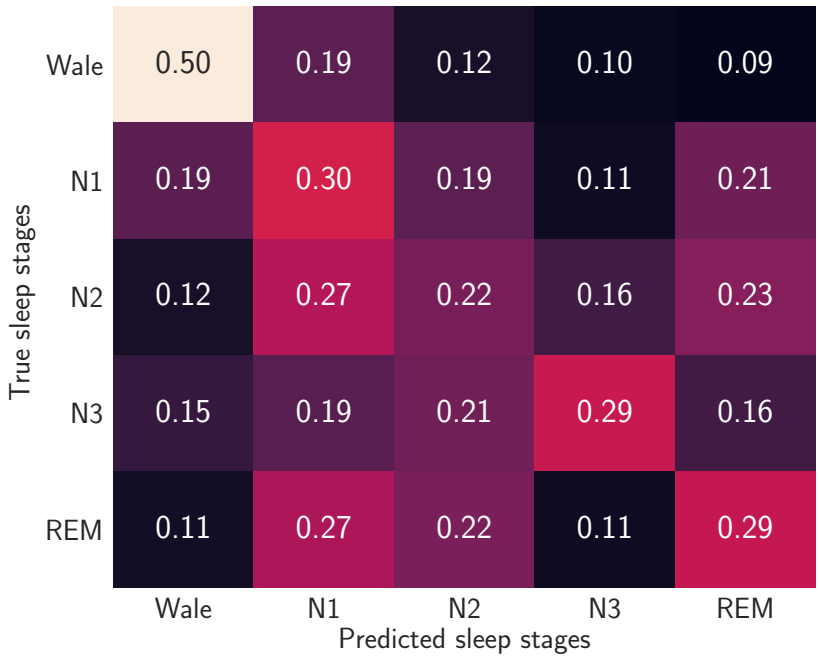

Figure 4.7: Normalised confusion matrices when we consider five sleep stages and use the reduced feature set. and leave-one-subject-out (LOSO). We trained the algorithm without including data from the left out participant.

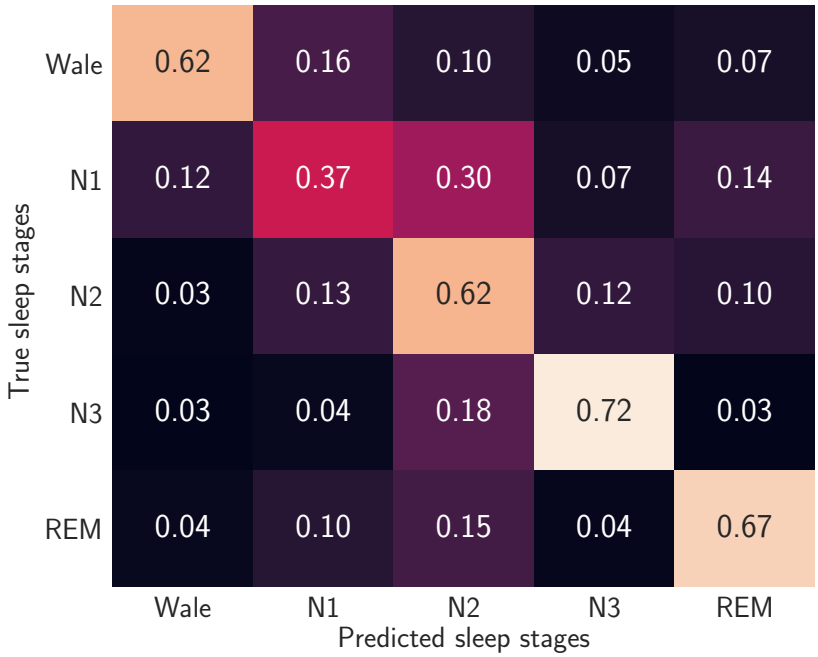

Figure 4.8: Normalised confusion matrices when we consider five sleep stages and use the reduced feature set. We trained the algorithm without including data from the left out participant. In addition to the 59 participants training set, we used randomly picked 25% epochs of the test participants.

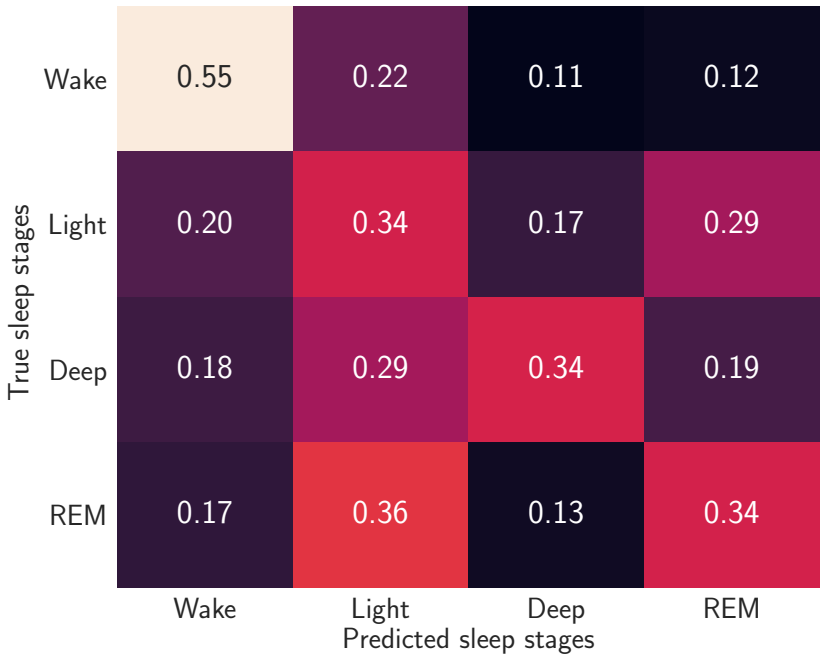

Figure 4.9: Normalised confusion matrices when we consider four sleep stages and use the reduced feature set. and leave-one-subject-out (LOSO). We trained the algorithm without including data from the left out participant.

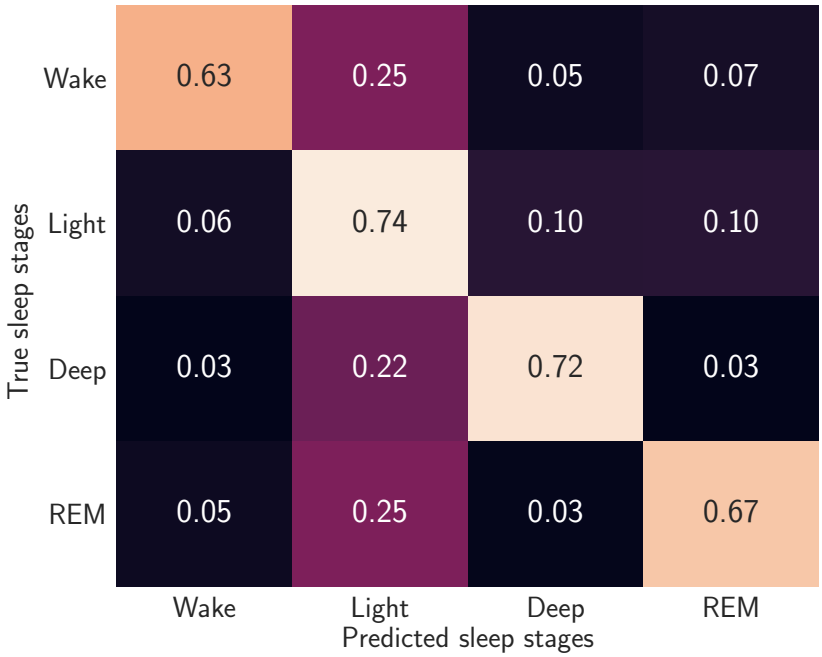

Figure 4.10: Normalised confusion matrices when we consider four sleep stages and use the reduced feature set. We trained the algorithm without including data from the left out participant. In addition to the 59 participants training set, we used randomly picked 25% epochs of the test participants.

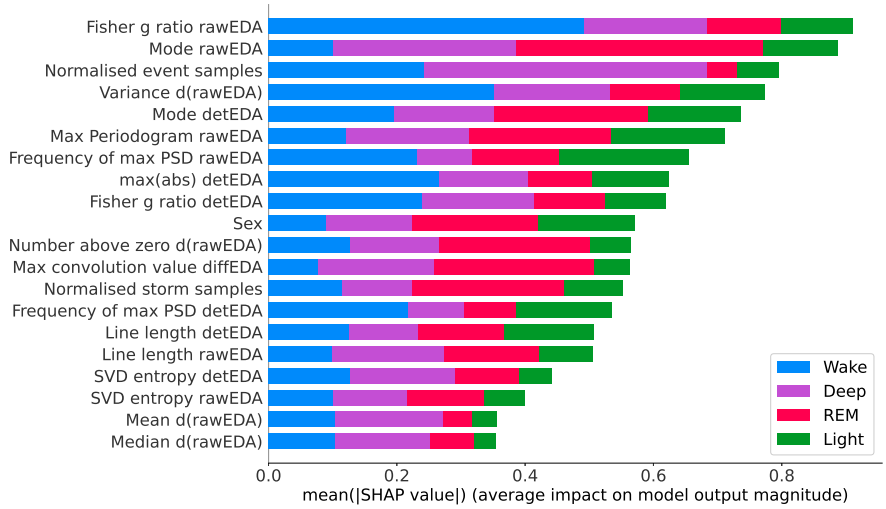

Figure 4.11: SHapley Additive exPlanations (SHAP) values of the sleep staging model trained using the leave-one-subject-out (LOSO) scheme and the reduced feature set.
for the four sleep stages architecture: wake (W), light sleep, deep sleep, rapid eye movement (REM) sleep.

Finally, we offer a graphical interpretation of the sleep staging model, trained on the reduced dataset, through the SHAP values of the 20 most influential variables, see Fig. 4.11- 4.12. It is worth noting that both models considered the number of EDA events to be highly relevant for N3 stage, see Fig.4.11- 4.12. The models also predict a significant relationship between EDA storms and REM sleep. Indeed, it is known that EDA activity increases in the third cycle of REM sleep [14].

# stages	$\mathbf{r_{th}}$	**Leave-One-Subject-Out**		**Personalised**	
		Macro F1-score	**Macro recall score**	**Macro F1-score**	**Macro recall score**
5 stages	0.8	27.3%	32.4%	57.5%	58.0%
4 stages	0.8	32.8%	39.7%	66.6%	66.9%

Table 4.5: Summary of sleep staging performance for, both, 4 stages and 5 stages classification.

4.3.3 The Need for Personalisation in Sleep Staging

Several physiological considerations support the need for personalisation in EDA-based sleep staging. Nocturnal sweat, the principal cause of changes in skin elec-

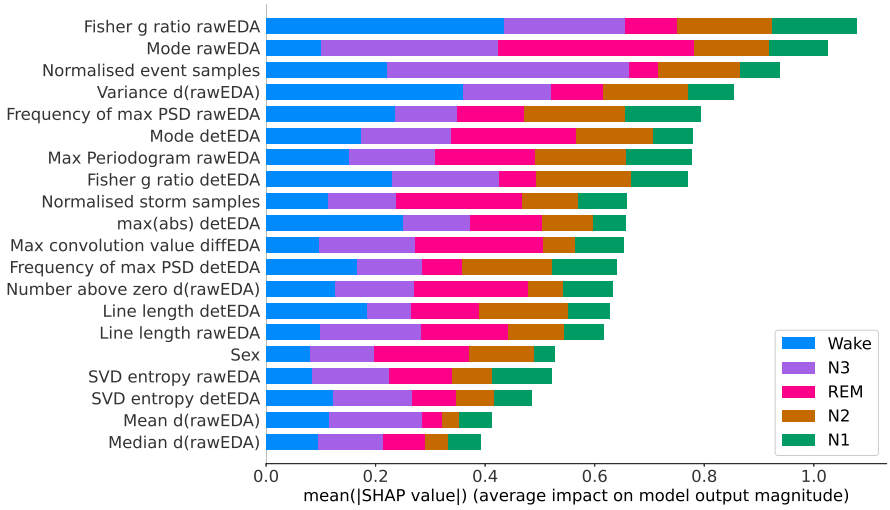

Figure 4.12: SHapley Additive exPlanations (SHAP) values of the sleep staging model trained using the leave-one-subject-out (LOSO) scheme and the reduced feature set. for the five sleep stages architecture: wake (W), non rapid eye movement 1 (N1), non rapid eye movement 2 (N2), non rapid eye movement 3 (N3), rapid eye movement (REM) sleep.

trical properties, is secreted to lower the core body temperature (CBT) [100]. However, the thermoregulation process depends on a large number of factors, for example, age, BMI, sex, skin hydration, eccrine sweat gland concentration, and environmental conditions [124, 125, 126]. All the factors mentioned significantly impact sweat and, consequently, the EDA signal. Furthermore, the latter is also affected by subject-dependent brain dynamics.

It is not straightforward to decide which personal subset of epochs to choose, as different EDA patterns arise in different parts of the night; for example, EDA events are more frequent in REM sleep during the last sleep cycle [14], while rarer in other REM sleep periods. Furthermore, differences in sleep cycle duration caused by age and OSA condition, among other factors, may hinder the beneficial effect of the algorithm's personalisation. Because of this, we opted for a fixed-seed random-pick approach.

4.3.4 Interpretation of the OSA Model

To evaluate the models' ability to distinguish between non-OSA persons and those with either mild or moderate to severe OSA, we used average values of the accuracy score, the F1-score, and the adjusted accuracy score. We also evaluated a binary classification problem, where participants either had OSA or not, for which we refrained from calculating the adjusted accuracy score. We present the results as we did for the sleep staging models in Table 4.6. They show that OSA severity determined through the EDA signal rather follows the classification obtained by using the ODI rather than the AHI. A possible explanation for this behaviour is how the ODI value divides the participants. Looking at Table 4.1, we observed that while both the indexes found the mean age to increase with the OSA severity, in ODI classification BMI values also increased with OSA severity. Lower BMI values have been associated with lower mean temperature values, [127], which may result in less need for thermoregulation. Consequently, simpler sweating patterns may be observed, which are better learned by the algorithm.

In Fig. 4.13- 4.14 and Fig. 4.15- 4.16, we used the SHAP values to present the effect of each variables on the different classification problem. Both three-class models choose normalised storm samples as one of the most significant variables, which relates well to the literature [56].

4.3.5 Feature Selections Comparison

Out of the 77 extracted variables, only eight appear in all models' top 20 most important features. They are EDA mode, ∂_tEDA variance, detEDA mode, EDA maximum power spectral density (PSD) estimate, EDA frequency of the maximum PSD estimate, ∂_tEDA normalised numbers above zero, detEDA frequency of the maximum PSD estimate, and biological sex. The seven numerical variables are

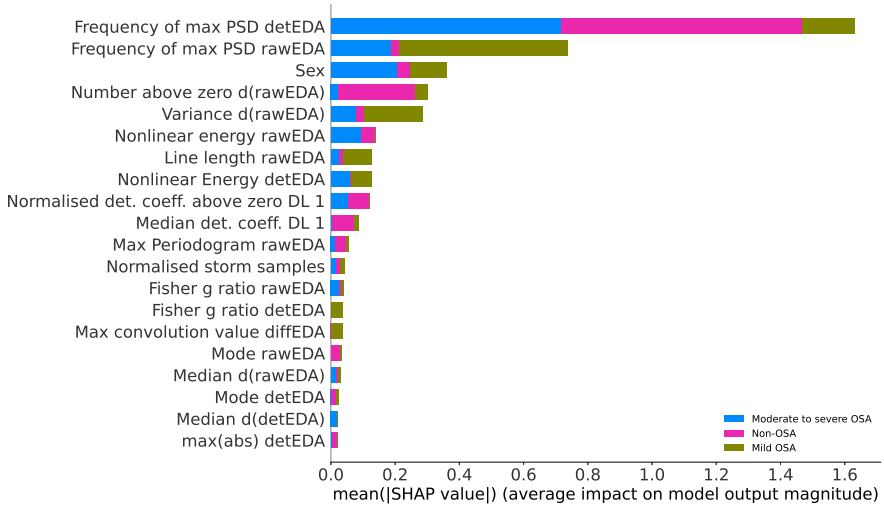

Figure 4.13: SHapley Additive exPlanations (SHAP) values of the obstructive sleep apnoea (OSA) detection model based on apnoea-hypopnea index (AHI) values and the reduced feature set. Three-class classification problem: participants with no, mild, or moderate to severe OSA.

OSA structure	$\mathbf{r_{th}}$	Mean accuracy score	Macro F1-score	Adj. accuracy score
AHI - non-OSA vs- OSA	0.8	75.7%	65.6%	-
ODI - non-OSA vs. OSA	0.8	82.0%	67.7%	-
AHI - Three groups	0.8	54.8%	32.9%	78.4%
ODI - Three groups	0.8	54.8%	32.9%	83.7%

Table 4.6: Results for obstructive sleep apnoea (OSA) detection, based on the apnoea-hypopnoea index (AHI) or on the oxygen desaturation index (ODI).

computed from two signals, that is, raw and de-trended EDA and the derivative of the raw signal; this subset is composed of variables spanning multiple domains, particularly time, frequency and EDA-specific. This variety confirms the need to consider different dynamical behaviours and EDA-related phenomena when using this signal. The most common specific feature is the number of EDA storm samples, which is amongst the top 20 most important features for all models, except for the two-class ODI-based OSA classification problem. However, in the latter problem, normalised storm energy is considered a relevant feature. Works trying to relate EDA and OSA are scarce and based mainly on subjective night sweats reports [128]. Although it is well-established that OSA symptomatology includes abnormal sweating episodes [56, 71], there needs to be more understanding of the

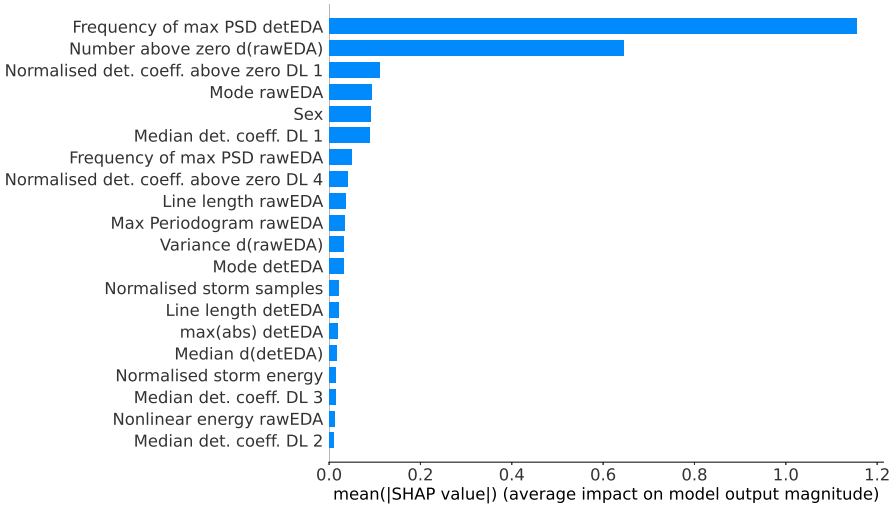

Figure 4.14: SHapley Additive exPlanations (SHAP) values of the obstructive sleep apnoea (OSA) detection model based on apnoea-hypopnea index (AHI) values and the reduced feature set. Binary classification problem: non-OSA participants and those with OSA.

relationship between OSA and EDA events and storms. Our work concludes that evaluating EDA storms, their lengths or energies, is more decisive in detecting OSA, particularly severe expressions, than evaluating EDA events. This conclusion holds for OSA classifications based on both AHI and ODI severity.

4.4 Conclusion and Future Work

The presented work aimed at detecting sleep stages and OSA severity using only the EDA signal. Recently, Anusha and colleagues presented an ML algorithm for identifying the sleep stage of the hypothalamus, the brain region directly responsible for thermoregulation during sleep [65], while, Gashi and colleagues presented a similar algorithm based on EDA that is able to detect wake/sleep stages and high-/low sleep quality [66]. Latter algorithms are based on self-reported annotations. Despite these significant results, more research on the relationship between EDA and neocortex activity is needed. Our work is the first one, in which neocortex sleep stages are predicted solely based on EDA. In the first part of this research work, we presented a sleep staging algorithm that is particularly accurate in detecting those sleep stages, where specific EDA patterns are known to occur, which are N3 and REM sleep. In the second part, we focused on OSA detection. By us-

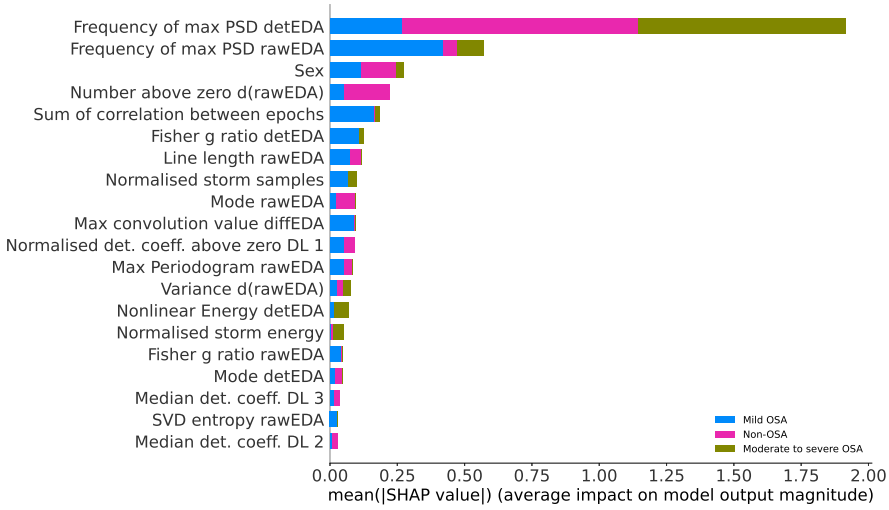

Figure 4.15: SHapley Additive exPlanations (SHAP) values of the obstructive sleep apnoea (OSA) detection model based on oxygen desaturation index (ODI) values and the reduced feature set. Three-class classification problem: participants with no, mild, or moderate to severe OSA.

ing the EDA signal, we distinguished non-OSA participants from those with OSA with reasonable accuracy.

Our work has three main limitations. The first one is that the raw signal was recorded at 200 Hz, an unattainable sampling frequency for current wearables. However, the signal was significantly downsampled, to 35 Hz, before it was handled. Since EDA events occur in the frequency band [0.25 Hz − 3 Hz] for endosomatic recordings, like the ones used in this study, further downsampling might potentially be performed without a significant loss of information, which we leave for future work. The second limitation is that the sleep staging algorithm requires a certain amount of individual data manually scored by a sleep expert. While this prevents the sleep staging model from being user-independent and, thus, might limit its use in wearables, in clinical studies, requiring only a small part of the signal to be manually scored significantly saves time and cost. Moreover, our work adds to the body of evidence on how crucial it is to include knowledge about sleep processes in ML models. A final limitation is the participants' significant ranges in age and BMI within a relatively small sample size. While the participants' diversity ensured to obtain general models, it also prevented the algorithm from learning patterns specific to a particular group, for example, individuals of the same biological sex and of similar age. Future studies may overcome this last limitation by

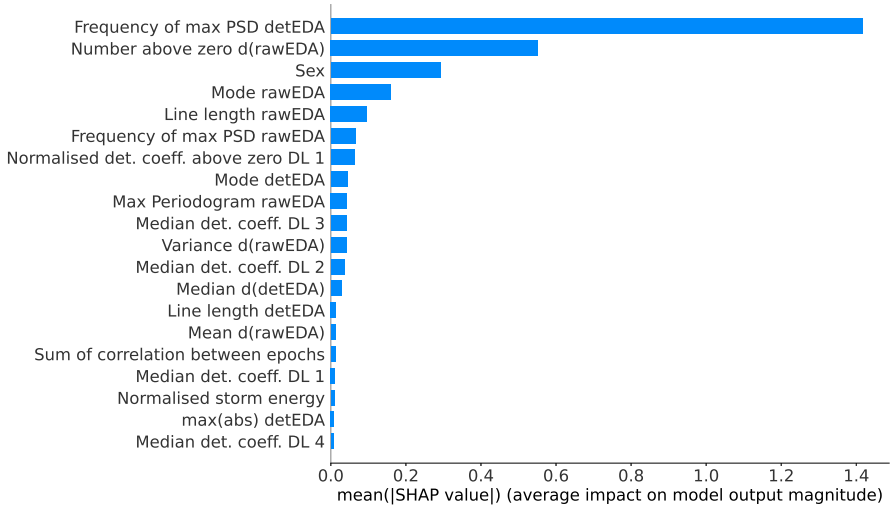

Figure 4.16: SHapley Additive exPlanations (SHAP) values of the obstructive sleep apnoea (OSA) detection model based on oxygen desaturation index (ODI) values and the reduced feature set. Binary classification problem: non-OSA participants and those with OSA

using a more selected cohort or by considering the body temperature signal, therefore addressing the differences in mean body temperature due to various aspects such as age, sex, and BMI.

To improve on the reported results, in the future, we will also include additional signals obtainable through wearables, such as acceleration and skin temperature. Doing so might reduce the need for individual tuning of the algorithm and allow it to identify other sleep stages more accurately. More precise sleep staging based on data obtained from wearables will allow the estimation of more advanced sleep parameters used in sleep diagnostics, such as total sleep time and sleep efficiency. Finally, since the algorithm labels each epoch as “non-OSA” or “OSA-prone", it will be possible to track a potential onset or worsening of sleep-disordered breathing. By adequately characterising the development of OSA symptoms, it will be possible to define a threshold that will lead to suggesting to seek professional advice when exceeded.

Chapter 5

An Optimisation-Based Sleep Thermoregulation Model

This chapter is to be submitted to "Mathematical Biosciences" as: "Piccini, J., August, E., An Optimisation-Based Sleep Thermoregulation Model"

Abstract

Human thermoregulation during sleep is a delicate balance between the need to keep the brain temperature within a tight temperature range and the constraints on the available energy. This problem has, so far, been studied by trying to solely replicate the temperature behaviour, rather than for investigating the underlying optimisation problem. In this paper, we model homeostasis as a nonlinear optimal control problem that minimises a physiologically-inspired cost function. We find an optimal control action sequence by by solving a nonlinear optimisation problem and then use this novel framework to investigate the interaction between skin and brain temperatures, as well as the effect of different physical conditions on the capability of the human body to thermoregulate itself. Our approach successfully tracks the in-sleep theoretical brain temperature for a variety of environmental conditions, while minimising energy allocation.

5.1 Introduction

Sleep represents a particularly interesting test bed for investigating the human body regulatory systems since external stimuli, that might act as disturbances, are at a minimum. For example, during wakefulness, in addition to maintaining key temperature signals in appropriate ranges, thermoregulatory responses are also generated by emotional stimuli [129]. Because of this interplay, studying thermoregulation during sleep allows to investigate its most fundamental mechanisms. In most mammals, the temperature of organs and the brain, commonly referred to as core body temperature (CBT), is kept at a constant value, also called homeostasis, to avoid deviations that could lead to organ malfunctioning. Significantly, the CBT safe range is exceptionally narrow; as a matter of fact, deviations as small as 3°C can lead to organ failure.

In the first part of the night, a decrease in CBT is observed, which is then followed by an increase before awakening and caused by the circadian rhythm [130]. The circadian oscillation causes the CBT to reach a maximum before sleep and a minimum approximately two hours before awakening. Sleep is a complex process and understanding its role still represents a prominent research question. Human thermoregulation is often regarded as one of the most significant nocturnal regulation processes [131]. Because of its importance, considerable research efforts have been dedicated to characterising key aspects, such as its functional architecture, both from qualitative and quantitative standpoints.

From a qualitative point of view, researchers have tried to understand the control structure of thermoregulation, particularly focusing on the different roles of skin temperature and CBT and how the sympathetic nervous system (SNS) manages variations in environmental conditions [26, 27, 132].

Quantitative results are obtained by using mathematical models with either a large number of nodes, that is, $N > 100$ [133], or consisting of simple compartmental models, that is, $N < 4$. Larger models discretise the human body in segments, for example, head, neck, and right-leg thigh, and further split such segments into different layers, such as core, muscle, and fat. Similar models are often used in works aiming at minimising energy expenditures in buildings [134]; we refer the reader to [135] for an extensive review of different models and their applications. However, research on simpler models also resulted in accurate descriptions [136, 137] based on modifications of the seminal Gagge's model [138]. While low-dimensional models for thermoregulation during wakefulness are abundant, there is a lack of such models during sleep, the most notable exception being [137]. There are several reasons for this gap in the literature. There are, for instance, different thermoregulatory actions for different sleep stages, a lack of a complete and thorough understanding of sleep, and the uncertainty on the thermoregulation control structure. The latter issue, in particular, has been a subject of an intense debate as there is no clear consensus on whether the control mechanism contains

only feedback loops or if feed-forward loops are also present [139, 140, 27, 132]; the existence of feed-forward loops has been introduced to account for the regulatory system's robustness to fluctuations in environmental conditions, which is distinctive to other feed-forward temperature control systems [141].

In both types of models, control action signals are generated by estimating deviations of temperature signals from their references through empirical equations [142]. The magnitude of the responses is proportional to the deviations of controlled variables, that is, different temperature signals and their reference values [133, 143]. A more complex approach is adopted in [144, 145], where the authors consider neuron firing dynamics. Despite the numerous efforts, past works do not explicitly consider the different energy expenditures needed by the various thermoregulatory actions, nor the optimisation processes occurring during sleep [55, 23]. For example, while generally being more effective for cooling, sweating not only requires more energy compared to vasodilation but also consumes water, a limited resource during sleep. These qualitative considerations suggest that the SNS finds an optimal trade-off between circadian rhythm-tracking properties and energy expenditure.

In this work, we investigate sleep thermoregulation in a novel manner, that is, we explicitly model the regulation process as an optimisation problem, building on observations made on sleep energy allocation [23]. After deriving two ordinary differential equations (ODEs) describing the heat exchanges occurring in the human body, we model thermoregulatory responses as depending on SNS-generated control actions rather than using empirical expressions. The control sequences are generated by minimising a cost function, which describes the physiological balance between the need for quick and precise tracking of the regulated variables and the need to use a minimum amount of energy. We do so by combining the mathematical model with well-known control theory results. In this work, the SNS acts as an optimal nonlinear controller, which we synthesise by solving a nonlinear program (NLP) through CasADi [50].

The importance of this work is multiple. First, we provide a framework for investigating different cost functions being minimised during sleep. Being able to change the quantity being minimised is an important contribution of this work; as in [146], biological systems might switch behaviours to optimise survival probabilities. Our model allows to investigate such a possibility. The second contribution of this paper lies in the flexibility of the presented framework; by appropriately tuning the model's parameters, we can simulate individuals with different physical characteristics, as well as a range of different operating conditions, both in terms of air temperature and relative humidity.

The remainder of this paper is organised as follows. Section 5.2 defines the dynamical system model by splitting it into passive and active components. In Section 5.3, we define the optimisation problem and explain our design choices. Section 5.4 shows the resulting signals for various environmental conditions; we

comment on them in Section 5.5. Finally, we conclude this paper in Section 5.6.

5.2 A simplified thermoregulation model

We first present the open-loop thermoregulation system; then, we introduce the novel model describing the different physiological control actions.

5.2.1 The Passive System

Our model is based on the following thermodynamic considerations [138]. The human CBT regulation involves a delicate balance between the increase caused by metabolic heat generation M and the dissipation of heat from the inner core to the skin and from the skin to the environment (see Fig. 5.1). The core compartment contrasts potentially dangerous increases in CBT by conducting heat through body tissues and the blood stream to the skin layer. The only other mechanism through which the core can dissipate heat is breathing, which directly connects the core compartment with the environment. Through these considerations, we obtain the following heat flux balances:

$$e_{skin} = q_{cd} - q_{cr} - q_{ev}$$
$$e_{core} = M - q_{cd} - q_{br}.$$

In the latter, we denote the heat storage rate of the core layer and of the skin layer as e_{core} and e_{skin}, respectively. We assume positive the heat fluxes increasing a layer's energy, and denote the internal heat metabolic production by M, the heat conducted through tissues and blood by q_{cd}, the heat exchanged with the environment through convection and radiation by q_{cr}, and through respiration by q_{br}. Finally, the heat dissipated from the skin compartment through sweat evaporation is denoted by q_{ev}. Each layer's heat storage rate is related to the layer's temperature through the following equation:

$$e_i = m_i c_{b,i} \frac{\mathrm{d}T_i}{\mathrm{d}t},$$

where the subscript i denotes quantities of the i-th layer, m_i is the compartment's mass, $c_{b,i}$ is the specific heat of the layer, and T_i is the layer's temperature. Throughout this work, we assume the skin layer and the clothing layer to be one and the same; the only effect of clothing is to increase the skin layer area by a factor f_{cl} depending on clothing insulation factor I_{cl} [147]. Throughout this work, we use Celsius degrees to measure temperatures as they are more easily interpretable and relatable to physiological conditions; we only use degrees Kelvin in the radiation equation, where we use the subscript K to denote their use. In our mathematical model we use the state-space notation; that is, we denote skin temperature and

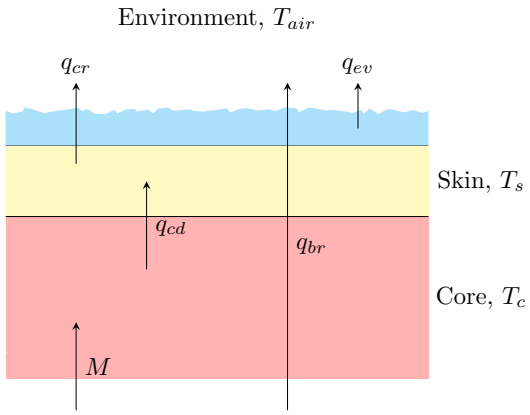

Figure 5.1: Graphical depiction of our model. The blue layer with an upper ragged border represents the sweat layer whose strength depends on CBT. Metabolic heat production M increases core compartment temperature, red layer. The core dissipates heat through convection and breathing, q_{cd} and q_{br}, respectively. Finally, the skin compartment, yellow layer, exchanges heat with the environment by convection and radiation, which we collect in q_{cr}, and through sweat evaporation, q_{ev}.

CBT as x_1, and x_2, respectively. By using fundamental thermodynamics considerations, we obtain the following mathematical model:

$$\dot{x}_1 = \frac{A_d}{m_{skin}c_b}\left(q_{cd}(x) - f_{cl}q_{cr}(x) - q_{ev}(x)\right) \tag{5.1}$$

$$\dot{x}_2 = \frac{A_d}{m_{core}c_b}\left(M_0 - q_{cd}(x) - q_{br}(x)\right) \tag{5.2}$$

$$q_{cd}(x) = (k_b + \dot{m}_{bl}c_{bl})(x_2 - x_1) \tag{5.3}$$

$$q_{cr}(x) = h_c(x_1 - T_{air}) + \sigma\alpha\epsilon\left(x_{1,K}^4 - T_{air,K}^4\right) \tag{5.4}$$

$$q_{br}(x) = 10^{-4}M_0\left(14(x_2 - T_{air}) + 23(p(x_1) - p_{va})\right) \tag{5.5}$$

$$q_{ev}(x) = 0.06h_e(p(x_1) - p_{va})) \tag{5.6}$$

$$p(T_i) = e^{18.67 - \frac{4030.18}{T_i - 38.15}} \tag{5.7}$$

$$p_{va} = RH \cdot p(T_{air}). \tag{5.8}$$

The system of ordinary differential equations (ODEs) given by (5.1)-(5.8) describes the dynamics of our model. A_d represents the human body surface computed using the DuBois' formula [148]:

$$A_d = 0.203m^{0.425}h^{0.725},$$

where m and h are the mass and height of the human body, respectively. We represent the core and skin masses as m_{core} and m_{skin}, respectively, the specific heats of the body and blood as c_b and c_{bl}, and the blood volumetric flow as $\dot{m}_{bl}$. We denote the metabolic heat produced during sleep by M_0, which we consider to be 85% of the wakefulness value M [149], the body tissues conductance by k_b, and the air convective heat coefficient by h_c. We denote the radiation parameters as σ, α, ϵ, which represent the Boltzmann's constant, the effective radiative area ratio, and the emissivity of the clothed body, respectively. Finally, RH is the air relative humidity, and h_e is the evaporative heat coefficient:

$$h_e = \frac{L \cdot h_c}{1 + 0.92 \cdot I_{cl} \cdot h_c},$$

where L is the Lewis' ratio. The definition of each parameter and their values are shown in Table 5.1.

Parameter	Value	Unit	Source
Metabolic production, M_0	80	W m^{-2}	[147]
Sleep metabolic production, M	68	W m^{-2}	[149, 147]
Height, ℓ	1.80	m	[−]
Mass, m	75	kg	[−]
Clothing insulation, I_{cl}	0.155	K m^2 W^{-1}	[147]
Clothing area factor, f_{cl}	1.150	[-]	[147]
Specific heat of human body, c_b	3492	J (kg K)$^{-1}$	[147]
Blood thermal capacity, c_{bl}	1.163	W hr (l K)$^{-1}$	[147]
Body tissues conductance, k_b	5.28	W m^{-2}	[147]
Neutral skin blood flow, $\dot{m}_{bl}$	6.3	l (hr m^2)$^{-1}$	[147]
Convective heat coefficient, h_c	5.2485	W m^{-2} K^{-1}	[150]
Effective radiative area ratio, α	0.72	[−]	[147]
Emissivity of clothed body, ϵ	0.97	[−]	[147]
Lewis' relation, L	2.2	[−]	[147]
Relative humidity, RH	30%	[−]	[−]

Table 5.1: Full set of parameters used in this work.

5.2.1.1 Evaporation Function Approximation

Previous works study sleep thermoregulation considering ambient temperatures of 20°C − 37°C. Assuming that outside the range of 10°C $\leq T_{air} \leq$ 40°C, sleep is rather difficult, we can substitute (5.7) by a second-order polynomial without loosing much accuracy while reducing. Particularly, for 10°C $\leq T_{air} \leq$ 40°C, we

$p(T_i)$ in (5.7) by the following polynomial:

$$p_2(T_i) = 0.0377T_i^2 - 0.3946T_i + 10.0619.$$

5.2.1.2 Equilbrium Point Analysis

We now study the open-loop dynamical system by looking at its equilibrium points and characterising their stability. We are only interested in steady states that arises from initial conditions by constraining initial conditions that lie within the following life-compatible set:

$$X_0 = \{31°\text{C} \leq x_1(t_0) \leq 35°\text{C},\ 36°\text{C} \leq x_2(t_0) \leq 38°\text{C}\}.$$

By using the *fsolve.m* function in MATLAB for all initial points from X_0, that is for all initial points $x_1(t_0)$ and $x_2(t_0)$, where $x_1(t_0) \in \{31.0, 31.1, 31.2, ..., 35.0\}$ and $x_2(t_0) \in \{36.0, 36.1, 36.2, ..., 38.0\}$, we find out that the system (5.1)-(5.8) has seemingly only one equilibrium point in X_0. By computing the Jacobian matrix,

$$J(x) = \frac{\partial f(x)}{\partial x},$$

and evaluating it at the equilibrium point we find that for the entire set X_0, the Jacobian matrix has a positive determinant and a negative trace; therefore, the equilibrium point is locally asymptotically stable.

5.2.2 The Control System

We now introduce active components governed by the SNS. Previous works consider proportional-like control laws obtained through data fitting such that thermoregulation responses had the following structure:

$$u_j(k+1) = K_j f_j(x(k) - x^{ref}(k)). \tag{5.9}$$

In (5.9), $f(x(k) - x^{ref}(k))$ denotes a function that depends on the deviation between the state variable and its reference trajectory at time step k, while K_j is a constant. Both terms are obtained through data fitting. However, these control laws have major shortcomings. First, typical saturations of physiological responses are not accounted for, functions of the type $f_j(x - x^{ref})$ increase with the deviation and upper bounds are not provided. Second, these expressions are obtained by fitting difficult to obtain and noisy signals [142]; for example, estimation of skin blood flow is a non-trivial task and experiments obtain measures that only hold locally. Furthermore, the empirical proportional control laws used to thermoregulation responses does not change with air temperature. This assumption might not hold in harsh conditions [142], when CBT regulation is prioritised at

the expense of the skin temperature or by ignoring the energy cost. We overcome these issue by providing new descriptions for the control actions and then computing the control sequence through numerical optimal control. To the best of our knowledge, this is the first work where ideas from optimal control theory are applied to thermoregulation. The active control system mechanisms maintaining CBT in its correct operating window vary with ambient temperature; they are divided into primary and secondary regulatory mechanisms. The primary regulatory actions are vasodilation and vasoconstriction, used to dissipate and withhold heat, respectively. This mechanism causes an increase or decrease in blood flow rate, by modifying the heat exchanged between the blood stream, core, and skin. We model this mechanisms by substituting (5.3) through the following expression:

$$q_{cd} = (k_b + \dot{m}_{bl} c_{bl} (1 + u_1))(x_2 - x_1). \tag{5.10}$$

Control variable u_1 represents the change in vasomotor tone; therefore, $u_1 > 0$ causes vasodilation, while $u_1 < 0$ leads to vasoconstriction. Changes in vasomotor tone directly affect m_{core} and m_{skin} as variations in blood stream also cause a mass exchange between the core layer and the skin layer. In the literature, the skin layer fraction α_{skin}, depends on $\dot{m}_{bl}$ and relates to m_{core} and m_{skin} as follows:

$$\begin{aligned} m &= m_{core} + m_{skin} \\ &= (1 - \alpha_{skin})m + \alpha_{skin} m, \\ \alpha_{skin} &= 0.0418 + \frac{0.7425}{\dot{m}_{bl}(1 + u_1) + 0.5854}. \end{aligned}$$

Intense thermal loads might cause the SNS to initiate sweating, which is a secondary regulatory action. Sweat secretion results in an increase in skin hydration level, therefore increasing heat dissipation through evaporation. We model sweat secretion as an increase to the skin hydration level. Heat dissipation through sweat does not occur indiscriminately, rather when the outer layer is fully covered by sweat, dripping occurs which prevent the excess sweat from dissipating heat. Because of this the effect of sweat secretion by modifying (5.6) as follows:

$$q_{ev} = h_e(0.06 + 0.94u_2)(p_2(x_1) - p_{va}).$$

Later, we constrain the range of admissible value of u_2, to replicate the saturation-like effect of heat dissipation through sweating. A secondary regulatory action against cold thermal loads is shivering. This mechanism prevents hazardous falls in CBT by increasing inner heat production. We model it by modifying the expression of the metabolic feat production as follows:

$$M_0(u) = M_0(1 + u_3).$$

Substituting the control actions terms in the open-loop system equations, we obtain:

$$\dot{x}_1 = \frac{A_d}{m_{skin}c_b}(q_{cd}(x,u) - f_{cl}q_{cr}(x) - q_{evap}(x,u)) \tag{5.11}$$

$$\dot{x}_2 = \frac{A_d}{m_{core}c_b}(M_0(u) - q_{cd}(x,u) - q_{br}(x)) \tag{5.12}$$

$$q_{cd}(x) = (k_b + \dot{m}_{bl}c_{bl}(1+u_1))(x_2 - x_1) \tag{5.13}$$

$$q_{cr}(x) = h_c(x_1 - T_{air}) + \sigma\alpha\epsilon\left(x_{1,K}^4 - T_{air,K}^4\right) \tag{5.14}$$

$$q_{br}(x) = 10^{-4}M_0(u)(14(x_2 - T_\infty) + 23(p_2(x_1) - RH \cdot p_2(T_{air}))) \tag{5.15}$$

$$q_{ev}(x) = (0.06 + 0.94u_2)h_e(p_2(x_1) - RH \cdot p_2(T_{air})). \tag{5.16}$$

5.3 Homeostasis Modelling

In [23], the author concludes that the human brain has evolved as to achieve homeostasis during NREM sleep while minimising energy expenditure. The main contribution of this work is seeing the mathematical description of homeostasis as an optimisation problem. Particularly, our model achieves homeostasis by means of a control sequence $u(t)$ that minimises a cost function. We obtain the cost function by considering the need for accurate tracking of the circadian rhythm oscillation and the minimal energy principle , therefore translating in mathematical terms observations made in [23]. We use the following quadratic cost function[1]:

$$S = \int_{t=0}^{t=N} \left[(x(\tau) - x^{ref}(\tau))^{\mathrm{T}}Q(x(\tau) - x^{ref}(\tau)) + u(\tau)^{\mathrm{T}}Ru(\tau)\right]d\tau, \tag{5.17}$$

where N is the time window over which the cost function is minimised and $x^{ref} \in \mathbb{R}^2$ is the vector containing reference trajectories. In the literature, there are various analytical forms for the CBT reference trajectory; in this work, we use the following second-order polynomial [137]:

$$x_2^{ref}(t) = 37.02 - 0.27677\frac{t}{3600} + 0.022234\left(\frac{t}{3600}\right)^2. \tag{5.18}$$

To our knowledge, there are no analytical expressions for skin temperature; in previous works the skin temperature reference value is assumed to be constant and equal to 34.6°C. Finally, Q and R are the matrices describing the weight state each variable has on the optimisation problem. Because this is a new approach,

[1] In the control theory literature, this is referred to as linear quadratic regulator (LQR)

guidelines on designing these matrices do not exist. In this work, we choose Q and R to be diagonal; particularly we use the following matrices:

$$Q = \begin{bmatrix} 5 & 0 \\ 0 & 30 \end{bmatrix}, \quad R = \begin{bmatrix} 1 & 0 \\ 0 & 20 \end{bmatrix}.$$

For $T_{air} < 21°\text{C}$, we need to consider shivering and augment the control weight matrix, that is $R \in \mathbb{R}^{3\times 3}$ and we set the third diagonal element to be $R_{3,3} = 20$. We choose $Q_{2,2} > Q_{1,1}$ to prioritise tracking of CBT with respect to skin. Similarly, we choose $R_{2,2} > R_{1,1}$ and $R_{3,3} > R_{1,1}$ because of the higher energy costs associated with secondary regulatory mechanisms. Finally, we formalise the following constrained optimal control problem:

$$\begin{aligned}
\min_{u(t)} \quad & (5.17) && (5.19)\\
\text{s.t.} \quad & (5.11) - (5.16) && (5.20)\\
& x_1(t) \geq x_{1,\ell}(T_{air}) && (5.21)\\
& x_2^{ref}(t) - \Delta x_2(t) \leq x_2(t) \leq x_2^{ref}(t) + \Delta x_2(t) && (5.22)\\
& u_{1,\ell} \leq u_1(t) \leq u_{1,u} && (5.23)\\
& u_{2,\ell} \leq u_2(t) \leq u_{2,u}. && (5.24)\\
& u_{3,\ell} \leq u_2(t) \leq u_{3,u}. && (5.25)
\end{aligned}$$

5.3.1 State Constraints

We use (5.22) to constrain the CBT such that it follows circadian oscillations, given by $x_2^{ref}(t)$, by imposing a narrow tolerance, which we denote by $\Delta x_2(t)$. We arbitrarily set the tolerance to be 1% of the reference value at any given time instant. As previously mentioned, $x_1^{ref}(t)$ is often given as 34.6°C. However, depending on ambient temperature, skin temperature rather deviate from this value. Particularly, previous works compute the thermoregulatory responses based on the 34.6°C value, even when experimental observations report significantly lower skin temperatures; for example, skin temperature fell to 31°C for $T_{air} = 21°\text{C}$ [151, 137]. The need for skin temperature accurate bounds, particularly in cooler conditions, is important for feasibility of the minimisation problem, we choose $x_{1,\ell}^{ref}$ in (5.21) based on experimental observations.

5.3.2 Control Constraints

Throughout this work, we assume control actions to saturate when deviations of skin temperature from the reference temperature reach 3°C. We denote this value

by ξ_1 and obtained it from the empirical data shown in [151, 137]. We assume the maximum CBT error to be within 1% of its reference trajectory. We obtain the blood flow for the extremal cases by using the empirical equation from [137]:

$$\dot{m}_{bl} = \dot{m}_{bl,0}\frac{1+100e_2}{1+0.25\xi_1}. \tag{5.26}$$

The bounds for the control actions are then obtained by dividing by the nominal blood flow rate:

$$u_{1,\ell} = \frac{1}{1+0.25\xi_1} \tag{5.27}$$

$$u_{1,u} = 1+100\xi_2. \tag{5.28}$$

Control input u_2 that affects sweat production is between 0 and 1. Similarly, the control action generating shivering cannot be negative, as it is only used to increase metabolic heat production, and, therefore, $u_{3,min} = 0$.

$$M_{shiv} = \frac{19.4}{2}\xi_1\xi_2. \tag{5.29}$$

We divide by M_0 to obtain the upper bound $u_{3,u}$.

$$-0.44 \leq u_1(t) \leq 6.88 \tag{5.30}$$

$$0 \leq u_2(t) \leq 1 \tag{5.31}$$

$$0 \leq u_3(t) \leq 0.16. \tag{5.32}$$

5.3.3 Alternative Formulations

In the following, we consider alternative cost functions. Extreme conditions might not allow the human body to solve the optimisation problem (5.19)-(5.25); in such occurrences, it is possible that the human body switches behaviour [146], and prioritises keeping CBT in its correct range. We model this, by providing alternative formulations of the minimisation problem. First, we relax the hypothesis that skin temperature is being tightly regulated. We do so to study whether a physiologically plausible skin temperature value can be achieved while only constraining the CBT to track its reference signal. The associated minimisation problem becomes:

$$\min_{u(t)} \quad S_2 = \int_{t=0}^{t=N} \left[q_{2,2}(x_2 - x_2^{ref})^2 + u^{\mathrm{T}}Ru\right] d\tau, \tag{5.33}$$

$$\text{s.t.} \quad (5.11) - (5.16)$$

$$(5.30) - (5.32)$$

$$x_2^{ref}(t) - \Delta x_2(t) \leq x_2(t) \leq x_2^{ref}(t) + \Delta x_2(t) \tag{5.34}$$

Second, we test thermoregulation under the assumption that a weighted average of skin and core temperatures is regulated. The minimisation problem then becomes:

$$\min_{u(t)} \quad S_3 = \int_{t=0}^{t=N} \left[\bar{q} \left(\frac{m_{skin}}{m} x_1 + \frac{m_{core}}{m} x_2 - x_b^{ref} \right)^2 + u^{\mathrm{T}} R u \right] d\tau, \tag{5.35}$$

$$\text{s.t.} \quad (5.11) - (5.16)$$

$$(5.30) - (5.32)$$

$$x_b^{ref}(t) - \Delta x_b(t) \leq x_b(t) \leq x_b^{ref}(t) + \Delta x_b(t). \tag{5.36}$$

Here we denote the body temperature by x_b and assume its oscillation follows the same dynamics as the one for CBT (5.18), that is, we only change its initial value and set it to 36.66°C following CBT and skin temperature initial values found in the literature [137]. We choose $\Delta x_b(t)$ to be equal to 1% of $x_b^{ref}(t)$. Finally, from now on, we denote the original cost function (5.17) as S_1.

5.4 Simulation

In this Section, we perform simulations for different environmental conditions. We model nonlinear programs (NLP) through CasADi's MATLAB[93] interface using a direct collocation method; we solve it using `IPOPT` [51]. We segment the 85 minutes long [137] NREM epoch in 3 s intervals, and discretise the NLP variables over the intervals using a Gauss-Legendre polynomial of order 3. We choose to use 3 s as interval duration to avoid oscillations in temperature signals. All simulations were carried out on a laptop with a 2.30 GHz Intel Core i7 processor, while using the parameters shown in Table 5.1. We present the results considering two air temperature ranges, which we refer to as "warm conditions" and "cool conditions". We define them by finding the temperature for which the human body transitions from using vasodilation during most of the NREM epoch to using vasoconstriction as means of temperature control; we denote the temperature by $T_{th,i}$, where i denotes the associated minimisation problem, $i = 1,\ 2,\ 3$.

5.4.1 Threshold Temperatures

Finding $T_{th,2}$ and $T_{th,3}$ are straightforward processes as they are independent of skin temperature. While computing $T_{th,2}$, skin temperature converged to approximately 32.0°C, see Fig. 5.2, which is a value comparable to the one in the literature [137]. As explained in Section 5.3, while $x_{1,\ell}^{ref}$ in (5.22) depends on air temperature, there is a lack of models to describe skin lower limit as a function of T_{air}. This makes difficult choosing a physiological value of $x_{1,\ell}^{ref}$ for which small control actions are needed. We choose $x_{1,\ell}^{ref} = 31$°C as it is the lowest experimental

value reported in the literature [151]. Solving the three, minimisation problems we obtain $T_{th,1} = 27.5°\text{C}$, $T_{th,2} = 27.5°\text{C}$, and $T_{th,3} = 27.9°\text{C}$.

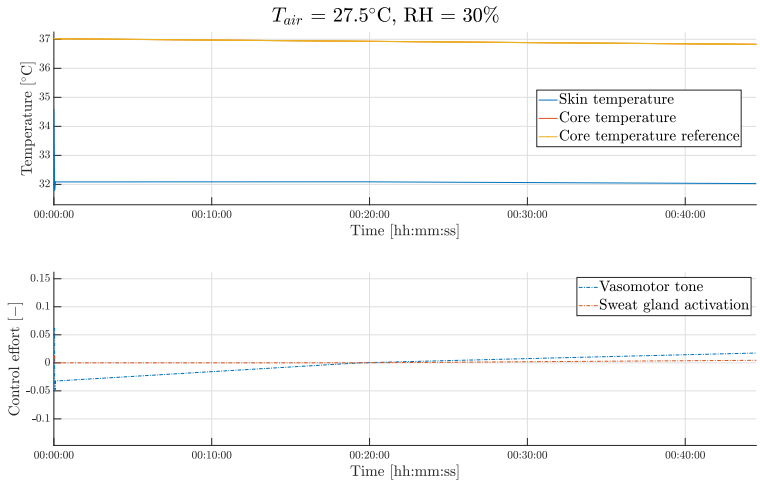

Figure 5.2: Simulation results when minimising S_2 to find threshold temperature $T_{th,2}$.

5.4.2 Warm Conditions

We show the results obtained by our model for two different temperature, that is $T_{air} = [33°\text{C},\ 37°\text{C}]$, at $RH = 30\%$. For both conditions, we set the state initial conditions at:

$$x(t_0) = \begin{bmatrix} 34.60 & 37.02 \end{bmatrix}^{\text{T}}, \quad \text{for } S_1,\ S_2 \tag{5.37}$$

$$x_b(t_0) = 36.66, \quad \text{for } S_3. \tag{5.38}$$

We report the simulation results for $T_{air} = 33°\text{C}$ in Fig. 5.3; and for $T_{air} = 37°\text{C}$ in Fig. 5.4.

5.4.3 Cool Conditions

Cool thermal loads are more challenging to be managed [137]; particularly, because of this, it is possible that the human body gives priority to CBT or changes how thermoregulation is achieved [146]. We investigate this research question by running simulations for progressively lower ambient temperature and by observing how different minimisation problems behave. We find that the minimisation

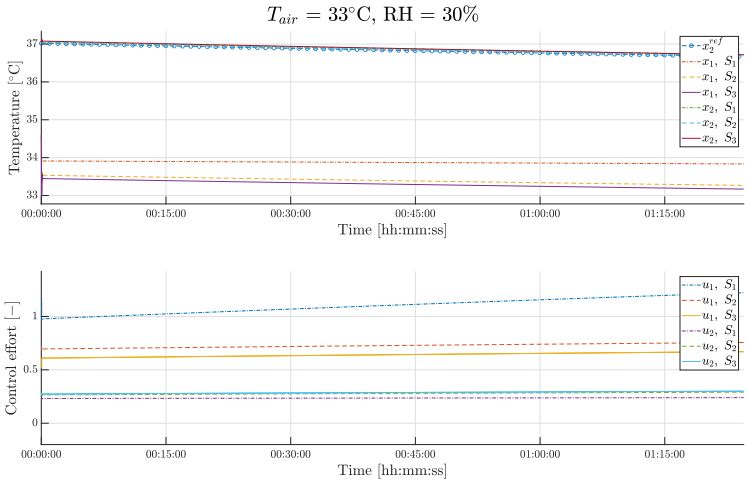

Figure 5.3: Simulation results for $T_{air} = 33°C$, $RH = 30\%$. By looking at experimental data, we set $x_1^{ref} = 34.0°C$, and $x_{1,\ell} = 32°C$.

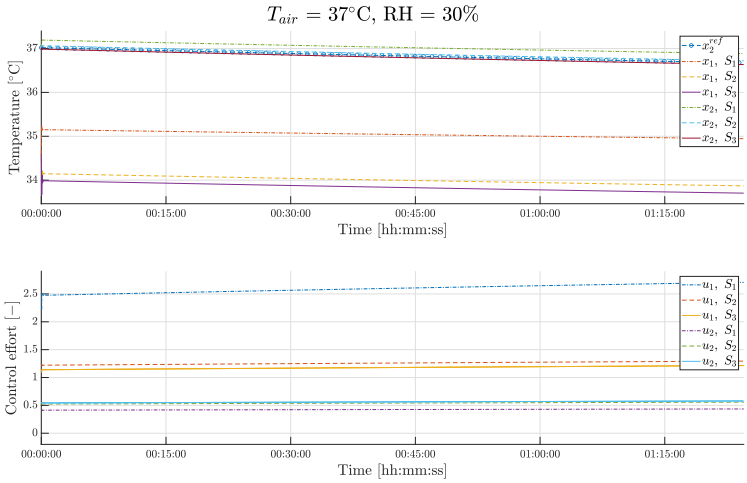

Figure 5.4: Simulation results for $T_{air} = 37°C$, $RH = 30\%$. By looking at experimental data, we set $x_1^{ref} = 36.0°C$, and $x_{1,\ell} = 34°C$.

problem associated with S_1 becomes infeasible at $T_{air} = 25.0°C$, $RH = 30\%$, while the one associated with S_3 loses physiological sense at $T_{air} = 26.4°C$ when CBT

exceeds 38°C, which we assume to be CBT's maximum possible value. We show simulation results when solving S_1, S_2 in Fig. 5.5.

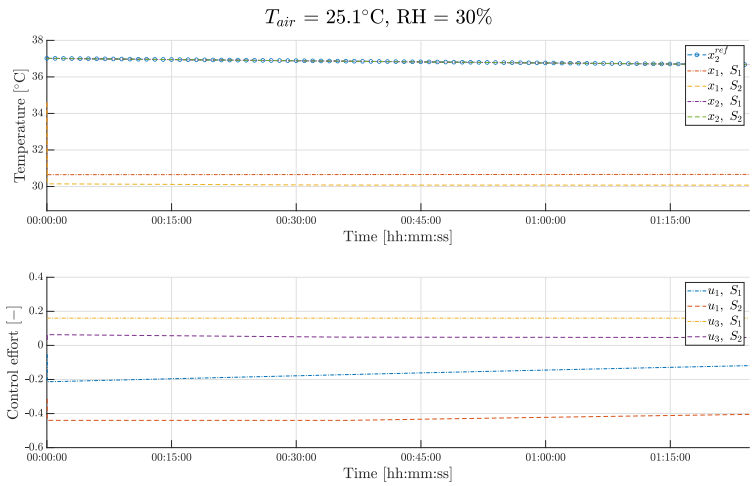

Figure 5.5: Temperature signals for $T_{air} = 25°C$, $RH = 30\%$. We set $x_1^{ref} = 31°C$, and $x_{1,\ell} = 30°C$.

5.5 Discussions

In Section 5.4, we tested our approach for various environmental conditions. It successfully handles warm conditions, where $27.5°C \leq T_{air} \leq 37°C$, as all three minimisation problems are feasible. For both cases shown, S_2 and S_3 obtain similar CBT and skin temperature, as well as similar control effort signals. On the other hand, the solution associated with S_1 exploits vasodilation to move heat from the core to the skin, thereby increasing skin temperature. Sweat productions are rather similar for all three solutions in both simulation scenarios. By looking at experimental temperature data in the literature [151, 137], the solution best representing experimental evidence is the one obtained by solving the problem associated with S_1, particularly because it results in a higher skin temperature. Cool temperatures are more challenging to handle; notably, ambient temperatures lower than 23.4°C make all three optimisation problems infeasible. However, we would like to note that such low temperatures often prevent sleep and might arise from the lack of bedding. Nesting, that is, proper preparation of the sleeping area is observed not only in humans but also in various other species [20]. Furthermore, the absence of bedding has been proven to affect sleep already at $T_{air} = 29°C$ [151].

Also, data in [151], indicates that CBT exhibits an offset of approximately 0.2°C already for air temperatures between 26°C and 32°C. This suggests that the reference value, for skin and core temperatures, depends on air temperature. Furthermore, the decrease in CBT appears to be steeper for lower temperatures [151, 137], suggesting that the CBT reference trajectory used so far it is not appropriate for low ambient temperatures.

5.6 Conclusions

Temperature regulation during sleep is a complex and delicate process strongly related to the circadian rhythm, a fundamental property of human life. To the best of our knowledge, efforts focusing on obtaining mathematical models of thermoregulation have focused on replicating experimental measures using empirical thermoregulatory responses. In this work, we provide, for the first time, a mathematical model of sleep thermoregulation that considers optimal energy allocation. By using our model, we were able to track the theoretical brain temperature trajectory during sleep, while minimising energy usage. Furthermore, we characterised energy usage by taking into consideration the different burden associated to different thermoregulatory responses. Finally, we test the robustness of this framework by testing our model against a variety of environmental conditions. This result is novel for mathematical models of thermoregulation during sleep, as no previous work has considered energy allocation and optimality dynamics.

A second objective is to explore how control action signals and temperature signals behave when thermoregulation is framed as an optimisation problem. Particularly, the insights gained from this second research direction could be used to further refine the algorithm presented in Chapter 4. Such insights could be used as basis for distinguishing expected sweating patterns, and consequent electrodermal activity (EDA) fluctuations, caused by thermoregulation needs from abnormal sweating patterns. Notably, the proposed model is directly linked to the environment and could potentially be expanded to account for different bedding levels, leading to more refined predictions of temperature and control action signals. Furthermore, we believe that advancing sleep medicine beyond automated sleep scoring with machine learning (ML) requires a deeper understanding of the physiological principles governing sleep-related phenomena. In this work, we present a simple yet general framework for investigating various aspects of thermoregulation. By developing a mathematical description that aligns with qualitative observations, such as the saturation of thermoregulatory control actions, we can replicate key human temperature tracking properties while accounting for the body's limited energy reserves. As demonstrated in Section 5.4, our model also captures the increased difficulty of maintaining optimal temperature in colder conditions. Therefore, our model could serve, in future research work, as a bed for further

refinement. Finally, because of how we designed the presented model, small, but key, modifications can allow to estimate the burden of sleep pathologies; for example, by reducing the heat exchanged through respiration, we can investigate the effects of obstructive sleep apnoea (OSA) on thermoregulatory control actions.

Chapter 6

Sufficient Stability Conditions for a Class of Switched Systems With Multiple Steady States

This chapter was accepted for presentation at the 62nd IEEE Control and Decision Conference (CDC) 2023 and for publishing as: "Piccini, J., August, E., Hafstein, S., & Andersen, S. (2023). Sufficient Stability Conditions for a Class of Switched Systems With Multiple Steady States. IEEE Control Systems Letters, 7, 2653–2658. https://doi.org/10.1109/LCSYS.2023.3288735".

Abstract

In this paper, we present a novel approach to determine the stability of switched linear and nonlinear systems using Sum of Squares optimisation. Particularly, we use Sum of Squares optimisation to search for a Lyapunov function that defines an absorbing set that confines solution trajectories. For linear systems, we show that this also implies global asymptotic stability. Using this approach, we can study stability for a broader range of switched systems, particularly, we can search for a global attractor for switched nonlinear systems, whose dynamics are given by polynomial vector fields and which have multiple equilibria or limit cycles.

6.1 Introduction

Switched systems are used for modelling in many different fields [152]. Examples for their use range from the biological sciences [153], for example, the dynamics of human body thermoregulation during sleep abruptly changes when sleep transitions from non-rapid eye movement (REM) sleep to REM sleep [20], to mechan-

ical engineering, where one example is the dynamics of an engine with shifting gears [154]. Switched systems can describe systems, whose dynamics are affected by instantaneous changes, by considering a set of continuous-time sub-systems and a rule governing the switching between them. Analysing switched systems is also important in the field of hybrid systems [152].

We consider switched systems in continuous-time that are of the following form,

$$\dot{x} = f_\sigma(x), \;\; x \in \mathbb{R}^n, \; \sigma : [0, \infty) \to \{1, 2, \dots, N\}. \tag{6.1}$$

Vector x denotes the state of the system and σ is the switching signal; given time-point t, the system dynamics is governed by function $f_i : \mathbb{R}^n \to \mathbb{R}^n$, where $\sigma(t) = i$. That is, there are N functions and which one is "on" is defined by switching signal σ. In this paper, we assume arbitrary switching, that is, switching signal σ fulfils the technical assumption that there is only a finite number of discontinuity-points (switchings) on every finite time-interval, but is otherwise arbitrary. Furthermore, we assume that the f_i are linear or polynomial functions.

Determining stability of an equilibrium point for (6.1), that is of a point $x^* \in \mathbb{R}^n$, for which $f_i(x^*) = 0$ for $i = 1, 2, \dots, N$, is often difficult, even for linear functions f_i [155]. Stability results have been obtained when the dynamics of the switching are non-arbitrary, for instance, when a minimal amount of time must pass before switching occurs [156, 154]; one then speaks of minimal dwell time. However, under arbitrary switching, the problem is notoriously hard and most results and methods used to determine stability of classical linear and nonlinear systems cannot be used. Thus, various works have adapted Lyapunov stability theory to switched systems and considered the construction of a Lyapunov functions for (6.1).

Under arbitrary switching, a necessary condition for stability of an equilibrium of (6.1) is that it is stable for each subsystem given by $\dot{x} = f_i(x)$. Otherwise, if it is not stable for $\dot{x} = f_j(x)$ then it cannot be stable for (6.1); just set $\sigma(t) = j$ for all t. Often, one seeks to find a common quadratic Lyapunov function [154], that is, to find a single quadratic Lyapunov function that guarantees the stability of each individual subsystem. If such a function exists then the equilibrium is also stable for the switched system. In [157, 158], algebraic conditions for the existence of a common quadratic Lyapunov function were defined. Arguably, those conditions on the system matrices seem rather restrictive.

A less conservative approach is to search for a common piecewise linear or polynomial Lyapunov function [159, 160]. In [161], a method for the computation of piecewise quadratic Lyapunov functions is presented. In the literature, there are mainly two approaches to compute such Lyapunov functions [162, 163]. One does so by means of either semidefinite programming or linear programming [164].

A different approach for computing a Lyapunov function is based on Sum of Squares (SOS) optimisation [49]. The advantage of using SOS optimisation is the

ability, for systems whose dynamics are defined by polynomial vector fields, to search for Lyapunov functions that consist of polynomials of higher-order [165]. In [166], the authors use SOS optimisation to search for polynomial Lyapunov functions and piecewise polynomial Lyapunov functions that guarantee global asymptotic stability for switched systems. In [167], the author showed that, for linear switched systems, the existence of a homogenous polynomial Lyapunov function that is SOS is not only sufficient for global asymptotic stability of the equilibrium, but also that such a function, of potentially high degree, must exist if the equilibrium is asymptotically stable.

In this paper, we present a novel method, based on SOS optimisation, to guarantee stability properties of nonlinear switched systems, whose dynamics are governed by polynomial vector fields. We do so by determining a globally absorbing set for the dynamical system given by (6.1). Using this approach, we can study stability for a broader range of problems. For linear switched systems, we show that the existence of such a set translates to global asymptotic stability of the equilibrium at the origin. As the Lyapunov function computed is not necessarily homogenous, one can potentially use polynomial Lyapunov function of lower degree than in [167].

Other approaches have considered invariant sets as a tool to prove stability for switched systems. For example, in [168], a stability theorem for switched systems is provided, where each subsystem possesses an invariant set. In [169] and in [170], the notion of invariant sets and boundedness are invoked to prove stability of switched systems with multiple equilibria. However, all these results depend on nonzero dwell time.

The contributions of this paper are for switched systems, whose dynamics can be described by polynomial vector fields, and are the following. First, by relaxing the problem to determining a globally absorbing set for (6.1) instead of proving global asymptotic stability directly by means of a common Lyapunov function, we can reduce the size of the problem and, thus, the computational effort by searching for Lyapunov functions that potentially consist of non-homogenous polynomials of lower order. Moreover, for switched systems with multiple equilibrium points or limit cycles, our approach provides novel means to establish stability and to characterise the attractor if it exists. This is an extension of the results for the same class of switched systems presented in [166], which provides stability certificates for switched system with a common equilibrium point for the subsystems. For linear systems, the approach presented in this paper scales better with system dimension than the one presented in [164], because no triangulation of the state-space is needed.

The remainder of the paper is organised as follows. Section 6.3 defines an absorbing set and shows how to search for one. Section 6.4 shows that for linear switched systems, the existence of an absorbing set translates to global asymptotic stability of the equilibrium point. In Section 6.5, we apply our method to different

examples. Finally, we conclude the paper in Section 6.6.

6.2 Sum of Squares Decomposition

Consider the real-valued polynomial function $F(x)$ of degree $2d$, $x \in \mathbb{R}^n$. A sufficient condition for $F(x)$ to be nonnegative is that it can be decomposed into a SOS [49]: $F(x) = \sum_i f_i^2(x) \geq 0$, where f_i are polynomial functions. $F(x)$ is a SOS if and only if there exists a positive semidefinite matrix R and $F(x) = \chi^{\mathrm{T}} R \chi$, where

$$\chi^{\mathrm{T}} = \begin{bmatrix} 1 & x_{(1)} & \dots & x_{(n)} & x_{(1)}x_{(2)} & \dots & x_{(n)}^d \end{bmatrix}.$$

The entries of vector χ consist of all monomial combinations of the elements of vector x up to degree d (including $x_{(i)}^0 = 1$) and, thus, its length is $\ell = \binom{n+d}{d}$. Note that R is not necessarily unique. However, $F(x) = \chi^{\mathrm{T}} R \chi$ poses certain constraints on R of the form $\mathrm{tr}(A_j R) = c_j$, where A_j and c_j are appropriate matrices and constants respectively. In general, in order to find R, we solve the optimisation problem associated with the following semidefinite programme:

$$\begin{aligned} \min \quad & \mathrm{tr}(A_0 R) \\ \text{s.t.} \quad & \mathrm{tr}(A_j R) = c_j, \ j = 1, \dots, m \\ & R = R^{\mathrm{T}} \succeq 0. \end{aligned}$$

6.3 Obtaining an Absorbing Set

We investigate the stability of a switched system by searching for a certificate for ultimate boundedness of the switched system and by using it to determine an absorbing set of (6.1). We do so by computing a Lyapunov function, $V(x)$, that is monotonically decreasing along all solution trajectories outside of the absorbing set. The notion of an absorbing set is not only useful for dynamical systems with a unique equilibrium, but also for systems that have multiple equilibria, limit cycles, and/or strange attractors.

6.3.1 Absorbing Sets

An absorbing set is a special kind of positively invariant set. For this reason, we provide the following definitions [42].

Definition 3. *Let $x(t)$ be a solution of the dynamical system $\dot{x} = f(x)$, which we assume to exist for all t. Then p is said to be a positive limit point of $x(t)$ if there is a sequence $\{t_n\}$, with $t_n \to \infty$ as $n \to \infty$, such that $x(t_n) \to p$ as $n \to \infty$.*

Definition 4. *A set M is invariant with respect to $\dot{x} = f(x)$ if*

$$x(0) \in M \Rightarrow x(t) \in M, \text{ for all } t \in \mathbb{R}.$$

This means, that if a solution belongs to M at some time instant, then it belongs to M for all time.

Definition 5. *For (6.1) and a switching signal σ denote by $t \longmapsto \phi_\sigma(t, x_0)$ its solution starting at $x(0) = x_0$. A set $M \subset \mathbb{R}^n$ is said to be* positively invariant *for (6.1), if for every switching signal σ we have*

$$x_0 \in M \Rightarrow \phi_\sigma(t, x_0) \in M, \text{ for all } t \geq 0.$$

A positively invariant set M for (6.1) is said to be an absorbing set *if additionally, for every compact set $C \subset \mathbb{R}^n$ there exist a time $t_C^* \geq 0$ such that for every switching signal σ*

$$x_0 \in C \Rightarrow \phi_\sigma(t, x_0) \in M, \text{ for all } t \geq t_C^*.$$

Now, for a switched system, the following theorem provides conditions for set $\mathcal{B}$ to be a globally, uniformly attractive, positively invariant set, that is, an absorbing set.

Theorem 2. *Assume that for (6.1) there exists a continuously differentiable function $V : \mathbb{R}^n \to \mathbb{R}$, a compact set $\mathcal{B} \subset \mathbb{R}^n$, and constants $\gamma \in \mathbb{R}$, $\rho > 0$, such that*

$$\begin{aligned} V(x) &= \gamma \quad \text{for all } x \in \partial\mathcal{B}, \\ V(x) &> \gamma \quad \text{for all } x \in \mathbb{R}^n \setminus \mathcal{B}, \\ \dot{V}(x) &\leq -\rho \quad \text{for all } x \in \mathbb{R}^n \setminus \mathcal{B}. \end{aligned}$$

Here

$$\dot{V}(x) := \max_{i=1,2,\ldots,N} \nabla V(x) \cdot f_i(x).$$

Then $\mathcal{B}$ is an absorbing set for (6.1).

Proof. The proof of the theorem follows from standard arguments when using Lyapunov stability theory: As long as $x = \phi_\sigma(t, x_0) \notin \mathcal{B}$ we have the condition that $V(x)$ monotonically decreases with time, $\dot{V}(x) \leq -\rho$, which means that

$$V(\phi_\sigma(t, x_0)) - V(x_0) \leq \int_0^t \dot{V}(\phi_\sigma(s, x_0))ds \leq -\rho t.$$

First, it follows from this inequality that if $x_0 \in \partial\mathcal{B}$, then the existence of a switching signal σ and time $t > 0$ such that $\phi_\sigma(s, x_0) \notin \mathcal{B}$ for $0 < s \leq t$ is impossible, because of $\gamma = V(x_0) < V(\phi_\sigma(t, x_0))$. Hence, $\mathcal{B}$ is positively invariant.

Second, again by the inequality, $\mathcal{B}$ must be absorbing. Indeed, fix a compact $C \subset \mathbb{R}^n$ and note that if $C \subset \mathcal{B}$ we can take $t_C^* = 0$. Otherwise denote by $\overline{V}$ the maximum value of V on the closure of $C \setminus \mathcal{B}$ and set $t_C^* = (\overline{V} - \gamma)/\rho > 0$ and note that for an arbitrary $x_0 \in C \setminus \mathcal{B}$ we have

$$\rho t_C^* \geq V(x_0) - \gamma \geq V(x_0) - V(\phi_\sigma(t, x_0)) \geq \rho t$$

as long as $\phi_\sigma(t, x_0) \notin \mathcal{B}$. Thus, there exists a $t^*(x_0) \leq t_C^*$ such that $\phi_\sigma(t, x_0) \in \mathcal{B}$ for all $t \geq t^*(x_0)$ and $\mathcal{B}$ is absorbing. □

A dynamical system with an absorbing set is said to be ultimately bounded system [171]. As shown previously, if a dynamical system possesses an absorbing set, denoted by $\mathcal{B}$, then, not only will all trajectories starting within the absorbing set remain within the set, but also there exists for every $x_0 \in \mathbb{R}^n$ a time point $t^*(x_0) \geq 0$ such that $\phi_\sigma(t, x_0) \in \mathcal{B}$ for all $t \geq t^*(x_0)$ and all switching signals σ. Indeed, $t^*(x_0)$ can be chosen to imply the same for all solutions starting in a neighbourhood of x_0.

Throughout this paper, we use the notion of an absorbing set to obtain stability certificates for switched systems using SOS optimisation [172, 165]. To solve SOS optimisation problems, we use the MATLAB® [93] toolbox SOSTOOLS [173]. For more details on SOS optimisation and the SOS decomposition, see the Appendix.

6.3.2 Obtaining an Absorbing Set

To find a Lyapunov function that defines an absorbing set for switched system (6.1), we apply the approach presented in [171] to all subsystems at once. The following two theorems provide means to obtain an absorbing set.

Theorem 3. *Given constants $\beta \geq 0$, and $\delta > 0$ and integer ℓ, if there exists a radially unbounded SOS polynomial $V(x)$, $V(x) \geq \delta||x||_{2\ell}^{2\ell}$, where $||x||_{2\ell}^{2\ell} = x_1^{2\ell} + x_2^{2\ell} + ... + x_n^{2\ell}$, and a SOS polynomial $p_i(x)$ that solve the following SOS programme,*

$$-f_i(x) \cdot \nabla V(x) - p_i(x)\left(||x||_2^2 - \beta\right) - \delta||x||_{2\ell}^{2\ell} \text{ is SOS } \forall i. \tag{6.2}$$

then there exists $\tilde{\beta} > 0$ such that with $\rho := \delta\tilde{\beta}$ we have

$$\dot{V}(x) \leq -\rho, \text{ for all} ||x||_{2\ell}^{2\ell} \geq \tilde{\beta}. \tag{6.3}$$

Proof. It is shown in [171] that (6.2) implies that

$$f_i(x) \cdot \nabla V(x) \leq -\delta\tilde{\beta} < 0, \text{ for } ||x||_2^2 \geq \beta, \tag{6.4}$$

and, thus, $||x||_{2\ell}^{2\ell} \geq \tilde{\beta}$, where $\tilde{\beta}$ is a positive constant, for all i. It follows that (6.3) holds. □

Theorem 4. *If there exist a positive constant γ and a SOS polynomial $q(x)$ such that*

$$-(V(x)-\gamma)+q(x)(||x||_2^2-\beta) \text{ is SOS} \tag{6.5}$$

then $\mathcal{B}=\{x\in\mathbb{R}^n|V(x)\leq\gamma\}$ is an absorbing set of (6.1), where V and β are from a solution to (6.2).

Proof. If (6.5) holds, where β solves (6.2), then $||x||_2^2 > \beta$ if $V(x) > \gamma$ and it follows from Theorem 2 and Theorem 3 that solution trajectories will approach the level set given by $V(x)=\gamma$ and, thus, that $\mathcal{B}=\{x\in\mathbb{R}^n|V(x)\leq\gamma\}$ is an absorbing set of (6.1). □

In this paper, we first increase the degree of Lyapunov function $V(x)$ (and accordingly of $p_i(x)$) until we obtain a solution to (6.2). Then, we repeatedly solve (6.2) while decreasing $\beta \geq 0$ as much as possible, which provides tighter bounds on the absorbing set. Increasing the value of ℓ allows us to reduce the number of low-degree monomials in $V(x)$; particularly, if the degree of $V(x)$ is 2ℓ then it consists of a homogenous polynomial function. Note that solving (6.2) for $\beta = 0$ is equivalent to finding a common Lyapunov function for the entire state space, as in [166]. If not stated otherwise, we set $\delta = 1$. Additionally, to reduce the size of $\mathcal{B}$, we solve the following problem instead of (6.5),

$$\begin{aligned} &\text{minimise} \quad \gamma \\ &\text{subject to} \quad -(V(x)-\gamma)+q(x)(||x||_2^2-\beta) \text{ is SOS.} \end{aligned} \tag{6.6}$$

For an illustration of absorbing set $\mathcal{B}$, see Fig. 6.1.

6.4 Asymptotic Stability for Linear Systems

For the special case of linear switched systems we have the following theorem.

Theorem 5. *Linear switched systems with asymptotically stable sub-systems and a common equilibrium point, given by $\dot{x} = A_i x$, are asymptotically stable under arbitrary switching if they possess an absorbing set.*

Proof. Essentially, this follows from the homogeneity of linear systems. That is, for a given switching σ and a constant $c > 0$, we have for the solution to the switched linear system, that $\phi_\sigma(t, cx_0) = c\phi_\sigma(t, x_0)$. In the following, $\mathcal{B}_r$ denotes the open ball centred at the origin with radius $r > 0$.

First, we show stability of the origin. Let constant $\varepsilon > 0$ be given. Choose the constant $c > 0$ so large that $\mathcal{B} \subset \mathcal{B}_{c\varepsilon}$ and choose the constant $\delta > 0$ so small

that $\mathcal{B}_{c\delta} \subset \mathcal{B}$. Since $\mathcal{B}$ is positively invariant for the switched system, we have for every switching that the solution $t \longmapsto \phi_\sigma(t, x_0)$ stays in $\mathcal{B}_{c\varepsilon}$ for all $t \geq 0$, whenever $x_0 \in \mathcal{B}_{c\delta} \subset \mathcal{B}$. Thus, $\phi_\sigma([0,\infty), \mathcal{B}_{c\delta}) \subset \mathcal{B}_{c\varepsilon}$ and by the homogeneity property

$$\phi_\sigma([0,\infty), \mathcal{B}_\delta) \subset \mathcal{B}_\varepsilon.$$

That is, stability follows by the homogeneity property. For an illustration of above argumentation, see Fig. 6.1.

To conclude the proof, we show that $\lim_{t\to\infty} \phi_\sigma(t, x_0) = 0$ for every switching and every $x_0 \in \mathbb{R}^n$. Assume, by way of contradiction, that this does not hold true. Then, there exists a switching signal σ, an $x_0 \in \mathbb{R}^n$, an $\varepsilon > 0$, and an unbounded sequence of times (t_n), such that $\|\phi_\sigma(t_n, x_0)\|_2 > \varepsilon$ for all $n \in \mathbb{N}$. Choose the constant $c > 0$ so large that that $\mathcal{B} \subset \mathcal{B}_{c\varepsilon}$. By the definition of t_C^* with $C = \overline{\mathcal{B}_{c\varepsilon}}$, cf. Definition 5, we have $\phi_\sigma(t, cx_0) \in \mathcal{B} \subset \mathcal{B}_{c\varepsilon}$ for all $t \geq t_C^*$. By the homogeneity property it follows that $\phi_\sigma(t, x_0) \in \mathcal{B}_\varepsilon$ for all $t \geq t_C^*$, which is a contradiction and we have proved the theorem.

□

Finally, Theorem 5 has an obvious corollary.

Corollary 1. *Solutions of linear switched switched systems with asymptotically stable sub-systems given by $\dot{x} = A_i x$ cannot have a periodic solution for any switching σ if the switched system as a whole has an absorbing set.*

6.5 Examples

In this section, we present a few examples. All problems are solved on a MacBook Pro with a 2.3 GHz quad-core Intel Core i5 processor. Furthermore, we solve linear matrix inequalities using semidefinite programming, for which we use YALMIP [174], a MATLAB® [93] toolbox. We solve SOS optimisation problems using SOSTOOLS [173], another MATLAB® toolbox. In both cases, we solve the problems using the solver SeDuMi [47].

6.5.1 Linear Switched System

The first problem is interesting, since it has been often investigated in the literature [164] and shows the potential of solving SOS optimisation problems. The problem consists of determining the asymptotic stability of a planar linear switched system given by

$$\dot{x} = A_{\sigma(t)} x, \ \sigma(t) \in \{1, 2\}, \tag{6.7}$$

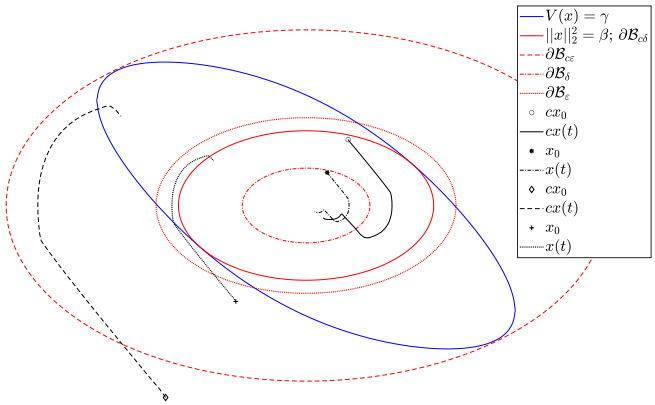

Figure 6.1: The figure shows $\partial\mathcal{B}$, which is given by $V(x) = \gamma$, and its relation to $||x||_2^2 = \beta$ (see main text). Moreover, it depicts two exemplary trajectories used to prove the first part of Theorem 5 ('$\circ$' & '$*$') and two used in the second part, where we choose c sufficiently large such that, for $t > t_C^*$, the trajectory starting at '$\diamond$' is and remains in $\mathcal{B}_{c\varepsilon}$, which implies that the trajectory starting at '+' is and remains in $\mathcal{B}_\varepsilon$ for $t > t_C^*$.

where

$$A_1 = \begin{bmatrix} 0 & 1 \\ -0.1 & -2 \end{bmatrix}, \; A_2 = \begin{bmatrix} 0 & 1 \\ -b & -2 \end{bmatrix}. \tag{6.8}$$

First, note that by solving the following linear matrix inequality,

$$P = P^{\mathrm{T}} \succ 0, \; PA_i + A_i^{\mathrm{T}} P \prec 0, \; i = 1, 2, \tag{6.9}$$

one obtains a common quadratic Lyapunov function up to $b \leq 5.36$.

Now, we let $\beta = 0$ and the degree of $V(x)$ be 2ℓ, that is, we search for a common homogenous polynomial Lyapunov function that guarantees global asymptotic stability. We solve (6.2) for $\beta = 0$ (and $\delta = 0.001$) for increasingly larger values of ℓ, which allows us to increase the value of b, however, not beyond $b = 12$, which is reached for $\ell = 6$. Since the existence of a homogenous polynomial that is SOS, of sufficiently high degree ($\ell >> 1$), and solves (6.2) is a necessary condition for stability [167], we continue increasing the value of ℓ. However, solving (6.2) for $\ell \geq 10$ leads to numerical problems. The Lyapunov function, that we obtain, is given by

$$\begin{aligned} V(x) = {} & 1326.8x_1^{12} + 3997.0355x_1^{11}x_2 + 13366x_1^{10}x_2^2 \\ & + 22545x_1^9x_2^3 + 24318x_1^8x_2^4 + 17999x_1^7x_2^5 \\ & + 10097x_1^6x_2^6 + 4333.6x_1^5x_2^7 + 1379.2x_1^4x_2^8 \\ & + 304.99x_1^3x_2^9 + 44.607x_1^2x_2^{10} + 3.9466x_1x_2^{11} \\ & + 0.1836x_2^{12}. \end{aligned}$$

It follows from Theorem 5 that the switched system presented in this example is globally asymptotically stable for $b = 12$. Finally, $b = 12$ much improves the previously reported result of $b = 5.36$ obtained by solving a linear matrix inequality, particularly, as simulations show that the switched system becomes unstable for $b = 13.26$.

6.5.2 Affine Switched System with 2 Equilibrium Points

In this example, we consider the switched dynamical system given by

$$\dot{x} = A_{\sigma(t)}x + d_{\sigma(t)}, \; d_1 = 0, \; d_2 = \begin{bmatrix} 1 \\ 1 \end{bmatrix}, \; \sigma(t) \in \{1, 2\}, \tag{6.10}$$

where A_1 and A_2 are given by (6.8) for $b = 2$. Note that the equilibrium point of one subsystem is the origin, while for the other one it is not. For $\ell = 2$ and $\beta = 3.3$, we obtain a solution for (6.2).

Specifically, we obtain a homogenous polynomial Lyapunov function of degree 4 that is given by

$$V(x) = 436.8x_1^4 + 929.2x_1^3x_2 + 963.1x_1^2x_2^2 + 519.2x_1x_2^3 + 168.1x_2^4. \tag{6.11}$$

Using this value for β, we solve (6.6) to obtain the boundary of absorbing set $\mathcal{B}$, given by $V(x) = \gamma$, where $\gamma = 8725$ (see Fig. 6.2).

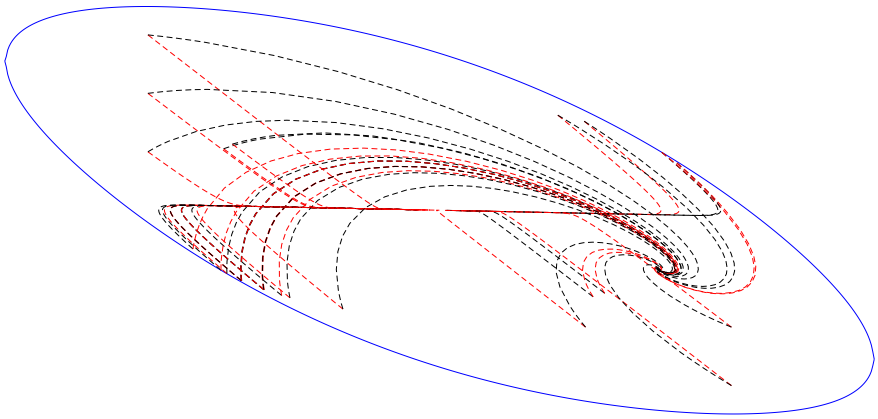

Figure 6.2: The figure shows the boundary of the absorbing set of (6.10) with a few exemplary system trajectories of $\dot{x} = A_1x$ and $\dot{x} = A_2x + d_2$. The boundary is given by $V(x) = 8725$ and $V(x)$ is given by (6.11). The figure lies in the area $[-3, 3] \times [-4, 4]$.

6.5.3 Affine Switched System with 3 Equilibrium Points

Here, we compare our approach to the one in [1], which depends on dwell time, when applied to Example 4.2 in [1], which considers the following switched system that has multiple equilibria,

$$\dot{x} = Ax + b_{\sigma(t)},\ \sigma(t) \in \{1, 2, 3\}, \tag{6.12}$$

where

$$A = \begin{bmatrix} -1 & -1 \\ 1 & -1 \end{bmatrix}, b_1 = \begin{bmatrix} 1 \\ 1 \end{bmatrix} b_2 = \begin{bmatrix} -1 \\ 1 \end{bmatrix} b_3 = \begin{bmatrix} 1 \\ -1 \end{bmatrix}.$$

Solving (6.2), with $\ell = 2$, and $\beta = 2$, we find a fourth order homogenous common Lyapunov function given by

$$V(x) = 8.7957x_1^4 + 1.8977x_1^3x_2 + 17.4811x_1^2x_2^2 - 1.5706x_1x_2^3 + 9.3477x_2^4.$$

We then solve (6.6), for $\beta = 2$ and obtain $\gamma = 38.43$, which guarantees boundedness of system solutions independent of dwell time (see Fig. 6.3); in [1] the average dwell time was required to be bounded away from zero.

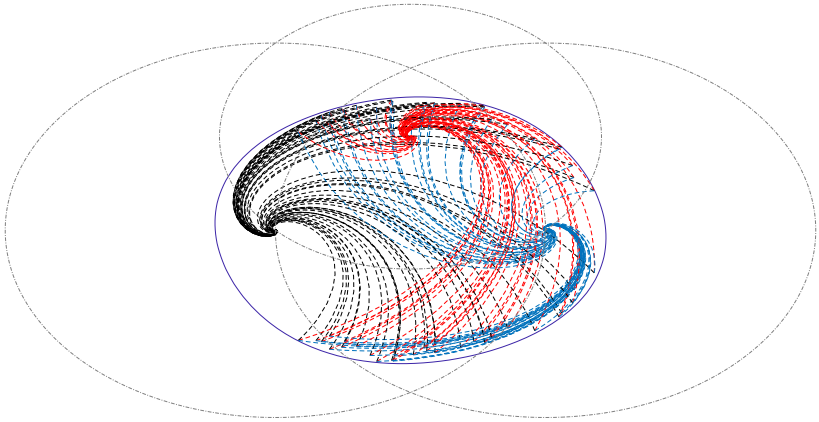

Figure 6.3: The figure shows exemplary trajectories of (6.12) and the boundary of its absorbing set. We overlap the bounded absorbing set obtained using our approach with the absorbing sets, depicted in grey dash-dotted lines, from [1]. The figure lies in the area $[-3.5, 3.5] \times [-3.5, 3.5]$.

6.5.4 Nonlinear Switched System with Unique Equilibrium

Consider the nonlinear switched system given by

$$\dot{x} = A_{\sigma(t)}(x)x, \ \sigma(t) \in \{1, 2\}, \tag{6.13}$$

where

$$A_1(x) = \begin{bmatrix} 0.2868 - x_2^2 & 1.5387 & 0.1731 \\ -0.3628 & 0.0893 & -0.6175 \\ 0.0892 & 1.2898 & -1.4316 \end{bmatrix},$$

$$A_2 = \begin{bmatrix} -1.5007 & 1.3875 & -0.4402 \\ 0.4919 & -1.5442 & 0.1360 \\ 0.2914 & -0.4561 & 0.0231 \end{bmatrix}.$$

First, to solve (6.2) for $\beta = 0$ and, thus, to guarantee asymptotic stability, $V(x)$ must be a SOS polynomial of degree 6. Note that we set $\ell = 2$. On the other hand, solving (6.2) and, then, (6.6), for $\beta = 5$, we can guarantee boundedness of solutions with a Lyapunov function $V(x)$ that is a SOS polynomial of degree 4 (see Fig. 6.4). Significantly, by doing so, the size of the resulting semidefinite programme reported by SOSTOOLS goes down from having 1339 equalities and 262 decision variables to having 444 equalities and 125 decision variables for solving (6.2) and 116 equalities and 41 decision variables for solving (6.6).

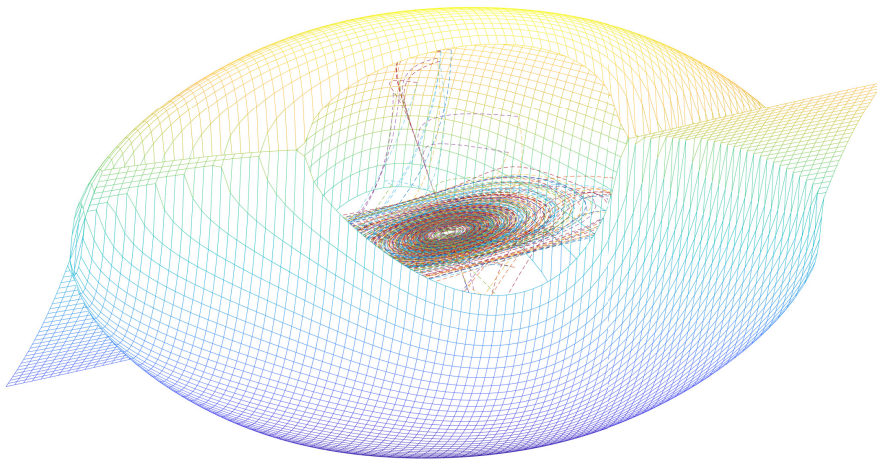

Figure 6.4: The figure shows the boundary of the absorbing set of (6.13) with a few exemplary system trajectories of $\dot{x} = A_1(x)x$ and $\dot{x} = A_2x$. The figure lies in the space $[-5, 5] \times [-2, 2] \times [-3, 3]$.

6.5.5 Nonlinear Switched System with Limit Cycle

In this example, we apply our approach to the analysis of a nonlinear switched system, where one subsystem consist of a Van der Pol oscillator. The system is given by

$$\dot{x} = f_{\sigma(t)}(x),\ \sigma(t) \in \{1, 2\}, \tag{6.14}$$

where

$$\begin{aligned} f_1(x) &= \begin{bmatrix} x_2 \\ -x_1 - (x_1^2 - 1)x_2 \end{bmatrix}, \\ f_2(x) &= \begin{bmatrix} x_2 \\ -6x_1 - 2x_2 \end{bmatrix}. \end{aligned} \tag{6.15}$$

Note that subsystem $f_1(x)$ admits a limit cycle around the origin, which is an unstable equilibrium point of the subsystem. However, we can show that the system possess an absorbing set with the origin in its interior. Specifically, for $\ell = 1$, $\delta = 0.0001$, and $\beta = 14$, solving (6.2) and, then, (6.6), we can bound system trajectories. Specifically, we obtain a Lyapunov function of degree 6 that defines the boundary of the absorbing set $\mathcal{B}$ (see Fig. 6.5).

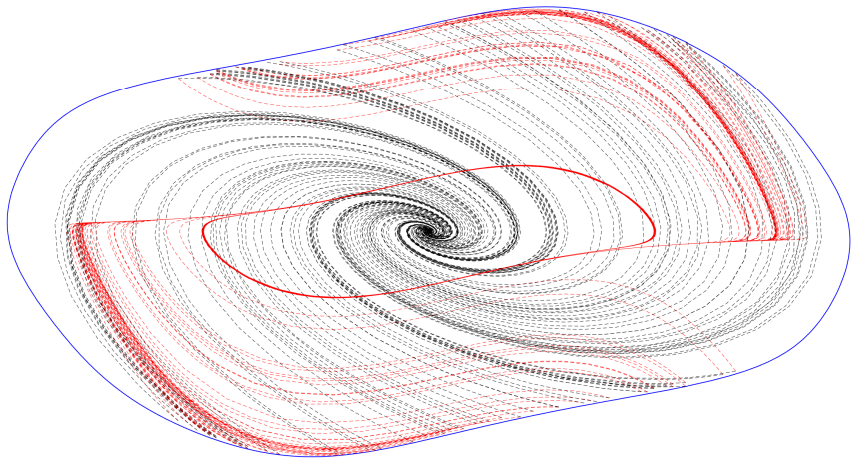

Figure 6.5: The figure shows the boundary of the absorbing set of (6.14) with a few exemplary system trajectories. The figure lies in the area $[-3.8, 3.8] \times [-9.5, 9.5]$.

6.6 Conclusions

Using SOS optimisation, in this paper, we presented a novel approach to provide stability certificates for switched linear and nonlinear systems, whose dynamics are described through polynomial vector fields, under arbitrary switching. We did so, by providing means to search for certificates of ultimate boundedness of the switched system under consideration. We also showed that, for linear switched systems, the existence of an absorbing set implies global asymptotic stability. We applied the presented approach to different examples to illustrate that it allows to locate an absorbing set, even when the switched system is composed of subsystems with distinct equilibrium points or possessing limit cycles. Furthermore, we showed that if guaranteeing boundedness of solutions is sufficient, as opposed to guaranteeing global asymptotic stability of an equilibrium, then our novel method might achieve this with reduced computational effort.

APPENDIX

Sum of Squares Decomposition

Consider the real-valued polynomial function $F(x)$ of degree $2d$, $x \in \mathbb{R}^n$. A sufficient condition for $F(x)$ to be nonnegative is that it can be decomposed into a SOS [49]: $F(x) = \sum_i f_i^2(x) \geq 0$, where f_i are polynomial functions. $F(x)$ is a SOS if and only if there exists a positive semidefinite matrix R and $F(x) = \chi^{\mathrm{T}} R \chi$, where

$$\chi^{\mathrm{T}} = \begin{bmatrix} 1 & x_{(1)} & \dots & x_{(n)} & x_{(1)}x_{(2)} & \dots & x_{(n)}^d \end{bmatrix}.$$

The entries of vector χ consist of all monomial combinations of the elements of vector x up to degree d (including $x_{(i)}^0 = 1$) and, thus, its length is $\ell = \binom{n+d}{d}$. Note that R is not necessarily unique. However, $F(x) = \chi^{\mathrm{T}} R \chi$ poses certain constraints on R of the form $\mathrm{tr}(A_j R) = c_j$, where A_j and c_j are appropriate matrices and constants respectively. In general, in order to find R, we solve the optimisation problem associated with the following semidefinite programme:

$$\begin{aligned} \min \quad & \mathrm{tr}(A_0 R) \\ \text{s.t.} \quad & \mathrm{tr}(A_j R) = c_j, \ j = 1, \dots, m \\ & R = R^{\mathrm{T}} \succeq 0. \end{aligned}$$

Chapter 7

Conclusions

In this thesis, we developed and presented a number of computational tools allowing to investigate the electrodermal activity (EDA) signal. Particularly, we presented methods exploiting meaningful EDA manifestations, as well as providing a novel framework based on mathematical modelling to investigate the mechanisms driving such manifestations. Specifically, we offered an improved view of thermoregulation during sleep by improving the analysis of the EDA signal, its main manifestation. Furthermore, to gain further insight into the energy-optimal behaviour of thermoregulation during sleep, we used first-principles mathematical modelling and optimal control.

In the first part of the thesis, Chapter 3 and Chapter 4, we developed a signal processing algorithm to automatically detect EDA events and EDA storms, two physiological phenomena strongly connected to the specific aspects of sleep health that are sleep staging and obstructive sleep apnoea (OSA).
In Chapter 4, we use feature engineering and Shapley values analysis to show that EDA events and EDA storms can be used in practice to diagnose sleep. The contribution of the first part of this thesis lies in the need of wearable devices to diagnose sleep in an alternative manner compared to the current ones. Wearables are able to measure only a small subset of the traditional signals used to diagnose sleep in polysomnography (PSG) studies. Thus, there is a strong need for new ways of analysing sleep. EDA signal coupled with other, more traditional signals, might help in obtaining more precise sleep health information when using only wearable devices.

In the second part of the thesis, we switched to a systems approach rather than further developing data-driven applications to better understand thermoregulation during sleep and its effects on the EDA signal.
In Chapter 5, we presented a novel approach for describing thermoregulation during sleep. To the best of our knowledge, this is the first time where optimal con-

trol theory is used to study thermoregulation during sleep. The work presented in Chapter 5 might represent a new tool to study sleep from a quantitative standpoint by using well-established methods from control theory. Moreover, thermoregulation during sleep undergoes an abrupt change when transitioning between non-rapid eye movement (NREM) and REM sleep, this means that thermoregulation during sleep can be treated as switched systems. Characterising this category of systems requires specialised methods.
In Chapter 6, we presented a computationally efficient method for providing stability certificates for a class of switched systems. Our allows to study stability for a broader range of switched system. Furthermore, we demonstrated how our method compares with other results from the literature, which, however, were subject to tighter constraints, such as dwell time assumptions

7.1 Future Research Directions

We believe that there is a significant potential for further research work stemming from this thesis. Before discussing broader future research directions, we first provide a brief overview of future work specific to the papers presented in this thesis. For a deeper view, we refer the reader to each chapter's individual Discussion and Conclusions sections.

- The algorithm presented in Chapter 3 relies on EDA signals measured with a high sampling frequency; however, commercially available devices measure EDA signals at much lower sampling frequencies. Because events classification relies on frequency-domain considerations, such low sampling frequencies hinder the algorithms' performances. A new research direction would involve developing and validating new definitions for EDA event for low sampling frequency signals. To achieve this goal, it would be necessary to record, both, high and low sampling frequency signals at the same time. After scoring the high sampling frequency signal with the algorithm presented in Chapter 3, we believe it would then be possible to train a convolutional neural network (CNN) on spectrograms from the low sampling frequency while using the labels obtained using our algorithm.

- The extreme gradient boosting (XGBoost) algorithm shown in Chapter 4 performs sleep staging solely based on the EDA signal. Although, when fine-tuning the model, we obtain satisfactory performances showcasing the potential of introducing EDA in sleep studies, solely using EDA to predict sleep stages is suboptimal. We believe that by combining EDA with other signals, for example, skin temperature and acceleration, we might be able to obtain better performances. One way to do so would be to perform data fusion and using information from all signals to diagnose sleep. An alternative

route would be to predict sleep stages in a sequential fashion, for example, by first detecting sleep and wakefulness epochs, and then identifying different sleep stages. Furthermore, such subsequent classifications problems might use the recorded signals in different but informed ways; as mentioned previously EDA is not the best candidate signal to classify wakefulness and sleep, while actimetry, that is, the use of acceleration signals for classification, has obtained remarkable results distinguishing between wakefulness and sleep. Similar considerations would be made for the other sleep staging classification problems.

- The mathematical model presented in Chapter 5 represents the very first step in accounting for energy aspects during NREM sleep, and therefore paves the way for a wide variety of future research directions. Firstly, our model could be extended to include a larger number of nodes. Additional equations might add further details about different body parts, or might be used to include further information about heat exchange with the surrounding environment. Another research area regards the synthesis of an analytical controller. In this work, we numerically solve a non-linear program. Future research might involve the synthesis of a closed-form controller representing the sympathetic nervous system (SNS). Obtaining such analytical representation, not only would allow to further characterise sleep thermoregulation dynamics, but would also to study the non-rapid eye movement (NREM) - REM switch using switched dynamical systems theory, therefore advancing our understanding of this delicate mechanism

- A second research direction for the mathematical model presented in Chapter 5 would be to modify it to reflect REM sleep. Given the uncertainty about regulating mechanisms in REM sleep; such research would involve hypothesising the existence of a cost function actually being minimised. So far, qualitative research has not been able to identify such cost function. Because of this, there might be need to use inverse optimal control, that is, using data to infer the optimality principle.

We now present two final suggestions for expanding the work presented in this dissertation. First, we propose integrating the mathematical modeling approach into the data-driven applications discussed in this thesis. While Chapters 3-4 do not explicitly consider the temperature signal, it is strongly interconnected with the studied phenomena, as highlighted throughout this work. We believe that incorporating the optimality-driven nature of the thermoregulation process during sleep into the presented algorithms could lead to significant improvements, both in performance and interpretability. What we propose is the design of a “optimality”-parameter obtained from data, and a comparison with the predicted cost from Chapter 5. Finally, we believe that the general approach adopted throughout this

thesis could be applied to investigate other physiological regulation processes of sleep. By doing so, we would create a picture of sleep underlying processes that are causing the phenomena observed through complex devices, therefore allowing us to better understand the dynamics of the human body.

Bibliography

[1] T. Alpcan and T. Başar, "A stability result for switched systems with multiple equilibria," *Dynamics of Continuous, Discrete and Impulsive Systems Series A: Mathematical Analysis*, vol. 17, 2010.

[2] T. Lancet, "Waking up to the importance of sleep," *The Lancet*, vol. 400, p. 973, 9 2022.

[3] H. Alsolai, S. Qureshi, S. M. Z. Iqbal, S. Vanichayobon, L. E. Henesey, C. Lindley, and S. Karrila, "A systematic review of literature on automated sleep scoring," *IEEE Access*, vol. 10, pp. 79 419–79 443, 2022.

[4] D. Ferreira-Santos, P. Amorim, T. S. Martins, M. Monteiro-Soares, and P. P. Rodrigues, "Enabling early obstructive sleep apnea diagnosis with machine learning: Systematic review," *Journal of Medical Internet Research*, vol. 24, p. e39452, 9 2022.

[5] H. Almutairi, G. M. Hassan, and A. Datta, "Machine-learning-based-approaches for sleep stage classification utilising a combination of physiological signals: A systematic review," *Applied Sciences*, vol. 13, p. 13280, 12 2023.

[6] M. D. Zambotti, N. Cellini, A. Goldstone, I. M. Colrain, and F. C. Baker, "Wearable sleep technology in clinical and research settings," *Medicine & Science in Sports & Exercise*, vol. 51, pp. 1538–1557, 7 2019.

[7] M. Rusanen, H. Korkalainen, H. Gretarsdóttir, T. Siilak, K. A. Ólafsdóttir, J. Töyräs, S. Myllymaa, E. S. Arnardóttir, T. Leppänen, and S. Kainulainen, "Self-applied somnography: technical feasibility of electroencephalography and electro-oculography signal characteristics in sleep staging of suspected sleep-disordered adults," *Journal of Sleep Research*, vol. 33, 4 2024.

[8] J. Newell, O. Mairesse, P. Verbanck, and D. Neu, "Is a one-night stay in the lab really enough to conclude? first-night effect and night-to-night vari-

ability in polysomnographic recordings among different clinical population samples," *Psychiatry Research*, vol. 200, pp. 795–801, 12 2012.

[9] F. Dimitri, A. S. Islind, K. A. Ólafsdóttir, S. Sigurdardóttir, K. R. Jóhannsdóttir, J. Hedner, L. Grote, and E. S. Arnardóttir, "Feasibility and usability of three consecutive nights with self-applied, home polysomnography," *Journal of Sleep Research*, 7 2024.

[10] M. Óskarsdóttir, A. S. Islind, E. August, E. S. Arnardóttir, F. Patou, A. M. Maier *et al.*, "Importance of getting enough sleep and daily activity data to assess variability: Longitudinal observational study," *JMIR formative research*, vol. 6, no. 2, p. e31807, 2022.

[11] M. W. Johns, B. A. Cornell, and J. P. Masterton, "Monitoring sleep of hospital patients by measurement of electrical resistance of skin," *Journal of Applied Physiology*, vol. 27, pp. 898–901, 12 1969.

[12] J. Healey and R. Picard, "Detecting stress during real-world driving tasks using physiological sensors," *IEEE Transactions on Intelligent Transportation Systems*, vol. 6, pp. 156–166, 6 2005.

[13] E. Saguin, D. Feingold, J.-B. Roseau, M. Quiquempoix, M. Boussaud, C. Izabelle, A. Metlaine, M. Guillard, P. V. Beers, C. Gheorghiev, B. Lahutte, D. Leger, D. Gomez-Merino, and M. Chennaoui, "An ecological approach to clinically assess nightmares in military service members with severe ptsd," *Sleep Medicine*, vol. 103, pp. 78–88, 3 2023.

[14] W. Boucsein, *Electrodermal Activity*. Springer US, 2012. [Online]. Available: http://link.springer.com/10.1007/978-1-4614-1126-0

[15] A. Malhotra and D. P. White, "Obstructive sleep apnoea," *The Lancet*, vol. 360, pp. 237–245, 7 2002.

[16] P. E. Peppard, T. Young, J. H. Barnet, M. Palta, E. W. Hagen, and K. M. Hla, "Increased prevalence of sleep-disordered breathing in adults," *American Journal of Epidemiology*, vol. 177, pp. 1006–1014, 5 2013.

[17] R. Lv, X. Liu, Y. Zhang, N. Dong, X. Wang, Y. He, H. Yue, and Q. Yin, "Pathophysiological mechanisms and therapeutic approaches in obstructive sleep apnea syndrome," *Signal Transduction and Targeted Therapy*, vol. 8, p. 218, 5 2023.

[18] J. Idiaquez, J. C. Casar, E. S. Arnardottir, E. August, J. Santin, and R. Iturriaga, "Hyperhidrosis in sleep disorders – a narrative review of mechanisms and clinical significance," *Journal of Sleep Research*, 6 2022.

[19] L. Gyllingberg, A. Birhane, and D. J. Sumpter, "The lost art of mathematical modelling," *Mathematical Biosciences*, vol. 362, p. 109033, 8 2023.

[20] E. C. Harding, N. P. Franks, and W. Wisden, "Sleep and thermoregulation," *Current Opinion in Psychology*, vol. 15, pp. 7–13, 2020. [Online]. Available: https://doi.org/10.1016/j.cophys.2019.11.008

[21] ——, "The temperature dependence of sleep," *Frontiers in Neuroscience*, vol. 13, 4 2019.

[22] L. C. Lack, M. Gradisar, E. J. V. Someren, H. R. Wright, and K. Lushington, "The relationship between insomnia and body temperatures," *Sleep Medicine Reviews*, vol. 12, pp. 307–317, 8 2008.

[23] M. H. Schmidt, "The energy allocation function of sleep: A unifying theory of sleep, torpor, and continuous wakefulness," *Neuroscience & Biobehavioral Reviews*, vol. 47, pp. 122–153, 11 2014.

[24] J. M. Siegel, "The rem sleep-memory consolidation hypothesis," 2001.

[25] W. Li, L. Ma, G. Yang, and W. B. Gan, "Rem sleep selectively prunes and maintains new synapses in development and learning," *Nature Neuroscience*, vol. 20, 2017.

[26] A. A. Romanovsky, "Thermoregulation: some concepts have changed. functional architecture of the thermoregulatory system," *American Journal of Physiology-Regulatory, Integrative and Comparative Physiology*, vol. 292, pp. R37–R46, 1 2007.

[27] ——, "Skin temperature: its role in thermoregulation," *Acta Physiologica*, vol. 210, pp. 498–507, 3 2014.

[28] A. R. Adamantidis and L. de Lecea, "Sleep and the hypothalamus," 2023.

[29] M. Glasser, "The transforms and applications handbook. second edition," 2001.

[30] I. Daubechius, "Ten Lectures of Wavelets," *Philadelphia, PA:Sosiety for Industrial and Applied Mathematics Analysis*, pp. 1544–1576, 1992.

[31] I. Daubechies, "Orthonormal bases of compactly supported wavelets," *Communications on Pure and Applied Mathematics*, vol. 41, pp. 909–996, 10 1988.

[32] J. Amann, A. Blasimme, E. Vayena, D. Frey, and V. I. Madai, "Explainability for artificial intelligence in healthcare: a multidisciplinary perspective," *BMC Medical Informatics and Decision Making*, vol. 20, 2020.

[33] Y. Xia, C. Liu, Y. Y. Li, and N. Liu, "A boosted decision tree approach using bayesian hyper-parameter optimization for credit scoring," *Expert Systems with Applications*, vol. 78, 2017.

[34] I. B. Mustapha and F. Saeed, "Bioactive molecule prediction using extreme gradient boosting," *Molecules (Basel, Switzerland)*, vol. 21, 2016.

[35] C. Bentéjac, A. Csörgő, and G. Martínez-Muñoz, "A comparative analysis of gradient boosting algorithms," *Artificial Intelligence Review*, vol. 54, 2021.

[36] R. E. Schapire, "The strength of weak learnability," *Machine Learning*, vol. 5, pp. 197–227, 6 1990.

[37] T. Hastie, R. Tibshirani, and J. Friedman, *The Elements of Statistical Learning*. Springer New York, 2009.

[38] A. Natekin and A. Knoll, "Gradient boosting machines, a tutorial," *Frontiers in Neurorobotics*, vol. 7, 2013.

[39] S. Boyd and L. Vandenberghe, *Convex Optimization*. Cambridge University Press, 3 2004. [Online]. Available: https://www.cambridge.org/core/product/identifier/9780511804441/type/book

[40] J. H. Friedman, "Greedy function approximation: A gradient boosting machine," *Annals of Statistics*, vol. 29, 2001.

[41] T. Chen and C. Guestrin, "XGBoost: A scalable tree boosting system," *Proceedings of the ACM SIGKDD International Conference on Knowledge Discovery and Data Mining*, vol. 13-17-Augu, pp. 785–794, 2016.

[42] H. K. Khalil, *Nonlinear Systems*, 3rd ed. Upper Saddle River, New Jersey: Prentice-Hall, 2000.

[43] J. Löfberg, "Yalmip: A toolbox for modeling and optimization in matlab." IEEE, 2004, pp. 284–289. [Online]. Available: http://ieeexplore.ieee.org/document/1393890/

[44] S. Boyd, L. E. Ghaoui, E. Feron, and V. Balakrishnan, *Linear Matrix Inequalities in System and Control Theory*. Society for Industrial and Applied Mathematics, 1 1994. [Online]. Available: http://epubs.siam.org/doi/book/10.1137/1.9781611970777

[45] L. Vandenberghe and S. Boyd, "Semidefinite programming," *SIAM Review*, vol. 38, pp. 49–95, 3 1996.

[46] Y. Nesterov and A. Nemirovskii, *Interior-Point Polynomial Algorithms in Convex Programming*, 1994.

[47] J. F. Sturm, "Using SeDuMi 1.02, a MATLAB toolbox for optimization over symmetric cones," *Optimization Methods and Software*, vol. 11–12, pp. 625–653, 1999, available at `http://sedumi.ie.lehigh.edu`.

[48] K. G. Murty and S. N. Kabadi, "Some np-complete problems in quadratic and nonlinear programming," *Mathematical Programming*, vol. 39, pp. 117–129, 6 1987.

[49] P. A. Parrilo, "Semidefinite programming relaxations for semialgebraic problems," *Mathematical Programming*, vol. 96, pp. 293–320, 5 2003.

[50] J. A. E. Andersson, J. Gillis, G. Horn, J. B. Rawlings, and M. Diehl, "CasADi – A software framework for nonlinear optimization and optimal control," *Mathematical Programming Computation*, vol. 11, no. 1, pp. 1–36, 2019.

[51] A. Wächter and L. T. Biegler, "On the implementation of an interior-point filter line-search algorithm for large-scale nonlinear programming," *Mathematical Programming*, vol. 106, pp. 25–57, 3 2006.

[52] P. E. Gill, W. Murray, and M. A. Saunders, "Snopt: An sqp algorithm for large-scale constrained optimization," *SIAM Journal on Optimization*, vol. 12, pp. 979–1006, 1 2002.

[53] J. P. Berrut and L. N. Trefethen, "Barycentric lagrange interpolation," *SIAM Review*, vol. 46, 2004.

[54] A. A. Borbély, S. Daan, A. Wirz-Justice, and T. Deboer, "The two-process model of sleep regulation: a reappraisal," *Journal of Sleep Research*, vol. 25, pp. 131–143, 4 2016.

[55] P. L. Parmeggiani, "Thermoregulation and sleep," *Frontiers in Bioscience*, vol. 8, p. 1054, 2003.

[56] E. S. Arnardottir, B. Thorleifsdottir, E. Svanborg, I. Olafsson, and T. Gislason, "Sleep-related sweating in obstructive sleep apnoea: Association with sleep stages and blood pressure," *Journal of Sleep Research*, vol. 19, no. 1 PART. 2, pp. 122–130, 2010.

[57] A. S. Jordan, D. G. McSharry, and A. Malhotra, "Adult obstructive sleep apnoea," *The Lancet*, vol. 383, pp. 736–747, 2 2014.

[58] A. Affanni and G. Chiorboli, "Design and characterization of a real-time, wearable, endosomatic electrodermal system," *Measurement*, vol. 75, pp. 111–121, 11 2015.

[59] C. Tronstad, M. Amini, D. R. Bach, and Ørjan G. Martinsen, "Current trends and opportunities in the methodology of electrodermal activity measurement," *Physiological Measurement*, vol. 43, 2022.

[60] H. F. Posada-Quintero and K. H. Chon, "Innovations in electrodermal activity data collection and signal processing: A systematic review," *Sensors (Switzerland)*, vol. 20, 2020.

[61] E. D. Lascio, S. Gashi, and S. Santini, "Unobtrusive assessment of students' emotional engagement during lectures using electrodermal activity sensors," *Proceedings of the ACM on Interactive, Mobile, Wearable and Ubiquitous Technologies*, vol. 2, pp. 1–21, 9 2018.

[62] M.-Z. Poh, T. Loddenkemper, N. C. Swenson, S. Goyal, J. R. Madsen, and R. W. Picard, "Continuous monitoring of electrodermal activity during epileptic seizures using a wearable sensor." IEEE, 8 2010, pp. 4415–4418.

[63] P. Zontone, A. Affanni, R. Bernardini, A. Piras, and R. Rinaldo, "Stress detection through electrodermal activity (eda) and electrocardiogram (ecg) analysis in car drivers." IEEE, 9 2019, pp. 1–5.

[64] F. A. Jacobsen, E. W. Hafli, C. Tronstad, and Ørjan G. Martinsen, "Classification of emotions based on electrodermal activity and transfer learning - a pilot study," *Journal of Electrical Bioimpedance*, vol. 12, pp. 178–183, 2021.

[65] A. S. Anusha, S. P. Preejith, T. J. Akl, and M. Sivaprakasam, "Electrodermal activity based autonomic sleep staging using wrist wearable," *Biomedical Signal Processing and Control*, vol. 75, no. January, 2022.

[66] S. Gashi, L. Alecci, E. Di, M. E. Debus, F. Gasparini, and S. Santini, "The role of model personalization for sleep stage and sleep quality recognition using wearables," *IEEE Pervasive Computing*, vol. 21, pp. 69–77, 4 2022.

[67] J. Piccini, E. August, M. Óskarsdóttir, and E. S. Arnardóttir, "Using the electrodermal activity signal and machine learning for diagnosing sleep," *Frontiers in Sleep*, vol. 2, 3 2023.

[68] L. E. Lajos, "The relation between electrodermal activity in sleep, negative affect, and stress in patients referred for nocturnal polysomnography," *Dissertation Abstracts International: Section B: The Sciences and Engineering*, vol. 65, no. 5-B, p. 2633, 2004.

[69] A. Sano and R. W. Picard, "Toward a taxonomy of autonomic sleep patterns with electrodermal activity," *Proceedings of the Annual International Conference of the IEEE Engineering in Medicine and Biology Society, EMBS*, pp. 777–780, 2011.

[70] W. Boucsein, *Electrodermal Activity*. Springer US, 2012. [Online]. Available: http://link.springer.com/10.1007/978-1-4614-1126-0

[71] E. S. Arnardottir, C. Janson, E. Bjornsdottir, B. Benediktsdottir, S. Juliusson, S. T. Kuna, A. I. Pack, and T. Gislason, "Nocturnal sweating—a common symptom of obstructive sleep apnoea: the icelandic sleep apnoea cohort," *BMJ Open*, vol. 3, p. e002795, 5 2013.

[72] N. Burch, "Data processing of psychophysiological recordings," *Symposium on the Analysis of Central Nervous System Data Using Computer Methods*, p. 165 – 180, 1965, cited by: 4. [Online]. Available: https://www.scopus.com/inward/record.uri?eid=2-s2.0-84055189057&partnerID=40&md5=ba525fb8027e59e42e885520714796de

[73] A. Sano, R. W. Picard, and R. Stickgold, "Quantitative analysis of wrist electrodermal activity during sleep," *International Journal of Psychophysiology*, vol. 94, no. 3, pp. 382–389, dec 2014. [Online]. Available: https://linkinghub.elsevier.com/retrieve/pii/S0167876014016237

[74] S. Taylor, N. Jaques, W. Chen, S. Fedor, A. Sano, and R. Picard, "Automatic identification of artifacts in electrodermal activity data," *Proceedings of the Annual International Conference of the IEEE Engineering in Medicine and Biology Society, EMBS*, vol. 2015-Novem, pp. 1934–1937, 2015.

[75] D. R. Bach, K. J. Friston, and R. J. Dolan, "An improved algorithm for model-based analysis of evoked skin conductance responses," *Biological Psychology*, vol. 94, pp. 490–497, 2013. [Online]. Available: http://dx.doi.org/10.1016/j.biopsycho.2013.09.010

[76] A. Greco, G. Valenza, A. Lanata, E. P. Scilingo, and L. Citi, "cvxeda: A convex optimization approach to electrodermal activity processing," *IEEE Transactions on Biomedical Engineering*, vol. 63, no. 4, pp. 797–804, 2016.

[77] M. B. Hossain, H. F. Posada-Quintero, Y. Kong, R. McNaboe, and K. H. Chon, "Automatic motion artifact detection in electrodermal activity data using machine learning," *Biomedical Signal Processing and Control*, vol. 74, no. December 2021, p. 103483, 2022. [Online]. Available: https://doi.org/10.1016/j.bspc.2022.103483

[78] R. Rao and J. Chapa, "Algorithms for designing wavelets to match a specified signal," *IEEE Transactions on Signal Processing*, vol. 48, no. 12, pp. 3395–3406, 2000. [Online]. Available: http://ieeexplore.ieee.org/document/887001/

[79] E. S. Arnardottir, A. S. Islind, M. Óskarsdóttir, K. A. Ólafsdóttir, E. August, L. Jónasdóttir, H. Hrubos-Strøm, J. M. Saavedra, L. Grote, J. Hedner, S. Höskuldsson, J. S. Ágústsson, K. R. Jóhannsdóttir, W. T. McNicholas, D. Pevernagie, R. Sund, J. Töyräs, and T. Leppänen, "The sleep revolution project: the concept and objectives," *Journal of Sleep Research*, vol. 31, 8 2022.

[80] B. Kemp, A. Värri, A. C. Rosa, K. D. Nielsen, and J. Gade, "A simple format for exchange of digitized polygraphic recordings," *Electroencephalography and Clinical Neurophysiology*, vol. 82, no. 5, pp. 391–393, may 1992.

[81] A. Kales and A. Rechtschaffen, *A Manual of Standardized Terminology, Techniques and Scoring System for Sleep Stages of Human Subjects*, ser. NIH publication. U. S. National Institute of Neurological Diseases and Blindness, Neurological Information Network, 1968. [Online]. Available: https://books.google.it/books?id=Z41IvQEACAAJ

[82] R. B. Berry, A. A. R. Quan, Stuart F., and et al., "The AASM Manual for the Scoring of Sleep and Associated Events: Rules, Terminology and Technical Specifications. Version 2.6," Darien, IL, pp. 1689–1699, 2020.

[83] P. Madan, V. Singh, D. P. Singh, M. Diwakar, and A. Kishor, "Denoising of ECG signals using weighted stationary wavelet total variation," *Biomedical Signal Processing and Control*, vol. 73, no. July 2021, p. 103478, 2022. [Online]. Available: https://doi.org/10.1016/j.bspc.2021.103478

[84] T. Tuncer, S. Dogan, and A. Subasi, "Surface EMG signal classification using ternary pattern and discrete wavelet transform based feature extraction for hand movement recognition," *Biomedical Signal Processing and Control*, vol. 58, p. 101872, 2020. [Online]. Available: https://doi.org/10.1016/j.bspc.2020.101872

[85] W. Chen, N. Jaques, S. Taylor, A. Sano, S. Fedor, and R. W. Picard, "Wavelet-based motion artifact removal for electrodermal activity," *Proceedings of the Annual International Conference of the IEEE Engineering in Medicine and Biology Society, EMBS*, vol. 2015-Novem, pp. 6223–6226, 2015.

[86] C. K. Chui and C. Heil, "An Introduction to Wavelets," *Computers in Physics*, vol. 6, no. 6, p. 697, 1992.

[87] A. Graps, "An Introduction to Wavelets," *IEEE Computational Science and Engineering*, vol. 2, no. 2, pp. 50–61, 1995.

[88] J. Rafiee, M. A. Rafiee, N. Prause, and M. P. Schoen, "Wavelet basis functions in biomedical signal processing," *Expert Systems with Applications*, vol. 38,

no. 5, pp. 6190–6201, 2011. [Online]. Available: http://dx.doi.org/10.1016/j.eswa.2010.11.050

[89] D. Kaplun, A. Voznesenskiy, S. Romanov, E. Nepomuceno, and D. Butusov, "Optimal estimation of wavelet decomposition level for a matching pursuit algorithm," *Entropy*, vol. 21, no. 9, 2019.

[90] R. Vetrugno, R. Liguori, P. Cortelli, and P. Montagna, "Sympathetic skin response," *Clinical Autonomic Research*, vol. 13, pp. 256–270, 8 2003.

[91] R. Edelberg, *Electrodermal Mechanisms: A Critique of the Two-Effector Hypothesis and a Proposed Replacement*. Boston, MA: Springer US, 1993, pp. 7–29. [Online]. Available: https://doi.org/10.1007/978-1-4615-2864-7_2

[92] I. Martin and P. Venables, *Techniques in Psychophysiology*. J. Wiley, 1980. [Online]. Available: https://books.google.is/books?id=pLBqAAAAMAAJ

[93] MATLAB, *version 9.12.0.1884302 (R2022a)*. Natick, Massachusetts: The MathWorks Inc., 2022.

[94] J. Braithwaite, D. Watson, J. Robert, and R. Mickey, "A Guide for Analysing Electrodermal Activity (EDA) & Skin Conductance Responses (SCRs) for Psychological Experiments," Tech. Rep., 2013.

[95] R. R. Coifman and D. L. Donoho, *Translation-Invariant De-Noising*, 1995. [Online]. Available: http://link.springer.com/10.1007/978-1-4612-2544-7_9

[96] S. T. Kuna, R. Benca, C. A. Kushida, J. Walsh, M. Younes, B. Staley, A. Hanlon, A. I. Pack, G. W. Pien, and A. Malhotra, "Agreement in computer-assisted manual scoring of polysomnograms across sleep centers," *Sleep*, vol. 36, no. 4, pp. 583–589, 2013.

[97] G. Safont, A. Salazar, and L. Vergara, "Vector score alpha integration for classifier late fusion," *Pattern Recognition Letters*, vol. 136, pp. 48–55, 8 2020.

[98] A. Soriano, L. Vergara, B. Ahmed, and A. Salazar, "Fusion of scores in a detection context based on alpha integration," *Neural Computation*, vol. 27, pp. 1983–2010, 9 2015.

[99] R. S. Guthrie, D. Ciliberti, E. A. Mankin, and G. R. Poe, "Recurrent hippocampo-neocortical sleep-state divergence in humans," *Proceedings of the National Academy of Sciences*, vol. 119, 11 2022.

[100] L. B. Baker, "Physiology of sweat gland function: The roles of sweating and sweat composition in human health," *Temperature*, vol. 6, pp. 211–259, 7 2019. [Online]. Available: https://www.tandfonline.com/doi/full/10.1080/23328940.2019.1632145

[101] P. Zontone, A. Affanni, R. Bernardini, A. Piras, and R. Rinaldo, "Stress detection through electrodermal activity (eda) and electrocardiogram (ecg) analysis in car drivers," in *2019 27th European Signal Processing Conference (EUSIPCO)*, 2019, pp. 1–5.

[102] S. Subramanian, B. Tseng, R. Barbieri, and E. N. Brown, "An unsupervised automated paradigm for artifact removal from electrodermal activity in an uncontrolled clinical setting," *Physiological Measurement*, vol. 43, p. 115005, 11 2022.

[103] J.-E. Broman and J. Hetta, "Electrodermal activity in patients with persistent insomnia," *Journal of Sleep Research*, vol. 3, pp. 165–170, 9 1994.

[104] E. S. Arnardottir, A. S. Islind, and M. Óskarsdóttir, "The Future of Sleep Measurements: A Review and Perspective," *Sleep Medicine Clinics*, vol. 16, no. 3, pp. 447–464, sep 2021.

[105] E. S. Arnardottir, A. S. Islind, M. Óskarsdóttir, K. A. Ólafsdóttir, E. August, L. Jónasdóttir, H. Hrubos-Strøm, J. M. Saavedra, L. Grote, J. Hedner, S. Höskuldsson, J. S. Ágústsson, K. R. Jóhannsdóttir, W. T. McNicholas, D. Pevernagie, R. Sund, J. Töyräs, and T. Leppänen, "The sleep revolution project: the concept and objectives," *Journal of Sleep Research*, vol. 31, 8 2022.

[106] R. B. Berry, S. F. Quan, A. R. Abreu, and et al., "The AASM Manual for the Scoring of Sleep and Associated Events: Rules, Terminology and Technical Specifications. Version 2.6," vol. 53, no. 9, pp. 1689–1699, 2020.

[107] L. Genzel, M. C. Kroes, M. Dresler, and F. P. Battaglia, "Light sleep versus slow wave sleep in memory consolidation: a question of global versus local processes?" *Trends in Neurosciences*, vol. 37, pp. 10–19, 1 2014.

[108] F. Chung, P. Liao, H. Elsaid, S. Islam, C. M. Shapiro, and Y. Sun, "Oxygen desaturation index from nocturnal oximetry," *Anesthesia & Analgesia*, vol. 114, pp. 993–1000, 5 2012.

[109] "Sleep-related breathing disorders in adults: recommendations for syndrome definition and measurement techniques in clinical research. The report of an american academy of sleep medicine task force." *Sleep*, vol. 22, pp. 667–89, 8 1999.

[110] R. Schafer, "What is a savitzky-golay filter?" *IEEE Signal Processing Magazine*, vol. 28, pp. 111–117, 7 2011.

[111] T. Verdonck, B. Baesens, M. Óskarsdóttir, and S. vanden Broucke, "Special issue on feature engineering editorial," *Machine Learning*, 8 2021.

[112] N. Burch, "Data processing of psychophysiological recordings," *Symposium on the Analysis of Central Nervous System Data Using Computer Methods*, p. 165 – 180, 1965. [Online]. Available: https://www.scopus.com/inward/record.uri?eid=2-s2.0-84055189057&partnerID=40&md5=ba525fb8027e59e42e885520714796de

[113] J. Piccini, E. August, S. L. Noel Aziz Hanna, and E. S. Arnardóttir, "Automatic Detection of Electrodermal Activity Events during Sleep," *Biomedical Signal Processing and Control*, vol. [*Under Review*], 2023.

[114] H. F. Posada-Quintero, J. P. Florian, A. D. Orjuela-Cañón, T. Aljama-Corrales, S. Charleston-Villalobos, and K. H. Chon, "Power spectral density analysis of electrodermal activity for sympathetic function assessment," *Annals of Biomedical Engineering*, vol. 44, pp. 3124–3135, 10 2016.

[115] N. V. Chawla, K. W. Bowyer, L. O. Hall, and W. P. Kegelmeyer, "Smote: synthetic minority over-sampling technique," *Journal of artificial intelligence research*, vol. 16, pp. 321–357, 2002.

[116] F. Pedregosa, G. Varoquaux, A. Gramfort, V. Michel, B. Thirion, O. Grisel, M. Blondel, P. Prettenhofer, R. Weiss, V. Dubourg, J. Vanderplas, A. Passos, D. Cournapeau, M. Brucher, M. Perrot, and E. Duchesnay, "Scikit-learn: Machine learning in Python," *Journal of Machine Learning Research*, vol. 12, pp. 2825–2830, 2011.

[117] S. M. Lundberg and S.-I. Lee, "A unified approach to interpreting model predictions," in *Advances in Neural Information Processing Systems 30*, I. Guyon, U. V. Luxburg, S. Bengio, H. Wallach, R. Fergus, S. Vishwanathan, and R. Garnett, Eds. Curran Associates, Inc., 2017, pp. 4765–4774. [Online]. Available: http://papers.nips.cc/paper/7062-a-unified-approach-to-interpreting-model-predictions.pdf

[118] S. M. Lundberg, G. G. Erion, and S.-I. Lee, "Consistent individualized feature attribution for tree ensembles," 2 2018.

[119] C. Molnar, *Interpretable Machine Learning*, 2nd ed., 2022. [Online]. Available: https://christophm.github.io/interpretable-ml-book

[120] R. Rothhaas and S. Chung, "Role of the preoptic area in sleep and thermoregulation," *Frontiers in Neuroscience*, vol. 15, 7 2021.

[121] H. Korkalainen, T. Leppanen, J. Aakko, S. Nikkonen, S. Kainulainen, A. Leino, B. Duce, I. O. Afara, S. Myllymaa, and J. Toyras, "Accurate deep learning-based sleep staging in a clinical population with suspected obstructive sleep apnea," *IEEE Journal of Biomedical and Health Informatics*, pp. 1–1, 2019.

[122] S. Chambon, M. N. Galtier, P. J. Arnal, G. Wainrib, and A. Gramfort, "A deep learning architecture for temporal sleep stage classification using multivariate and multimodal time series," *IEEE Transactions on Neural Systems and Rehabilitation Engineering*, vol. 26, pp. 758–769, 4 2018.

[123] U. J. Magalang, N.-H. Chen, P. A. Cistulli, A. C. Fedson, T. Gíslason, D. Hillman, T. Penzel, R. Tamisier, S. Tufik, G. Phillips, and A. I. Pack, "Agreement in the scoring of respiratory events and sleep among international sleep centers," *Sleep*, vol. 36, pp. 591–596, 4 2013.

[124] R. Yanovich, I. Ketko, and N. Charkoudian, "Sex differences in human thermoregulation: Relevance for 2020 and beyond," *Physiology*, vol. 35, pp. 177–184, 5 2020.

[125] M. Grosiak, P. Koteja, U. Bauchinger, and E. T. Sadowska, "Age-related changes in the thermoregulatory properties in bank voles from a selection experiment," *Frontiers in Physiology*, vol. 11, 11 2020.

[126] J. R. Speakman, *Obesity and thermoregulation*, 2018, pp. 431–443.

[127] J. Waalen and J. N. Buxbaum, "Is older colder or colder older? the association of age with body temperature in 18,630 individuals," *The Journals of Gerontology Series A: Biological Sciences and Medical Sciences*, vol. 66A, pp. 487–492, 5 2011.

[128] C. A. Nigro, I. Bledel, and E. Borsini, "Independent association between hypoxemia and night sweats in obstructive sleep apnea," *Sleep and Breathing*, 8 2022.

[129] T. Kamei, T. Tsuda, S. Kitagawa, K. Naitoh, K. Nakashima, and T. Ohhashi, "Physical stimuli and emotional stress-induced sweat secretions in the human palm and forehead," *Analytica Chimica Acta*, vol. 365, pp. 319–326, 6 1998.

[130] R. Refinetti, "Circadian rhythmicity of body temperature and metabolism," *Temperature*, vol. 7, pp. 321–362, 10 2020.

[131] H. F. Nijhout, J. A. Best, and M. C. Reed, "Systems biology of robustness and homeostatic mechanisms," *WIREs Systems Biology and Medicine*, vol. 11, 5 2019.

[132] A. A. Romanovsky, "The thermoregulation system and how it works," pp. 3–43, 2018.

[133] Y. Kobayashi and S. ichi Tanabe, "Development of JOS-2 human thermoregulation model with detailed vascular system," *Building and Environment*, vol. 66, pp. 1–10, 2013.

[134] S. Zhou, B. Li, C. Du, H. Liu, Y. Wu, S. Hodder, M. Chen, R. Kosonen, R. Ming, L. Ouyang, and R. Yao, "Opportunities and challenges of using thermal comfort models for building design and operation for the elderly: A literature review," *Renewable and Sustainable Energy Reviews*, vol. 183, p. 113504, 9 2023.

[135] K. Katić, R. Li, and W. Zeiler, "Thermophysiological models and their applications: A review," *Building and Environment*, vol. 106, pp. 286–300, 9 2016.

[136] A. Zolfaghari and M. Maerefat, "A new simplified model for evaluating non-uniform thermal sensation caused by wearing clothing," *Building and Environment*, vol. 45, pp. 776–783, 3 2010.

[137] P. Dongmei, C. Mingyin, D. Shiming, and Q. Minglu, "A four-node thermoregulation model for predicting the thermal physiological responses of a sleeping person," *Building and Environment*, vol. 52, pp. 88–97, 6 2012.

[138] A. P. Gagge, "An effective temperature scale based on a simple model of human physiological response," *Ashrae Trans.*, vol. 77, no. 1, pp. 247–262, 1971.

[139] K. Kanosue, L. I. Crawshaw, K. Nagashima, and T. Yoda, "Concepts to utilize in describing thermoregulation and neurophysiological evidence for how the system works," *European Journal of Applied Physiology*, vol. 109, pp. 5–11, 5 2010.

[140] R. M. McAllen, M. Farrell, J. M. Johnson, D. Trevaks, L. Cole, M. J. McKinley, G. Jackson, D. A. Denton, and G. F. Egan, "Human medullary responses to cooling and rewarming the skin: A functional mri study," *Proceedings of the National Academy of Sciences*, vol. 103, pp. 809–813, 1 2006.

[141] B. Thomas, M. Soleimani-Mohseni, and P. Fahlén, "Feed-forward in temperature control of buildings," *Energy and Buildings*, vol. 37, pp. 755–761, 7 2005.

[142] D. Fiala, "Dynamic simulation of human heat transfer and thermal comfort," *Sustainable Development*, vol. 45, 1998.

[143] B. Kingma, "Human thermoregulation: a synergy between physiology and mathematical modeling," Ph.D. dissertation, Maastricht University, 2012.

[144] V. Hajnová, F. Zlámal, P. Lenárt, and J. Bienertova-Vasku, "Homeostatic model of human thermoregulation with bi-stability," *Scientific Reports*, vol. 11, p. 17327, 8 2021.

[145] B. R. M. Kingma, M. J. Vosselman, A. J. H. Frijns, A. A. van Steenhoven, and W. D. van Marken Lichtenbelt, "Incorporating neurophysiological concepts in mathematical thermoregulation models," *International Journal of Biometeorology*, vol. 58, pp. 87–99, 1 2014.

[146] J. R. Banga and S. Sager, "Generalized inverse optimal control and its application in biology," 5 2024.

[147] V. Melnikov, V. V. Krzhizhanovskaya, M. H. Lees, and P. M. Sloot, "System dynamics of human body thermal regulation in outdoor environments," *Building and Environment*, vol. 143, pp. 760–769, 10 2018.

[148] D. Dubois and E. Dubois, "A formula to estimate the approximate surface area if height and weight be known," *Nutrition*, vol. 5, no. 5, p. 303 – 311, 1989.

[149] S. Sharma and M. Kavuru, "Sleep and metabolism: An overview," *International Journal of Endocrinology*, vol. 2010, pp. 1–12, 2010.

[150] J. Colin and Y. Houdas, "Experimental determination of coefficient of heat exchanges by convection of human body." *Journal of Applied Physiology*, vol. 22, pp. 31–38, 1 1967.

[151] K. Okamoto-Mizuno, K. Tsuzuki, and K. Mizuno, "Effects of mild heat exposure on sleep stages and body temperature in older men," *International Journal of Biometeorology*, vol. 49, 9 2004.

[152] D. Liberzon, *Switching in Systems and Control*. Birkhäuser Boston, 2003.

[153] N. El-Farra, A. Gani, and P. Christofides, "A switched systems approach for the analysis and control of mode transitions in biological networks," in *Proceedings of the 2005 American Control Conference*, 2005, pp. 3247–3252.

[154] R. Shorten, F. Wirth, O. Mason, K. Wulff, and C. King, "Stability criteria for switched and hybrid systems," *SIAM Review*, vol. 49, no. 4, pp. 545–592, 2007.

[155] D. Liberzon and A. Morse, "Basic problems in stability and design of switched systems," *IEEE Control Systems Magazine*, vol. 19, no. 5, pp. 59–70, 1999.

[156] J. Hespanha and A. Morse, "Stability of switched systems with average dwell-time," in *Proceedings of the 38th IEEE Conference on Decision and Control*, vol. 3, 1999, pp. 2655–2660.

[157] R. Shorten and K. Narendra, "On the stability and existence of common Lyapunov functions for stable linear switching systems," in *Proceedings of the 37th IEEE Conference on Decision and Control*, vol. 4, 1998, pp. 3723–3724.

[158] C. King and M. Nathanson, "On the existence of a common quadratic Lyapunov function for a rank one difference," *Linear Algebra and its Applications*, vol. 419, pp. 400–416, 2006.

[159] H. Lin and P. J. Antsaklis, "Stability and stabilizability of switched linear systems: A survey of recent results," *IEEE Transactions on Automatic Control*, vol. 54, no. 2, pp. 308–322, 2009.

[160] M. Branicky, "Stability of switched and hybrid systems," in *Proceedings of 1994 33rd IEEE Conference on Decision and Control*, vol. 4, 1994, pp. 3498–3503.

[161] M. Johansson and A. Rantzer, "Computation of piecewise quadratic Lyapunov functions for hybrid systems," *IEEE Transactions on Automatic Control*, vol. 43, no. 4, pp. 555–559, 1998.

[162] A. Polanski, "Lyapunov function construction by linear programming," *IEEE Transactions on Automatic Control*, vol. 42, no. 7, pp. 1013–1016, 1997.

[163] S. Hafstein and P. Giesl, "Review on computational methods for Lyapunov functions," *Discrete and Continuous Dynamical Systems - Series B*, vol. 20, pp. 2291–2331, 2015.

[164] S. Andersen, P. Giesl, and S. Hafstein, "Common Lyapunov functions for switched linear systems: Linear programming-based approach," *IEEE Control Systems Letters*, vol. 7, pp. 901–906, 2023.

[165] J. Anderson and A. Papachristodoulou, "Advances in computational Lyapunov analysis using sum-of-squares programming," *Discrete and Continuous Dynamical Systems - Series B*, vol. 20, pp. 2361–2381, 2015.

[166] S. Prajna and A. Papachristodoulou, "Analysis of switched and hybrid systems - beyond piecewise quadratic methods," in *Proceedings of the 2003 American Control Conference*, 2003, pp. 2779–2784.

[167] G. Chesi, "Lmi conditions for time-varying uncertain systems can be non-conservative," *Automatica*, vol. 47, no. 3, pp. 621–624, 2011.

[168] M. Dorothy and S.-J. Chung, "Switched systems with multiple invariant sets," *Systems & Control Letters*, vol. 96, pp. 103–109, 10 2016.

[169] R. Kuiava, R. A. Ramos, H. R. Pota, and L. F. C. Alberto, "Practical stability of switched systems without a common equilibria and governed by a time-dependent switching signal," *European Journal of Control*, vol. 19, no. 3, pp. 206–213, 2013.

[170] S. Veer and I. Poulakakis, "Switched systems with multiple equilibria under disturbances: Boundedness and practical stability," *IEEE Transactions on Automatic Control*, vol. 65, pp. 2371–2386, 6 2020.

[171] E. August and M. Barahona, "Finding positively invariant sets and proving exponential stability of limit cycles using sum-of-squares decompositions," *Journal of Computational Dynamics*, vol. 10, no. 1, pp. 105–126, 2023.

[172] A. Papachristodoulou and S. Prajna, "On the construction of Lyapunov functions using the sum of squares decomposition," in *Proceedings of the 41st IEEE Conference on Decision and Control, 2002.*, vol. 3, 2002, pp. 3482–3487.

[173] A. Papachristodoulou, J. Anderson, G. Valmorbida, S. Prajna, P. Seiler, P. A. Parrilo, M. M. Peet, and D. Jagt, *SOSTOOLS: Sum of squares optimization toolbox for MATLAB*, `http://arxiv.org/abs/1310.4716`, 2021, available from `https://github.com/oxfordcontrol/SOSTOOLS`.

[174] J. Löfberg, "Yalmip: A toolbox for modeling and optimization in matlab," in *Proceedings of the IEEE International Symposium on Computer-Aided Control System Design*, 2004, pp. 284–289.